Département de Physique
Université de Fribourg (Suisse)

Elasticity and Dynamics of Weakly Aggregated Colloidal Systems.

THESE

Présentée à la Faculté des Sciences de l'Université de Fribourg (Suisse) pour l'obtention du grade de Doctor rerum naturalium.

Joaquim Clara Rahola

de

Girona, Catalunya, Espagne

Thèse No. 1557

Imprimerie privée, 2007

Acceptée par la Faculté des Sciences de l'Université de Fribourg (Suisse) sur la proposition de Dr. Véronique Trappe, Prof. Dr. Eckhard Bartsch et Prof. Dr. Peter Schurtenberger (Rapporteurs) et Prof. Dr. Jean-Claude Dousse (Président du Jury).

Fribourg, le 27 Avril 2007.

La Directrice de thèse :

Dr. Véronique Trappe

Le Doyen :

Prof. Dr. Titus Jenny

La vida no es la que uno vivió sino la que uno recuerda y cómo la recuerda para contarla.

Gabriel García Márquez en 'Vivir Para Contarla'.

Els homes volen ésser escoltats. És el que els agrada més. Els agrada més que els diners, que les dones i que menjar i beure bé. Un home escoltat esdevé un fatxenda absolutament feliç.

Josep Pla en 'El Quadern Gris'.

Table of Contents.

Abstract. 6

Résumé. 7

I.- Introduction. 9

II.- Experimental Techniques.

Introduction 15
Dynamic Light Scattering 15
Static Single Scattering 18
Diffusing Wave Spectroscopy 23
Time Resolved Correlation 26
DWS experimental set-up 27
Rheology 30
References 33

III.- Short-time Dynamics and Rheology of Weakly Aggregated Colloidal Gels.

Introduction 36
Experimental Systems: Preparation and Characteristics 37
Results and Discussion 44
Summary 56
References 56

IV.- Non-evolutionary Slow Dynamics in Weakly Aggregated Colloidal Particle Systems.

Introduction 59
Experimental Systems and Methods 59
Results and Discussion 61
References 67

V.- Phase Behavior of Poly(N-isopropyl-acrylamide) Microgels.

Introduction 69
Experimental Systems: Synthesis and Characterization 69
Results and Discussion 72
Summary 93
References 94

Acknowledgments. 96

Curriculum Vitae. 97

Abstract.

In this work we present an experimental study on the elastic and dynamic properties of a variety of colloidal particle suspensions, in which the intrinsic Van der Waals attraction between the particles is modulated by providing the particle with a steric stabilization layer. We use different destabilization methods to trigger aggregation and study the physical properties of the resulting non-equilibrium solids. Experimental methods include Diffusing-Wave Spectroscopy, Dynamic and Static Light Scattering, Small Angle Neutron Scattering, Rheology and Optical Microscopy.

We find that the aggregated phases of our sterically modified particle systems exhibit a short-time dynamics and a mechanical response function that is reminiscent of the one observed in fractal gels. For a series of samples, in which either the particle volume fraction or the particle-particle interaction is varied, the dynamical and mechanical relaxation spectra can be scaled onto each other, revealing the self-similar nature of the aggregated phases obtained. An examination of the interrelation between the scaling parameters indicates that the structural length of the aggregated phases is entirely set by the volume fraction and does not depend on the particle interactions.

We investigate the long time dynamics of one of our sterically modified systems and compare it to the behavior found for a non-modified system. While the long-time dynamics of the non-modified system evolves with the age of the sample, the long-time dynamics of the modified system exhibits a nearly stationary behavior. This nearly stationary relaxation is found to exhibit a strong dependence on volume fraction up to approximately 20%, while it becomes nearly volume fraction independent at larger volume fractions.

Finally, we study the concentration and temperature-dependence of poly-N-isopropyl-acrylamide (PNiPAM) microgels that exhibit a continuous decrease in size with increasing temperature up to the lower critical solution temperature (LCST) of PNiPAM at ~33°C. Below LCST we find the rheological properties of the microgel solutions to be essentially determined by the size and the core-shell nature of the microgels. Our findings indicate that the shells easily interpenetrate at large concentrations and that the viscosity diverges when the core volume fraction reaches random close packing. Above the LCST the particles become attractive; the microgel particles aggregate and form stress-bearing networks that are composed of objects with sharp interfaces, which suggest that aggregation within these systems proceeds at least initially via a liquid-liquid phase separation. The structural characteristics of the networks are temperature independent, while the short-time dynamic properties exhibit strong temperature dependence. We find the slow dynamics of these systems to exhibit a strong evolutionary behavior and to be characterized by temporal heterogeneities. Macroscopic observations suggest that the long-time structural relaxation might be due to micro-collapses of small parts of the network.

Résumé.

Dans ce travail nous présentons une étude expérimentale des propriétés élastiques et dynamiques de différentes suspensions colloïdales. L'attraction de Van der Waals entre les particules est modulée en ajoutant une couronne de stabilisation stérique. Nous utilisons des méthodes de déstabilisation variées pour initier l'agrégation et étudier les propriétés physiques du solide résultant qui est dans un état de non-équilibre. Les méthodes expérimentales utilisées sont la spectroscopie par diffusion multiple de la lumière (DWS), la diffusion de la lumière en statique et en dynamique, la diffusion de neutrons aux petits angles, la rhéologie et la microscopie optique.

Nous observons que la phase agrégée des particules modifiées stériquement présente une dynamique aux temps courts et une réponse mécanique qui sont toutes deux semblables aux gels fractals. Pour une série d'échantillons dans lesquels soit la fraction volumique, soit l'interaction entre les particules sont changées, il est observé que les spectres de relaxation dynamique et mécanique peuvent être superposés. Ceci révèle l'autosimilarité des phases agrégées. Un examen de la relation entre les paramètres utilisés pour la superposition, indique que la longueur caractéristique de structure est déterminée seulement par la fraction volumique et ne dépend pas de l'interaction entre les particules.

Nous étudions la dynamique aux temps longs sur un de nos systèmes modifié stériquement et nous la comparons au comportement observé sur le système non-modifié. Alors que la dynamique aux temps longs pour le système non-modifié évolue avec le temps (vieillissement), celle du système modifié présente un comportement quasi stationnaire. Cette relaxation quasi stationnaire dépend fortement de la fraction volumique en dessous de 20%, tandis qu'au dessus de 20%, elle est indépendante de la fraction volumique.

Finalement, nous étudions la dépendance en concentration et en température des microgels de poly-N-isopropyl-acrylamide (PNiPAM). Lorsqu'on augmente la température jusqu'à la 'Lower Critical Solution Temperature' (LCST), la taille de ces microgels décroît continûment. En dessous de la LCST, nous observons les propriétés rhéologiques d'une solution de microgels qui sont essentiellement déterminées par la taille et la nature cœur-couronne des microgels utilisés. Notre travail montre que les couronnes s'enchevêtrent facilement à forte concentration et que la viscosité diverge lorsque la fraction volumique des cœurs des particules atteint l'empilement aléatoire le plus dense (random close packing). En dessus de la LCST, les particules deviennent attractives et s'agrégent pour former un réseau résistant aux contraintes (stress-bearing). Ce réseau est formé d'objets présentant des interfaces franches. Ceci suggère que l'agrégation dans ces systèmes est initiée par la séparation de phase liquide-liquide. Alors que les caractéristiques structurales du réseau sont indépendantes de la température, les propriétés de la dynamique aux temps courts sont elles,

fortement dépendantes de la température. Nous observons que la dynamique lente de ces systèmes évolue fortement dans le temps et est caractérisée par des hétérogénéités temporelles. Les observations macroscopiques suggèrent que les relaxations structurales aux temps longs pourraient être causées par des micro-effondrements locaux du réseau.

Chapter I.

Introduction.

We typically refer to colloidal suspensions for systems composed of mesoscopic particles suspended in a background fluid. Colloidal suspensions exhibit a rich phase behavior that comprises equilibrium phases such as gases, fluids and crystals and non-equilibrium phases such as gels and glasses [1-6]. The equilibrium properties of colloidal systems can be described using the tools of statistical physics, with colloidal particles acting as atoms. Because the associated time and length scales are larger than the ones corresponding to atomic systems, colloids are often used as model systems to study fundamental problems in statistical mechanics [7, 8]. Moreover, because the colloidal volume fraction and the range and strength of the interaction can be controlled independently we can conveniently access a wide range of phase behavior within a single system [9, 10].

The intrinsic attractive interaction between colloidal particles is the Van der Waals interaction. For equally sized spherical particles of radii a, it is expressed as [11]:

$$U_A(s) = -\frac{A}{6}\left[\frac{2a^2}{(2a+s)^2-4a^2}+\frac{2a^2}{(2a+s)^2}+\ln\left(1-\frac{4a^2}{(2a+s)^2}\right)\right] \tag{I.1}$$

where s is the closest surface-surface distance and A the Hamaker constant, a parameter that depends on the polarizabilities of the fluid and colloid material [9]. Colloidal particles that purely interact by Van der Waals attraction aggregate. Several strategies can be adopted to avoid particle aggregation.

The most common is to provide charge to the particle surface. The charge repulsive potential between spherical particles with constant surface charge density is expressed as [12]:

$$U_R(s) = -2\pi a\varepsilon_0\varepsilon_r\psi_0^2\ln\left[1-\exp(-\kappa s)\right] \tag{I.2}$$

for $\kappa a \ll 1$. Here ψ_0 is the potential on the particle surface, ε_0 is the permittivity in vacuum and ε_r the permittivity of the particle material. The closest inter-particle distance is mainly determined by the range of the ion cloud surrounding a particle, quantified by the Debye-Hückel screening length κ^{-1}:

$$\kappa = \left[\frac{e^2}{\varepsilon_0 \varepsilon_r k_B T} 2[I] \right]^{1/2} \tag{I.3}$$

where the ionic strength $[I] = 1/2 \sum n_i c_i^2$ expresses the concentration n_i of the ion of species i with valency c_i in the background fluid. Assuming additivity of the attractive Van der Waals and the charge repulsive potentials, Derjaguin and Landau and Verwey and Overbeek developed the quantitative theory for the stability of colloidal suspensions known as the DLVO theory [13, 14]. At low ionic strength, the range of the Debye-Hückel screening length is longer ranged than the attraction and the particle interaction is characterized by a potential barrier, as shown in Figure I.(a). At intermediate ionic strengths the screening of the surface charge is not complete and the particle interaction potential is characterized by a deep primary minimum at short distances, by a maximum at intermediate distances and by a secondary minimum at longer distances, as shown in Figure I.(b). Finally, when the charge repulsion is effectively removed, the attractive term governs the particle interaction, as shown in Figure I.(c). At low ionic strength the particle interaction is thus repulsive and the system is a stable suspension of particles, as seen in the image of Figure I.2(a). When the surface charge is not completely screened

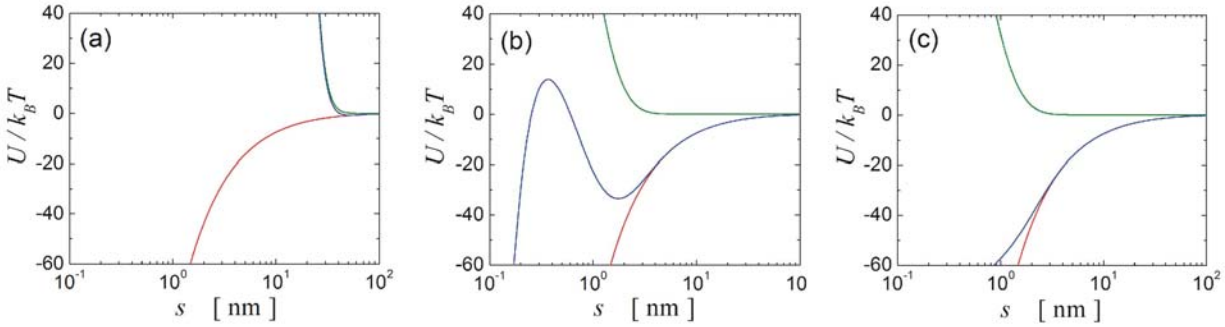

Figure I.1: Interacting potential of charged polystyrene particles of radii a = 360nm and surface charge density of σ = 0.0375 C/m^2. The Van der Waals attraction (red curves) added to the charge repulsion (green curves) results in the DLVO interaction (blue curves). The ionic strength is (a) *[I]* = 10mM, (b) *[I]* =280mM and (c) *[I]* = 400mM.

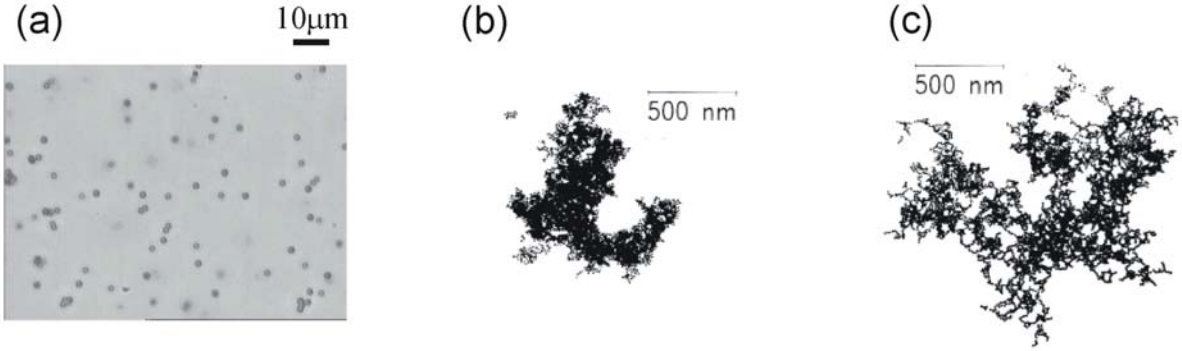

Figure I.2: (a) Charged stabilized polystyrene particles of radii a = 1.5μm. Fractal clusters of gold particles, a = 7.5nm, are formed by (b) RLCA at partial screening and by (c) DLCA at total screening of the surface charge [15].

the particles aggregate at a rate that is determined by the attempt rate to overcome the maximum. This so-called Reaction Limited Cluster Aggregation (RLCA) leads to the formation of rather compact aggregates, as shown in Figure I.2(b) [15]. When the surface charge is completely screened, the aggregation rate is purely determined by diffusion; the particles explore the available free volume and attach to each other upon collision. This Diffusion Limited Cluster Aggregation (DCLA) leads to the formation of more open structures, as shown in Figure I.2(c) [15].

Another mechanism typically used to tune colloidal particle interactions is the steric interaction, where a polymer brush of thickness L is adsorbed or grafted on the particle surface. In a simplified approach we can consider the particle interaction to be infinitely repulsive at contact between the brushes, while the contribution of the brush to the interaction potential is zero at larger distances. The range of the polymer barrier then constitutes a cut off to the Van der Waals attraction, as shown in Figure I.3. For a more accurate description of the potential, additional contributions such as the Van der Waals attraction between polymer chains, solvent-polymer interactions or interpenetration between brushes should be taken into account. Nonetheless, we can assume that if the range of the brush barrier is larger than the range of the attractive potential, the particle interaction is repulsive and the system is stabilized against aggregation. If the range of the brush is much shorter, the potential exhibits a deep minimum and the system

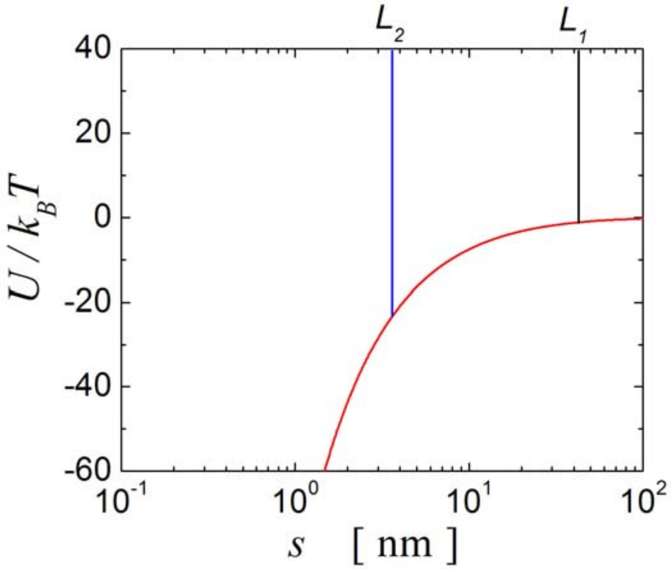

Figure I.3: Scheme of the steric interaction. A polymer brush of thickness *L* (vertical lines) is located on the particle surface. The thickness of the brush determines a cut off to the attractive Van der Waals repulsion (red curve). By adjusting the range of the brush it is possible to tune the particle interaction and span from hard-sphere (black line) to relatively strong attractive potentials (blue line).

aggregates at a rate that again should only be determined by diffusion. If the range of brush is not too short, such that the minimum is shallow, aggregation should be reversible.

The focus of this work is the development of aggregating particle systems in which the particle interactions are modulated by steric stabilization layers. We aim a detailed study of their aggregated states. In Chapter II we describe the experimental techniques used in our investigations. In Chapter III we present three different systems, all of them being partially sterically stabilized. For these systems we explore the short time dynamics and elastic properties of the aggregated phases. Chapter IV presents a study on the slow dynamics of one of our systems. In Chapter V we describe the phase behavior poly(N-isopropyl-acrylamide) microgel particles.

References.

1. P. N. Pusey and W. van Megen, *Phase Behaviour of Concentrated Suspensions of Nearly Hard Colloidal Spheres.* Nature, 1986. **320**(6060): p. 340-342.
2. S. M. Ilett, et al., *Phase Behavior of a Model Colloid-Polymer Mixture.* Physical Review E, 1995. **51**(2): p. 1344-1352.
3. W. Van Megen and S. M. Underwood, *Change in Crystallization Mechanism at the Glass Transition of Colloidal Spheres.* Nature, 1993. **362**(6421): p. 616-618.
4. E. Bartsch, et al., *Dynamic light scattering study of concentrated microgel solutions as mesoscopic model of the glass transition in quasiatomic fluids.* Journal of Chemical Physics, 1992. **97**(6): p. 3950-3963.
5. M. Carpineti, et al., *Salt-induced Fast Aggregation of Polystyrene Latex.* Physical Review A, 1990. **42**(12): p. 7347-7354.
6. M. Y. Lin, et al., *Universality in Colloid Aggregation.* Nature, 1989. **339**(6223): p. 360-62.
7. J. K. G. Dhont, *An Introduction to the Dynamics of Colloids*. 1996, Amsterdam: Elsevier Science.
8. R. Klein, *Interacting Colloidal Suspensions*, in *Neutrons, X-Rays and Light: Scattering Methods Applied to Soft Condensed Matter*, Elsevier, Editor. 2002: Amsterdam. p. 351-379.
9. J. Israelachvili, *Intermolecular & Surface Forces*. 1985, London: Elsevier Academic Press.
10. M. Kleman and O. D. Lavrentovich, *Soft Matter Physics: An Introduction*. 2003, New-York: Springer-Verlag.
11. W. B. Russel, D. A. Saville, and W. R. Schowalter, *Colloidal dispersions*. 1989, Cambridge: Cambridge University Press.
12. R. J. Hunter, *Foundations of Colloid Science*. 1987, Oxford University Press: New York.
13. B. V. Derjaguin and L. D. Landau, *Theory of the Stability of Strongly Charged Lyophobic Sols and the Adhesion of Strongly Charged Particles in Solutions of Electrolytes.* Acta Physicochimica URSS, 1941. **14**: p. 633-662.

14. E. J. W. Verwey and J. Th. G. Overbeek, *Theory of the Stability of Lyophobic Colloids*. 1948, Elsevier: New York.
15. D. A. Weitz, et al., *Limits of the Fractal dimension for Irreversible Kinetic Aggregation of Gold Colloids.* Physical Review Letters, 1985. **54**(13): p. 1416-1419.

Chapter II.

Experimental Techniques.

Introduction.

In this Chapter we describe the experimental techniques used in our studies. Two single light scattering techniques, Dynamic and Static Light Scattering (DLS and SLS, respectively) are employed to characterize our systems. Another single scattering technique, Small Angle Neutron Scattering (SANS) is used to study the structural configuration of concentrated repulsive suspensions. To study the dynamics of aggregated attractive systems, we employ a multiple scattering technique, Diffusive Wave Spectroscopy (DWS) with Time Resolved Correlation (TRC). Rheology is performed to study the mechanical behavior of these gels. We use Optical Microscopy (OM) to directly visualize our systems. DLS and SLS experiments are performed with an ALV/DLS/SLS-5000F monomode fiber compact goniometer system with an ALV-5000 fast correlator and a CCD camera Ultra-Small Angle Light Scattering (USALS) set-up. SANS experiments are performed in the Paul Scherrer Institut, Villigen, Switzerland. In contrast to the single scattering instruments, we constructed our own DWS set-up. Rheological experiments are performed with a Paar Physica MCR300 rheometer using the double gap cuvette geometry. Optical microscopy is performed with an inverted Leica DM IRB microscope and an upright Leica DM LB microscope equipped with a Linkham CSS 450 shear cell that permits an accurate control of the temperature and sample thickness.

The aim of this chapter is to briefly describe the techniques employed in our experiments as applied to the study of soft condensed matter. For a more detailed description, the references listed in this chapter can be consulted, with particular emphasis on [1-6].

Dynamic Light Scattering (DLS).

In a single scattering experiment, radiation with wave vector $\vec{k}_0$ illuminates the sample and scattered light with wave vector $\vec{k}_f$ is detected at an angle θ in the far field,

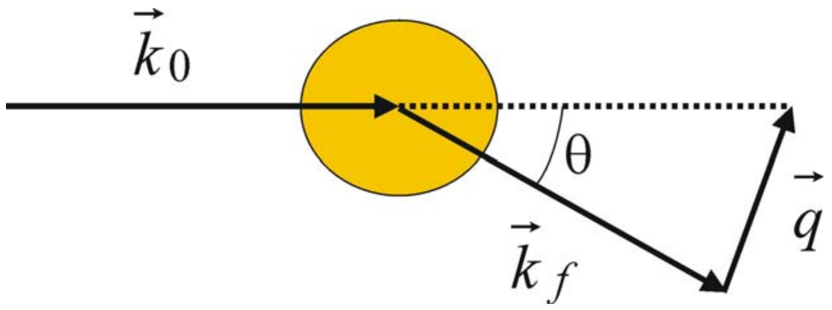

Figure II.1: Schematic representation of a quasi-elastic scattering experiment. The incident beam with wave vector k_0 is scattered at the particle and exits the sample with a wave vector k_f. The intensity is measured as a function of the scattering vector q, which depends on the scattering angle θ.

as shown in Figure II.1. The particle concentration must be low enough in order to guarantee that light is scattered only once. For the quasi-elastic techniques used in this work, $\left|\vec{k}_0\right| \cong \left|\vec{k}_f\right|$, and the wave vectors are related to the scattering vector by $\vec{q} = \vec{k}_0 - \vec{k}_f$, where $\left|\vec{q}\right| = (4\pi n_s / \lambda_0)\sin(\theta/2)$, n_s is the refractive index of the solvent and λo the wavelength of the light in vacuum. For a suspension of N particles, the total scattered field, $\vec{E}(t)$, is the addition of the individual fields scattered by each particle.

$$\vec{E}(t) = \sum_{n=1}^{N} \vec{E}_0 \exp(-i\vec{q}\cdot\vec{r}_n(t)) \qquad \text{(II.1)}$$

Here $\vec{E}_0$ is the scattered field of a single particle at the detector. Since the particles move, their positions $\vec{r}_n(t)$ and thus the phases $\vec{q}\cdot\vec{r}_n(t)$ are time dependent. As the total scattered field fluctuates in time, the magnitude of the field $\vec{E}(\vec{q},t+\tau)$ at a time $t + \tau$ varies with respect to its magnitude at a time t, $\vec{E}(\vec{q},t)$. For small τ, the phase angles have not changed much and $\vec{E}(\vec{q},t+\tau)$ and $\vec{E}(\vec{q},t)$ are still correlated. However, over times such that the phase angles change by 2π, fluctuations in the scattered field become totally uncorrelated. The normalized time correlation function of the scattered field is defined by

$$g_1(q,\tau) = \frac{< E(\vec{q},0)E^*(\vec{q},\tau) >}{< E(\vec{q},0)E^*(\vec{q},0) >} \qquad \text{(II.2)}$$

where < … > denotes the time average; $g_1(q,\tau)$ is decorrelated when a particle moves a distance $r_n(t+\tau) - r_n(t) \sim 2\pi/q$ and thus the length scale probed by the experiment is determined by the scattering vector. The experimentally accessible intensity correlation function $g_2(q,\tau)$ is defined as

$$g_2(q,\tau) = \frac{< I(\vec{q},0)I(\vec{q},\tau) >}{< I(\vec{q},0) >^2} \qquad \text{(II.3)}$$

For gaussian fluctuations, the field correlation function $g_1(q,\tau)$ is directly related to the intensity correlation function $g_2(q,\tau)$ through the Siegert relation [7]:

$$g_2(\vec{q},\tau) = 1 + \beta \cdot \left[g_1(\vec{q},\tau)\right]^2 \qquad \text{(II.4)}$$

where β is a factor that represents the degree of spatial coherence of the scattered light over the detector and is determined by the ratio of the detector area to the area of one speckle. The field correlation function, $g_1(q,\tau)$ is expressed as [7]:

$$g_1(q,\tau) = \exp\left[-\frac{1}{6}q^2 < \Delta r^2(\tau) >\right] \qquad \text{(II.5)}$$

Where $< \Delta r^2(\tau) >$ is the mean square displacement of a particle. For non-interacting particles undergoing Brownian dynamics $< \Delta r^2(\tau) > = 6D_0\tau$, with D_0 the free diffusion coefficient. Then:

$$g_1(q,\tau) = \exp\left[-q^2 D_0 \tau\right] \qquad \text{(II.6)}$$

where the relaxation time of $g_1(q,\tau)$ is $\tau_0 = 1/q^2 D_0$. Figure II.2(a) and (b) show the results of a typical DLS measurement where the particle hydrodynamic radius R_H is determined by using the Stokes-Einstein relation, $D_0 = k_B T / 6\pi\eta R_H$, with η the viscosity of the solvent and T the temperature.

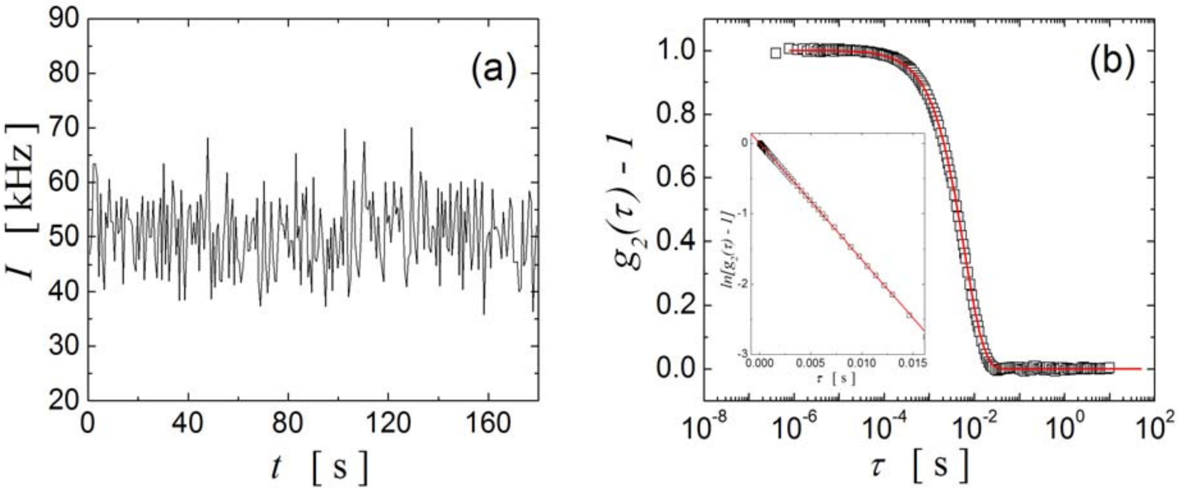

Figure II.2: Typical DLS sizing experiment for a dilute aqueous suspension of particles at T=20°C and η(20°C)=10^{-3} Pa·s. The fluctuating intensity is acquired with a point detector at $q=1.2\cdot 10^{7}\text{m}^{-1}$ (a). By autocorrelating the signal, the intensity correlation function $g_2(\tau)-1$ is determined (b). As shown in the inset, the decay of $g_2(\tau)-1$ is exponential with a characteristic decay time $\tau = -1/(2q^2D)$. From the linear fit (red curve) of ln($g_2(\tau)-1$) and using the Stokes-Einstein relation for the diffusion coefficient $D=k_BT/6\pi\eta R_H$, the particle hydrodynamic radius R_H=400nm is determined.

Static Single Scattering.

In Static Light Scattering (SLS) experiments, a monochromatic coherent beam with amplitude E_I illuminates a sample containing N scatterers at respective positions $\vec{R}_n(t)$. The ensemble averaged scattered intensity is detected at a distance R in the far field, which is expressed as [8]:

$$< I_S(q) >= \frac{E_I^2}{R^2}\left\langle \sum_{j=1}^{N}\sum_{k=1}^{N} b_j(q) b_k^* \exp\left[-i\vec{q}\left(\vec{R}_j - \vec{R}_i\right)\right]\right\rangle \qquad (\text{ II.7 })$$

Where the scattering length $b_n(q)$ of particle n corresponds to the amplitude of the scattered wave relative to that of the incident one. Note that by writing the average scattered intensity as a function of the modulus q of the scattering vector, we have assumed the sample to be spatially isotropic on average, which is characteristic to fluid-like suspensions. For dilute systems, particle positions are uncorrelated and the scattered intensity is the addition of the average intensity scattered by each individual particle:

$$< I_S(q) >= \frac{E_I^2}{R^2} \sum_{j=1}^{N} < \left| b_j(q) \right|^2 > \tag{II.8}$$

Therefore the magnitude of $< I_S(q) >$ as a function of q provides information on the size, structure and geometry of the particles. For identical homogeneous particles of volume V_P, the scattering lengths are equal and the average scattered intensity is:

$$< I_S(q) >= \frac{E_I^2 N}{R^2} < \left| b(0) \right|^2 > P(q) \tag{II.9}$$

Where *P(q)* is the form factor of a particle

$$P(q) = \frac{< \left| b(q) \right|^2 >}{< \left| b(0) \right|^2 >} \tag{II.10}$$

and the scattering length at $q \to 0$, *b(0)*, expresses the contrast between the particles and the background fluid as the difference between their respective refractive indexes n_P and n_L:

$$b(0) = \frac{k_0^2}{2\pi n_0} (n_P - n_L) V_p \tag{II.11}$$

Here n_0 is the refractive index of the suspension. Note that the strength of the scattered intensity depends on the contrast between particles and suspending fluid while the parameter containing the structural information of a particle is the form factor *P(q)*, which for an homogeneous monodisperse spherical particle system of radius *a* is shown in Figure II.3 and expressed as [8]:

$$P(q) = \left[\frac{3}{(qa)^3} \left(\sin(qa) - qa\cos(qa) \right) \right]^2 \tag{II.12}$$

The form factor *P(q)* of an arbitrary particle cannot be expressed by an analytical functional form and it is necessary to consider the particle as composed by N_P equally sized volume elements at positions $\{\vec{R}_m\}$. Then *P(q)* is expressed as [9]:

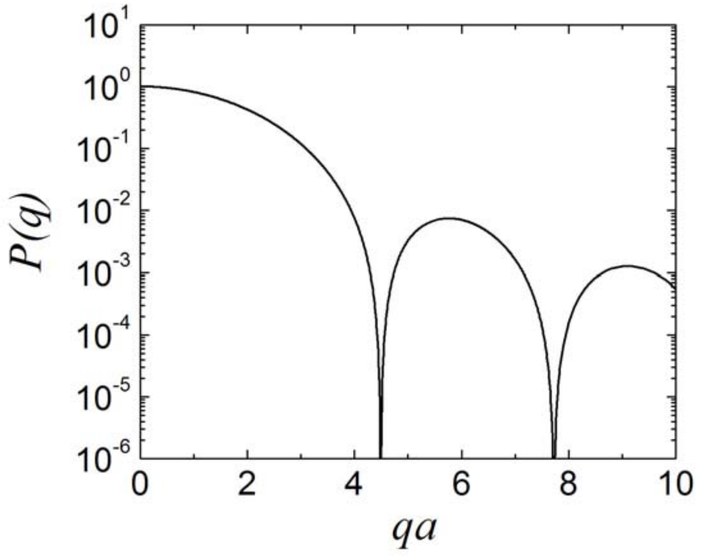

Figure II.3: Form factor *P(q)* corresponding to a particle of radius *a*. The calculation is performed using equation II.12

$$P(q) = \frac{1}{N_P^2} \sum_{m=1}^{N_P} \sum_{n=1}^{N_P} \frac{\sin q\left|\vec{R}_m - \vec{R}_n\right|}{q\left|\vec{R}_m - \vec{R}_n\right|} \qquad \text{(II.13)}$$

Expanding II.13 in powers of q yields the result known as Guinier's expression [10]:

$$P(q) = 1 - \frac{1}{3} q^2 < R_G^2 > + O(q^4) \qquad \text{(II.14)}$$

The radius of gyration $R_G^2 = \frac{1}{N_P} \sum_{m=1}^{N_P} \left|\vec{R}_m - \vec{R}_{CM}\right|^2$, with $\vec{R}_{CM}$ the center of mass of the particle, describes its mass distribution. Note that for a sphere the radius of gyration is $R_G(sphere) = \sqrt{3/5} \cdot a$. Finally, it must be mentioned that the Guinier expression (II.14) is sometimes written as $P(q) = \exp(-q^2 < R_G^2 > /3)$, which is not valid beyond the $O(q^2)$ limit.

So far we have considered experiments on dilute suspensions of particles with uncorrelated dynamics. We introduce now the situation of systems in which particle positions are correlated. For such a system, the average scattered intensity described in equation II.9 is now expressed as [8]:

$$< I_S(q) >= \frac{E_I^2 N}{R^2} < |b(0)|^2 > P(q)S(q) \qquad \text{(II.15)}$$

Thus the average scattered intensity factorizes into the product of equation II.9, which describes the scattering by N uncorrelated particles, and the structure factor *S(q)*, which represents the variation of the intensity due to the spatial correlation of the particles. The particle spatial correlations of a concentrated system are described with the radial distribution function *g(r)*, which denotes the probability of finding the center of any particle at a distance r from the center of a reference particle. Figure II.4(a) shows *g(r)* corresponding to a monodisperse suspension of hard spheres at different volume fractions. As two particles cannot access the same volume, *g(r)* is zero at center-to-center distances below one particle diameter. The main peak of *g(r)*, R_{max}, describes the nearest neighbor shell or cage of particles around a particle, which is determined by the particle interaction. An efficient method typically employed in order to calculate *g(r)* is the approach from Ornstein and Zernike [11], which conceives the total correlation function between two particles as the their direct correlation weighted by the presence of a third particle. However, the calculation of the total correlation function is subject to approximations denoted as closure relations, which are particular to each type of interaction such as the Percus-Yevick closure for hard spheres [12] or the Rogers-Young closure for charged spheres [13]. The structure factor is the Fourier representation of *g(r)* and it is expressed as [11]:

$$S(q) = 1 + 4\pi \frac{N}{V} \int_0^\infty [g(r) - 1] r^2 \frac{\sin qr}{qr} dr \qquad \text{(II.16)}$$

Which is shown in Figure II.4(b) for the previous hard sphere system. The peak of *S(q)* is considered to be approximately a Bragg reflection from planes of particles at a distance equal to the separation between nearest neighbors. The peak position of *g(r)* and *S(q)*, respectively R_{max} and q_{max}, are related by the Bragg condition $q_{max} R_{max} \sim 2\pi$. Therefore, a scattering experiment at a scattering vector q measures on a spatial scale $2\pi/q$.

Experimentally, the measurement of the structure factor is performed in several steps. First it is necessary to measure the intensity scattered by a dilute sample, $< I(q) >_{dil}$, where *S(q)*=1. Then the intensity scattered by the concentrated sample of

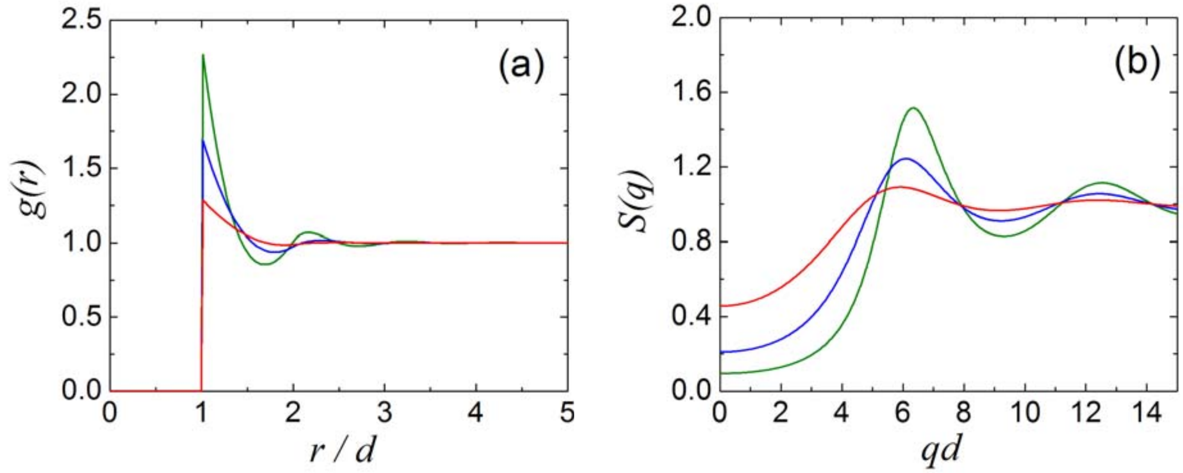

Figure II.4: (a) Radial distribution function *g(r)* and (b) structure factors *S(q)* corresponding to a suspension of hard spheres of diameter *d*. The different colors denote different volume fractions. Red lines denote $\Phi = 0.1$, blue lines denote $\Phi = 0.2$ and green lines denote $\Phi = 0.3$. The calculations are performed using the Percus-Yevick closure relation for hard spheres.

interest, $< I(q) >_{conc}$, is measured. The structure factor is determined as the ratio between the two measurements normalized with the particle concentrations; indeed, it is straightforward to relate the ratio between II.15 and II.9 to the structure factor so that:

$$S(q) = \frac{< I(q) >_{conc} \; N_{dil}}{< I(q) >_{dil} \; N_{conc}} \qquad \text{(II.17)}$$

Although we have restricted ourselves to the static properties of scattered light, it is possible to generalize these results to the scattered intensity of neutron beams. Neutrons are particles for which the wave-particle duality becomes significant. The De Broglie expression relates the wavelength of neutrons λ_n to their mass *m* and velocity *v* as $\lambda_n = h / mv$, with *h* the Planck constant. Neutrons scatter with the nuclei of the sample, and, for soft matter studies, neutrons with λ_n =1.5-1Å are typically used. The weak interaction of neutrons with matter decreases multiple scattering effects and thus neutron scattering is an ideal tool to study optically dense materials. However, neutron scattering lengths depend in an unsystematic way on the nucleus at which neutrons are scattered and there can be a dramatic variation in the scattering length for different isotopes of a given nucleus. Additionally, the scattering length also depends upon the direction of the nuclear spin. Since individual scattering lengths are independent, defining $< b > \equiv < b_j > = < b_k >$ and avoiding prefactors, the average scattered neutron intensity is expressed as [14]:

$$< I(q) >_S = < b >^2 \sum_{j=1}^{N} \left\langle \exp\left[-i\vec{q}\left(\vec{R}_j - \vec{R}_i\right)\right]\right\rangle + N\left(< b^2 > - < b >^2 \right) \qquad \text{(II.18)}$$

The scattered intensity is decomposed into two parts: a first coherent term that contains all the structural information and a second incoherent term that contains no interference contributions and hence no information about the structure of the system. Because of the missing phase relation, the incoherent term can be used to investigate the behavior of individual scatters such as their self-diffusion. However, it is typically considered as a flat background that is subtracted in the data analysis. Then the average scattered intensity of neutrons is formally equivalent to the one of light (equation II.7) and thus it is possible to obtain structural information from scattered neutron intensities within the same framework than SLS. Note, however, that the wavelength of a neutron is smaller than the one of light and thus neutron scattering experiments operate at higher q scale, providing an accessible length scale smaller than SLS.

Diffusing Wave Spectroscopy (DWS).

Diffusing Wave Spectroscopy (DWS) is a technique employed for studying the dynamics of turbid colloidal systems and extends the previously described single-scattering DLS to the multiple-scattering limit. In a turbid system, incoming photons are scattered many times resulting in light propagation that is diffusive-like, with photons undergoing a random walk of step length l^*. This transport mean free path, l^*, is the distance that a photon has to travel to randomize its direction and completely lose the memory of its original direction of propagation. In our experiments, we use rectangular cells of thickness L, where $L >> l^*$ guarantees that the transmitted light is scattered many times. In this regime, the different photon paths are statistically uncorrelated. Thus, the field autocorrelation function from each path is calculated individually; weighted by the path-length distribution function, they are summed up to obtain the total autocorrelation function [15]:

$$g_1(\tau)=\frac{\left(\frac{L}{l^*}+\frac{4}{3}\right)\sqrt{k_0^2<\Delta r^2(\tau)>}}{\left(1+\frac{4}{9}k_0^2<\Delta r^2(\tau)>\right)\sinh\left(\frac{L}{l^*}\sqrt{k_0^2<\Delta r^2(\tau)>}\right)+\frac{4}{3}\sqrt{k_0^2<\Delta r^2(\tau)>}\cosh\left(\frac{L}{l^*}\sqrt{k_0^2<\Delta r^2(\tau)>}\right)} \tag{II.19}$$

where $<\Delta r^2(\tau)>$ is the mean square displacement (MSD) of the particles. For short lag times, this expression can be approximated by a simple exponential function [15]:

$$g_1(\tau)=\exp\left(-\left(\frac{L}{l^*}\right)^2 k_0^2<\Delta r^2(\tau)>\right) \tag{II.20}$$

Note that the relaxation time of $g_1(\tau)$ depends on the step length of the photon random walk, the light wavelength λ_0, and the time averaged mean square displacement of the particles. In contrast to DLS, displacements of the particles much smaller than the wavelength $\Delta r \sim \lambda_0 l^*/L$ are sufficient to lead to a significant phase change of the scattered light and thus to fully relax $g_1(\tau)$. As a result, shorter time scales and smaller particle motions are accessible with DWS than with single-scattering DLS. Contrary to DLS, the final polarization state of the photon is arbitrary as multiple scattering events vary the propagating direction many times. Because each photon is scattered many times and all angular-dependent scattering information is lost, DWS does not provide dynamical information on different length scales and the typical *q*-resolution of single-scattering DLS experiments is not available. In order to extract the relaxation time or the mean square displacement of the particles (MSD), the characteristic length l^* has to be determined for each sample in DWS experiments. When the absorption of light is negligible, the transmitted intensity T is related to l^* according to [15]:

$$T=\frac{5l^*/3L}{1+4l^*/3L} \tag{II.21}$$

Thus it is possible to obtain the magnitude of l^* in the investigated sample by comparing T to the transmitted intensity T_r of a reference sample of known l_r^*. Then

$$l^*=\left(\frac{T_r}{Tl_r^*}+\frac{4(T_r-T)}{3LT}\right)^{-1} \tag{II.22}$$

Once l^* is determined, the only unknown parameter in the expression of the field correlation function is the MSD; this is generally the quantity of interest which can be obtained by finding the zeros of II.7 or II.8, with typical results shown in Figure II.5(a).

Typically DWS measurements are performed with a point detector, such as an optical fiber connected to a photon multiplier (PM). This detection scheme is used when measuring scattered light from samples denoted as ergodic: systems that are free to explore the entirety of their phase space. As all possible spatial configurations of the system are explored, time and ensemble averages are equivalent. The intensity of a single speckle is measured in time, and the intensity autocorrelation function, $g_2(\tau)$, is calculated from the fluctuating scattered light. Classically, data is acquired over a period 10^4 times longer that the slowest relaxation time of $g_2(\tau)$, which guarantees that the ensemble average exhibits good statistics. In a second category of samples, denoted non-ergodic, such as colloidal glasses and gels, particles are localized and exhibit limited excursions around fixed average positions. Because particles are embedded in a limited region of the sample volume, each speckle undergoes limited fluctuations and the time and ensemble averages are no longer equivalent. Therefore, the time-averaged intensity autocorrelation function is no longer related to the ensemble-averaged field autocorrelation function through the Siegert relation (equation II.4) [7]. Fortunately, several schemes have been developed in order to perform light scattering experiments on non-ergodic systems [16-19]. To resolve dynamics on non-ergodic samples using a point detector, we employ the so-called double cell technique [20]. In this scheme, a second cell containing an ergodic medium is placed after the sample to be investigated and serves to properly average the signal of the first cell only. With this strategy, the ensemble averaging of light scattered by the first cell is accomplished. The intensity autocorrelation function measured with this approach is factorized as a product of the correlation functions of the two independent cells [20]:

$$g_2(\tau)-1=\left[g_2(\tau,L_1)-1\right]\cdot\left[g_2(\tau,L_2)-1\right] \tag{II.23}$$

where $g_2(\tau, L_1)$ denotes the intensity autocorrelation function of the non-ergodic medium and $g_2(\tau,L_2)$ denotes the intensity autocorrelation function of the ergodic medium. Then the intensity correlation function of the system under study is:

$$g_2(\tau,L_1)-1=\left[g_2(\tau)-1\right]/\left[g_2(\tau,L_2)-1\right]$$

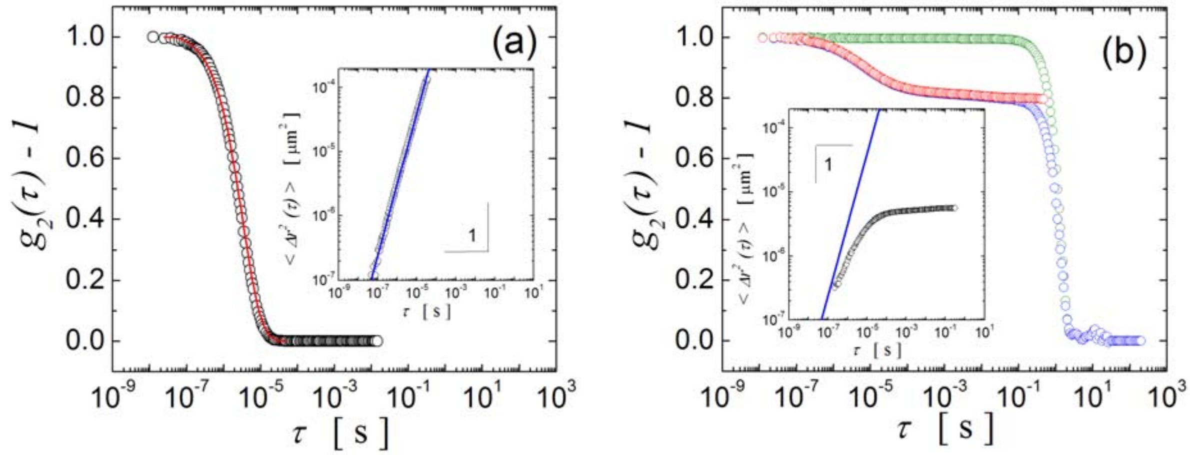

Figure II.5: DWS intensity correlation functions for (a) an ergodic suspension of Brownian particles and (b) a non-ergodic gel. The transport mean free path, *l**, of the suspension is the parameter determined from the fit of the experimental data (black circles) to equation II.19 (red curve). This parameter is used as a reference to determine the *l** corresponding to the gel. The intensity correlation function of the second cell (green circles) is divided from the total intensity correlation function of the gel-second cell system (blue circles); this results in the intensity correlation function of the gel (red circles). In both figures the insets show the respective MSDs. The blue lines in the insets indicate the purely diffusive MSD.

Note that now the Siegert relation applies and thus the dynamics of the system can be resolved as the ergodic problem described above, as shown in Figure II.5(b). One limitation of this approach is the artificial decay imposed by the relaxation of the ergodic sample: all dynamical information for τ greater than the relaxation time of the second cell is lost.

Time Resolved Correlation (TRC).

Traditional single speckle detection techniques do not provide precise time resolution as they only measure time-averaged dynamics. The introduction of the so-called multispeckle technique has addressed this issue [16]. In a multispeckle experiment, the point detector is replaced by the 2-D array of pixels of a CCD camera. Each CCD pixel acts as an independent detector for which an intensity time autocorrelation function is calculated. In multispeckle experiments, the time average that is usually performed in traditional light scattering is replaced by an average over the CCD detector. With this operation the ensemble average is performed and thus dynamics of non-ergodic systems can be studied. Multispeckle detectors allow the use of the recently introduced Time Resolved Correlation (TRC) technique [21, 22], permitting the study of heterogeneous dynamics, a key feature of slow relaxation processes exhibited by non-equilibrium solids, such as glasses, gels, compressed emulsions, and foams [23]. The TRC technique can be applied both to single and multiple scattering experiments; however, in this work, we employ this technique only to study turbid systems.

In a TRC experiment, a series of images of the speckle pattern are recorded with a CCD camera. Motion of the scatterers varies the relative phase of the scattered photons and subsequently the intensity of the speckles. Thus, particle dynamics determine the degree of correlation between images separated a lag time τ; which is quantified by introducing the normalized intensity correlation between speckle images at time *t* and *t* + τ:

$$c_I(t,\tau) = \frac{< I_p(t) I_p(t+\tau) >_p}{< I_p(t) >_p < I_p(t+\tau) >_p} - 1 \qquad \text{(II.24)}$$

where the subscript *p* refers to the CCD pixels. For homogeneous systems, $c_I(t,\tau)$ is time independent, while for a medium characterized by heterogeneities $c_I(t,\tau)$ exhibits spikes at the time position of the heterogeneity. The time average of $c_I(t,\tau)$ yields the normalized intensity autocorrelation function, $g_2(\tau)-1$:

$$g_2(\tau) - 1 = \frac{<< I_p(t) I_p(t+\tau) >_p >_t}{<< I_p(t) >_p >_t << I(t+\tau) >_p >_t} - 1 \qquad \text{(II.25)}$$

DWS Experimental set-up.

A sketch of our experimental set-up is shown in Figure II.6. The sample cells are placed in a water bath. This bath allows temperature control and is thermally isolated to avoid convection of the water. We use a solid state laser, “Verdi” from Coherent, a diode pumped Nd:YV04 with wavelength λ = 532nm, which illuminates the sample perpendicularly to the surface of the cell. The diameter of the laser beam is 3mm and we

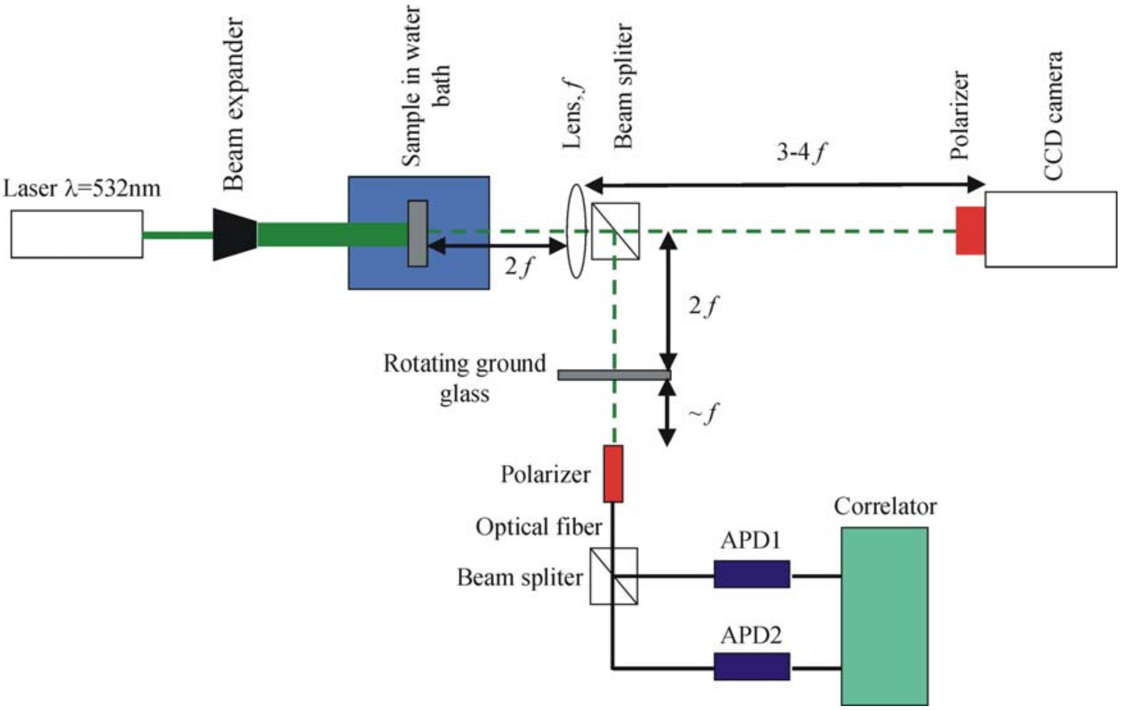
Laser λ=532nm
Beam expander
Sample in water bath
Lens, f
Beam spliter
3-4 f
Polarizer
CCD camera
2 f
2 f
Rotating ground glass
~f
Polarizer
Optical fiber
Beam spliter
Correlator
APD1
APD2

Figure II.7: Diffusing Wave Spectroscopy set-up used to study turbid systems.

expand it to 6mm with a collimator in order to illuminate the sample uniformly. We always detect scattered light in transmission geometry. We guarantee that we detect multiple scattered light by placing polarizers in front of each detector with their axis oriented to transmit light with polarization perpendicular to that of the incident beam.

The scattered light is collected by a lens, *f*=62.9mm, and split in two beams. For one of the beams, the intensity is measured in the far field with a Pulnix TM-6703 CCD camera with a 2-D array of 484(*H*)×640(*V*) square pixels, whose dimensions are 9μm×9μm. The CCD-camera is positioned in the set-up to obtain a good "signal to noise" ratio, which is the case for speckle sizes of 2-3 pixels [16]. This ratio is determined by calculating the spatial intensity correlation function, C_{sp} using a static sample.

$$C_{sp}(\Delta pix) = \frac{< I_p I_{p+\Delta pix} >_p}{< I_p >_p < I_{p+\Delta pix} >_p} - 1 \qquad \text{(II.27)}$$

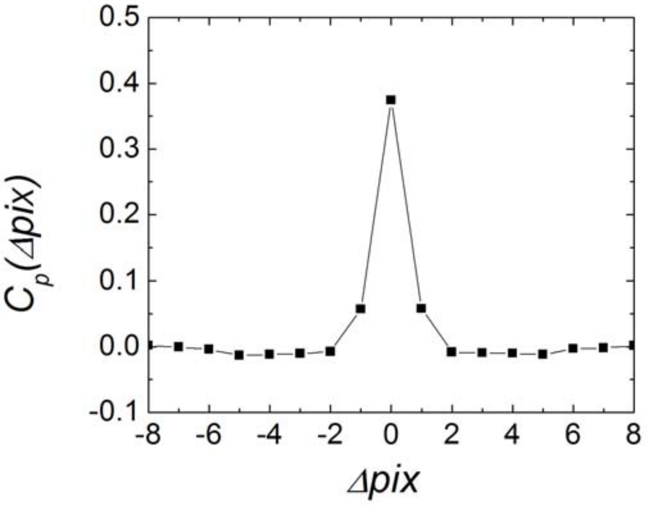

Figure II.7: Spatial intensity correlation function in vertical direction of a speckle pattern for a static sample. The first minimum of C*sp* determines the speckle size of about 2 pixels.

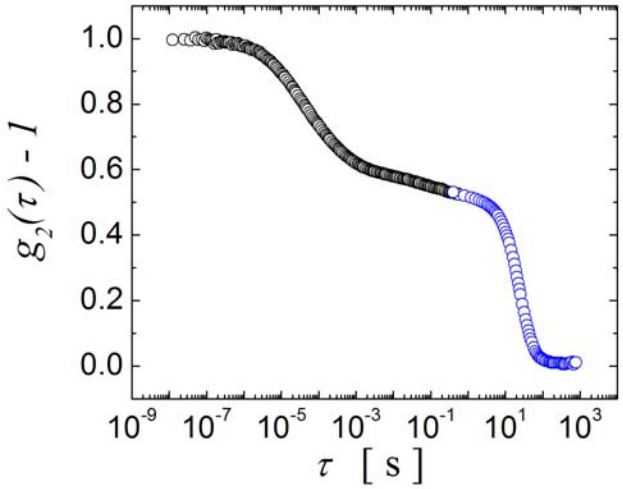

Figure II.8: Intensity correlation function of a gel of polystyrene particles of radius a = 300nm at a volume fraction $\Phi = 0.08$. Black symbols denote the measurement with a PM and blue symbols denote the measurement with a CCD-camera.

Where $I_{p+\Delta pix}$ is the intensity shifted by Δpix from I_p. The intensities of neighboring pixels remain only correlated as long they belong to the same speckle, thus the position of the first minimum of C_{sp} determines the speckle size, as shown in Figure II.7.

The intensity of the second beam is collected in the far field with a fiber and split in two equal beams, which feed two PMs. The electrical signal output of the PMs are cross-correlated with a 16-chanel correlator (ALV). This “pseudo-crosscorrelation” eliminates spurious afterpulsing at very short lag times. To solve the problem of non-ergodicity in systems such colloidal gels, we utilize a rotating piece of ground glass as a second cell. Combining CCD and PM detection schemes, it is possible to measure the intensity correlation function in a lag-time window that expands over more than ten lag-time decades, as shown in Figure II.8.

Rheology.

We study the mechanical properties of our systems while restricting our experiments to linear responses. Within this scope, viscoelastic materials such as concentrated suspensions, gels, glasses, foams or pastes are generally described as composed by a viscous Newtonian term, in which the stress and shear rate are related as $\sigma = \eta\dot{\gamma}$ and a Hookean elastic term, in which stress and strain are related as $\sigma = G\gamma$. These components are respectively conceived as a dashpot, with fluid viscosity η_{dp}, and a spring, with elasticity G_{sp}, as shown in Figure II.9. Typically, there are two strategies to explore the viscoelastic behavior of a system: to investigate the response of an applied constant strain rate or to investigate the response of an applied constant stress. Because the principle of superposition applies to linear Rheology, these two approaches are respectively represented as the association in series or in parallel of the dashpot and spring representations. These are the simplest viscoelastic models, respectively the Maxwell and Voigt-Kelvin models, as shown in Figure II.10 [4]. The Maxwell model corresponds to the association in series and describes the response of a viscoelastic system when a constant strain rate is suddenly applied and held at that value for subsequent times. The constitutive description for such system is [4]:

$$\dot{\gamma} = \frac{1}{G_{sp}}\dot{\sigma} + \frac{\sigma}{\eta_{dp}} \tag{II.28}$$

Although the system is immediately strained, the stress reaches its maximum amplitude only after a characteristic time $\tau_M = \eta_{dp}/G_{sp}$ as indicated by the solution of equation II.28:

$$\sigma(t) = \eta_{dp}\dot{\gamma}\left[1 - \exp(-t/\tau_M)\right] \tag{II.29}$$

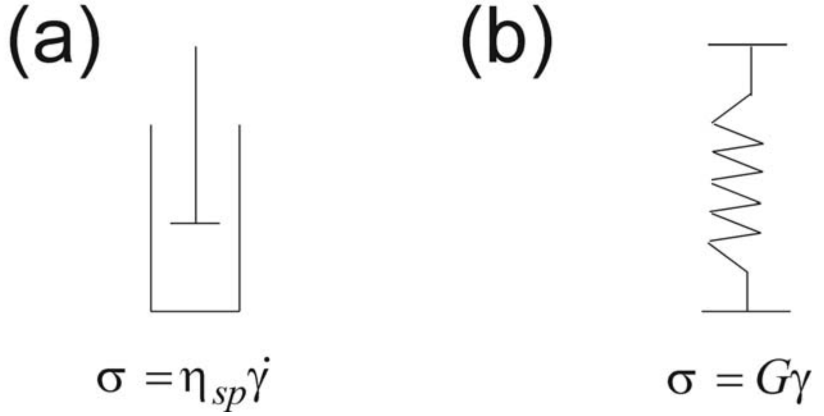
(a)
(b)
$\sigma = \eta_{sp}\dot{\gamma}$
$\sigma = G\gamma$

Figure II.9: Basic rheological elements. A viscous Newtonian fluid is conceived as a dashpot (a) and a Hookean solid is conceived as a spring (b).

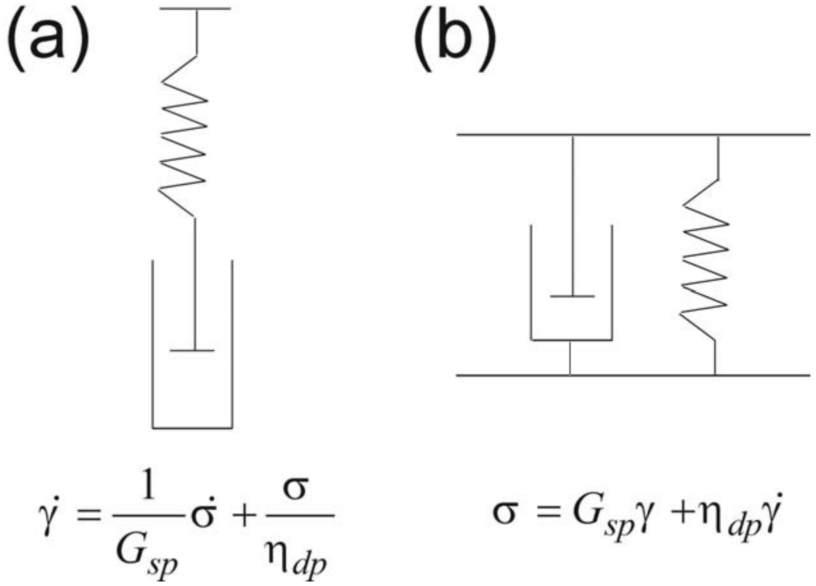
(a)
(b)
$\dot{\gamma} = \frac{1}{G_{sp}}\dot{\sigma} + \frac{\sigma}{\eta_{dp}}$
$\sigma = G_{sp}\gamma + \eta_{dp}\dot{\gamma}$

Figure II.10: Basic rheological models: (a) the Maxwell model and (b) the Voigt-Kelvin model.

If the strain rate is removed at $t = t_c$, the system relaxes in within the same characteristic time τ_M:

$$\sigma(t) = \eta_{dp}\dot{\gamma}\exp(-t/\tau_M) \qquad \text{(II.30)}$$

This strategy is often applied in so called stress-relaxation experiments, where, upon removal of the applied strain rate, the stress relaxation is measured from its equilibrium value to zero, which is the mechanical equivalent of the temperature jump and pressure jump experiments used to study chemical equilibrium.

The Voigt-Kelvin model corresponds to the association of the dashpot and the spring representations in parallel. It describes the response of a viscoelastic system when a constant stress is applied and held at that value. The constitutive description of this scheme is [4]:

$$\sigma = \eta_{dp}\dot{\gamma} + G_{sp}\gamma \tag{II.31}$$

Because the dissipative term is immediately acting, the system achieves its maximum deformation only after the characteristic time τ_M. Indeed, this is noticed by the solution of equation II.31, which yields:

$$\gamma = \sigma / G_{sp}\left[1 - \exp(-t/\tau_M)\right] \tag{II.32}$$

The response of the Maxwell model (equation II.29) resembles the Newtonian behavior of a fluid, and the Maxwell model generally applies to viscoelastic fluid systems. By contrast, the response of the Voigt-Kelvin model (equation II.32) resembles the Hookean behavior of a solid and it applies to viscoelastic solids.

There is another class of experiments where the response of these models is evaluated by applying an oscillatory strain. In an oscillatory experiment, the system is subject to a sinusoidal oscillating strain, $\gamma = \sin(wt)$, and the resulting stress is measured at different frequencies. The mechanical response of the Maxwell and Voigt-Kelvin models is quantified by solving equations II.28 and II.31; which is unified in:

$$\sigma(t) = G'(\omega)\sin(\omega t) + G''(\omega)\cos(\omega t) \tag{II.33}$$

The elements *G'(ω)* and *G''(ω)* are respectively denoted as loss and storage modulus. *G'(ω)* is the elastic term while *G''(ω)* is associated to the dissipative viscosity. For each model they are expressed as:

Maxwell model: $$G'(\omega) = \frac{G_{sp}\omega^2\tau_M^2}{1+\omega\tau_M} \qquad G''(\omega) = \frac{\omega\eta_{dp}}{1+\omega^2\tau_M^2} \tag{II.34}$$

Voigt-Kelvin model: $$G'(\omega) = G_{sp} \qquad G''(\omega) = \eta_{dp}\omega \tag{II.35}$$

Each corresponding frequency response of *G'(ω)* and *G''(ω)* is shown in Figure II.11. Note that in each case there is a crossover between *G'(ω)* and *G''(ω)* at a crossover

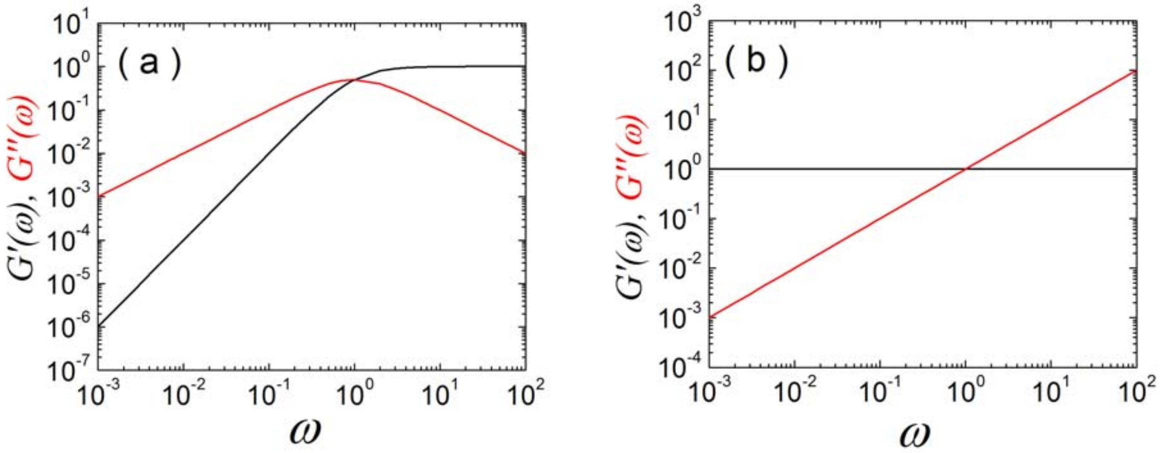

Figure II.11: Storage (black curves) and Loss (red curves) moduli corresponding to (a) the Maxwell model and to (b) the Voigt-Kelvin model upon application of an oscillatory strain. The magnitude of the elasticity and viscosity are arbitrarily fixed at G_{sp}=1 and η_{dp}=1.

frequency, ω_c, such that $G'(\omega_c) = G''(\omega_c)$. The response to an applied oscillatory strain of systems such polymer gels or colloidal glasses is twofold. At low frequencies these systems exhibit behavior corresponding to the Maxwell model while at high frequencies they exhibit behavior corresponding to the Voigt-Kelvin model [24]. Moreover, the crossover frequencies between $G'(\omega)$ and $G''(\omega)$ of each model are associated to the different relaxation times of the system. The crossover to viscous-dominated behavior at low frequencies belongs to slow relaxations, which occur over timescales where particles can access longer length scales than the cage to which they are confined. The crossover to solid-like behavior when decreasing frequency at large ω occurs because of the motion of particles trapped within cages that can not access all free volume. In the first scenario, the system is somewhat fluidized, while the second scenario corresponds to a solid and thus are respectively described with the Maxwell and Voigt-Kelvin approaches.

References.

1. P. Linder and Th. Zemb, *Neutrons, X-Rays and Light: Scattering Methods Applied to Soft Condensed Matter*. 2002, Amsterdam: Elsevier

2. B.J. Berne and R. Pecora, *Dynamic Light Scattering*. 1976, New York: Wiley.
3. Ferry, J.D., *Viscoelastic Properties of Polymers*, ed. J.W. sons. 1980, New York.
4. H. A. Barnes, J. F. Hutton, and K. Walters, *An Introduction to Rheology*, ed. Elsevier. 1998, Amsterdam.
5. Hulst, H.C.V.d., *Light Scattering by Small Particles*, ed. D. Publications. 1981, New York.
6. W. Brown, *Light Scattering: Principles and Development*, ed. C. Press. 1996, Oxford.
7. P. N. Pusey, *Dynamic Light Scattering*, in *Neutrons, X-Rays and Light: Scattering Methods Applied to Soft Condensed Matter*. 2002, Amsterdam: Elsevier p. 203-220.
8. P. N. Pusey, *Introduction to Scattering Experiments*, in *Neutrons, X-Rays and Light: Scattering Methods Applied to Soft Condensed Matter*. 2002, Amsterdam: Elsevier p. 3-21.
9. P. Debye, *Molecular-Weight Determination by Light Scattering.* Journal of Physical and Colloid Chemistry, 1947. **51**: p. 18-32.
10. A. Guinier and G. Fournet, *Small-Angle Scattering of X-Rays*. 1955, New York: Wiley Interscience.
11. R. Klein, *Interacting Colloidal Suspensions*, in *Neutrons, X-Rays and Light: Scattering Methods Applied to Soft Condensed Matter*. 2002, Amsterdam: Elsevier p. 351-379.
12. J. K. Percus and G. J. Yevick, *Analysis of Classical Statistical Mechanics by Means of Collective Coordinates.* Physical Review, 1958. **110**(1): p. 1-13.
13. F. J Rogers and D. A. Young, *New, thermodynamically consistent, integral equation for simple fluids.* Physical Review A, 1984. **30**(2): p. 999-1007.
14. P. Schurtenberger, *Contrast and Contrast Variation in Neutrons, X-Ray and Light Scattering*, in *Neutrons, X-Rays and Light: Scattering Methods Applied to Soft Condensed Matter*.2002, Amsterdam: Elsevier p. 203-220.
15. D.A. Weitz and D. J. Pine, *Dynamic Light Scattering*, ed. C.P. Oxford. 1993. 652.

16. V. Viasnoff, F. Lequeux, and D. J. Pine, *Multispeckle diffusing-wave spectroscopy: a tool to study slow relaxation and time-dependent dynamics.* Review of Scientific Instruments, 2002. **73**(6): p. 2336-2344.
17. J. Z. Xue, et al., *Nonergodicity and light scattering from polymer gels.* Physical Review A, 1992. **46**(10): p. 6550-6563.
18. J. G. H. Joosten, E. T. F. Gelade, and P. N. Pusey, *Dynamic light scattering by nonergodic media: Brownian particles trapped in polyacrylamide gels.* Physical Review A, 1990. **42**(4): p. 2161-2175.
19. P. N. Pusey and W. Van Megen, *Dynamic light scattering by non-ergodic media.* Physica A, 1989. **157**(2): p. 705-741.
20. F. Scheffold, et al., *Diffusing-wave Spectroscopy of Nonergodic Media.* Physical Review E, 2001. **63**(6): p. 061404-11.
21. L. Cipelletti, et al., *Time-resolved Correlation: a new tool for studying temporally heterogeneous dynamics.* Journal of Physics: Condensed Matter, 2003. **15**(1): p. S257-S262.
22. A. Duri, et al., *Time-resoved Correlation Measurements of Temporally Heterogeneous Dynamics.* Physical Review E, 2005. **72**: p. 051401-17.
23. A. Duri, et al., *Fluctuations and Noise in Time-resolved Light Scattering Experiments: Measuring Temporally Heterogeneous Dynamics.* Fluctuation and Noise Letters, 2005. **5**(1): p. L1-L5.
24. J. Goodwin, *Colloids and Interfaces with surfactants and Polymers*, 2005, Sussex: John Wiley and Sons.

Chapter III.

Short-time Dynamics and Rheology of Weakly Aggregated Colloidal Gels.

Introduction.

The study of attractive colloidal particles depends on our ability to finely tune the nature of the attraction. Attraction is an inherent property of colloids, where the colloid is prevented of aggregation solely by appropriated surface modification. The two main routes to stabilization are surface charges and steric repulsion [1]. Each of these routes provides means to tailor the inter-particle interactions by controlling both the magnitude and range of the repulsive interaction, and balancing this with the intrinsic Van der Waals attraction between the particles. The long-range Coulomb repulsion of charged particles can be drastically reduced, or even completely eliminated by screening the charges through addition of electrolyte to the solution, or by neutralizing the surface charges on the particles. Similarly, the shorter-range steric repulsive barrier can be adjusted by varying the thickness of the stabilizing layer on the particle surfaces. This is traditionally accomplished by varying either the density or the length of the molecules that are adsorbed on the particle surface.

In this study we adopt the scheme of a variation in the steric stabilization layer to adjust the attraction between colloids. We develop and investigate three systems. The first one is an industrial system composed of zinc-oxide particles dispersed in mineral oil and coated with various amount of a polymeric dispersant. For the second system we adsorb a triblock copolymer on otherwise charge stabilized latex spheres so that to achieve a surface coverage of 60%; aggregation is then obtained by screening the particle charge. As a third system, we use polystyrene particles with a chemically grafted brush of Poly-N-isopropyl acrylamide (PNiPAM) on the surface; heating the system above the lower critical temperature of PNiPAM leads to a collapse of the brush and consequently to aggregation. We study the dynamics and mechanical properties of these aggregated systems by performing Diffusion Wave Spectroscopy and oscillatory shear experiments.

Experimental Systems: Preparation and Characteristics.

Solsperse 3000 coated ZnO particles.

Our ZnO-particles are commercial particles (Z-Cote^{TM}HP-1, BASF) that are highly anisotropic and polydisperse, as shown in Figure III.1(a), where we display an image of the dry powder obtained by scanning electron microscopy (SEM). From dynamic light scattering experiments we determine the average hydrodynamic radius of these particles to be $<R_H> = 102$ nm. As suspending medium we use a mineral oil (Sigma-Aldrich) with a density of $\rho = 0.838$ g cm^{-3} and a viscosity of $\eta = 24.5$ mPa s (25°C); as polymeric dispersant we use Solsperse^{TM}3000 from Avecia. Both, ZnO and Solsperse are mixed into the mineral oil, subsequently sonicated for 30 minutes and finally left for tumbling at 5rpm until use.

Evidence that our polymeric dispersant is effectively grafting onto the ZnO surface is shown in Figure III.1(b), where we display micrographs obtained by optical microscopy (OM) for samples with 10w% ZnO-particles. For the sample without dispersant the particles are aggregated forming a coarse network. By contrast for the sample with a large amount of dispersant the particles are well dispersed exhibiting Brownian motion. For samples with smaller amounts of dispersant (images not shown) we observe the formation of less coarse networks with some freely diffusing particles in the continuous phase.

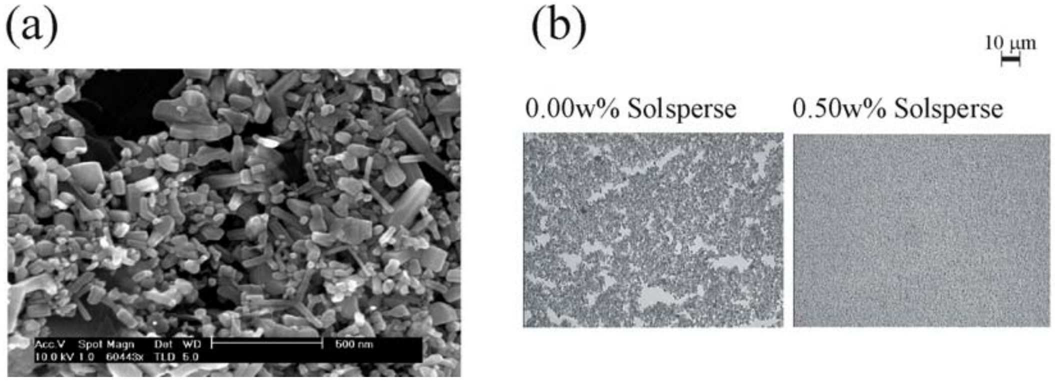

Figure III.1: (a) SEM image of the bare ZnO system. (b) OM image of Solsperse-coated ZnO particles at a ZnO concentration of 10w% and surfactant concentrations of 0.00w% (left) and 0.50w% (right).

Pluronic f68 coated polystyrene particles.

The particle systems used in this study are aqueous suspensions of sulfated polystyrene particles from Interfacial Dynamics Corporation (IDC) that have a surface charge density of $\sigma_0 = 3.8\mu C/cm^2$ and radii of $a = 340nm$. With no added electrolyte the surface charge stabilizes the suspension against aggregation. For the partial steric stabilization of the particles we use a commercial triblock copolymer from BASF Corp., Pluronic f68. Pluronic f68 is a Poly(ethylene)-Poly(propylene)-Poly(ethylene)Oxide (PEO-PPO-PEO) triblock copolymer with a molecular weight of 8350g/mol and is used without previous purification. In water the hydrophobic PPO-block adsorbs onto the surface of the polystyrene particles, while the PEO-blocks are water soluble and thus act as steric stabilization layer.

Partially sterically stabilized particles are prepared by adding 0.866ml of an aqueous Pluronic f68 solution (10^{-2}g/ml) to 20ml of bare latex at a volume fraction $\Phi = 0.077$, which leads to a volume fraction of $\Phi = 0.074$ and to an overall Pluronic f68 concentration of $C_{TOTAL} = 3.85 \cdot 10^{-4}$ g/ml. The system is then left to equilibrate while tumbling for a period of 12h. Pluronic adsorption on polystyrene is described by a Langmuir adsorption isotherm [2] :

$$C_{TOTAL} = \frac{3\Phi}{a(1-\Phi)} \cdot \frac{\Gamma_M}{1 + B / C_{FREE}} + C_{FREE} \qquad \text{(III.1)}$$

where $C_{TOTAL} = C_{ADS} + C_{FREE}$ is the overall Pluronic concentration, which is the sum of the Pluronic concentration adsorbed on the surface, C_{ADS}, and the Pluronic concentration remaining in the solvent, C_{FREE}; Γ_M is the mass of Pluronic per unit area obtained at maximal surface coverage and B is a material specific concentration [3]. The magnitude of both Γ_M and B are reported in ref. [4], which enables us to determine the free Pluronic concentration in our preparation to be $C_{FREE} = 1.2 \cdot 10^{-5}$g/ml, which corresponds to 60% coverage according to the measurements reported in [5]. The system is then concentrated up to a volume fraction $\Phi = 0.18$ with a Millipore 8010 Stirred Ultrafiltration Cell. The remaining supernatant is kept and all posterior dilutions are done with this polymer solution, which guarantees that the surface coverage does not vary from one sample to another.

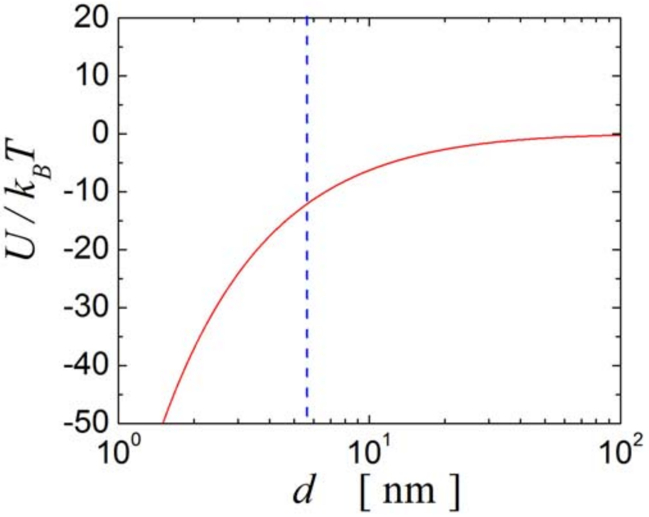

Figure III.2: Sketch of the particle-particle interactions expected for the Pluronic-coated PS-particle system. The red line is the Van der Waals attractive potential of the bare PS. The blue line indicates the position of the steric barrier.

The brush thickness for a fully saturated polystyrene surface has been reported to be $L_F \sim$ 7nm [4, 5]. To estimate the brush thickness at 60% coverage, we assume that the mean distance between anchoring chains, s_C, depends on the mean distance at full coverage, s_F, and the fraction of coated surface ξ as $s_C = \xi^{-2/3} s_F$. The thickness of a polymer brush in a solvent-favorable environment is $L_C = n^{5/3} l / s_C^{2/3}$, n being the number of segments with a Kuhn length l [6]. Therefore $L_C = \xi^{4/9} L_F$ and $L_C(\xi = 0.6) \sim$ 5.6nm for the Pluronic-coated particles. This length determines the range of the steric repulsion, which for our particles cuts off the Van der Waals attraction so that the minimum potential is $U_{min}/k_B T = -12.5$, as sketched in Figure III.2.

As mentioned above our particles are also charged stabilized, which effectively prevents them from aggregation prior to our destabilization experiment. We destabilize our suspensions by gradually screening the Coulomb-repulsion using the in situ destabilization method described in [7, 8]. This method takes advantage of the urease catalyzed hydrolysis of urea to obtain homogeneously screened particle suspensions. The enzyme urease is inactive below T = 5°C, above this temperature it catalyses the hydrolysis of urea:

$$(NH_2)_2CO + 2H_2O \rightarrow NH_4^+ + NH_3 + HCO_3^-$$

Thus, to achieve homogeneous destabilization we thoroughly mix our suspensions with urea and urease solutions at a temperature below 5°C. Raising the temperature to 20°C leads then to an activation of the urease that catalyzes the hydrolysis of urea, which leads to a gradual increase of the ionic strength and eventually to aggregation of our particles. We study the aggregated phases in a particle volume fraction range of 0.03-0.15, maintaining the free volume concentrations of urea and urease respectively at 0.3 molar and 60u/ml.

To evaluate the evolution of the ionic strength during our experiment we measure the conductivity during the urea-urease reaction using this set of urea and urease concentrations in (a) pure water and (b) an aqueous solution of Pluronic-f68 at 10^{-2} g/ml. In both cases, we find the conductivity to increase linearly in time becoming constant at t = 7200s, as shown in Figure III.3(a). Using the calibration curve reported in [9] we convert the conductivity to ionic strength, as shown in Figure III.3(b). We calculate the

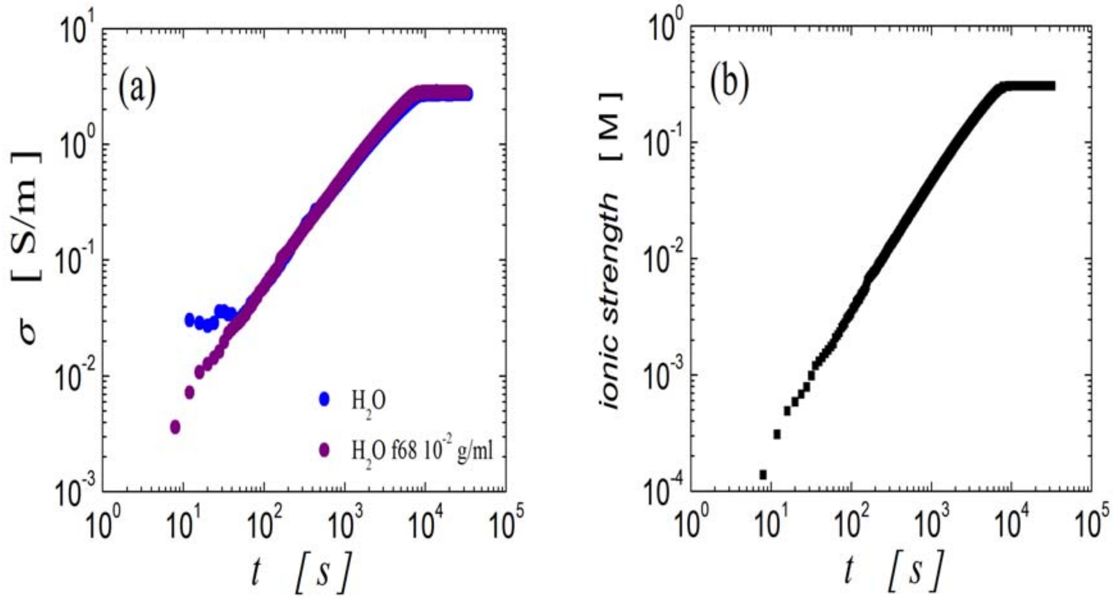

Figure III.3: (a) Temporal evolution of the conductivity during the urea-urease reaction in pure water (blue circles) and in a 10^{-2} g/ml solution of Pluronic f68 (purple circles). In both cases the urea concentration is 0.3 molar and the urease concentration is 60 u/ml. (b) Temporal evolution of the ionic strength as obtained by transforming the temporal evolution of the conductivity using the reference curve reported in reference [9].

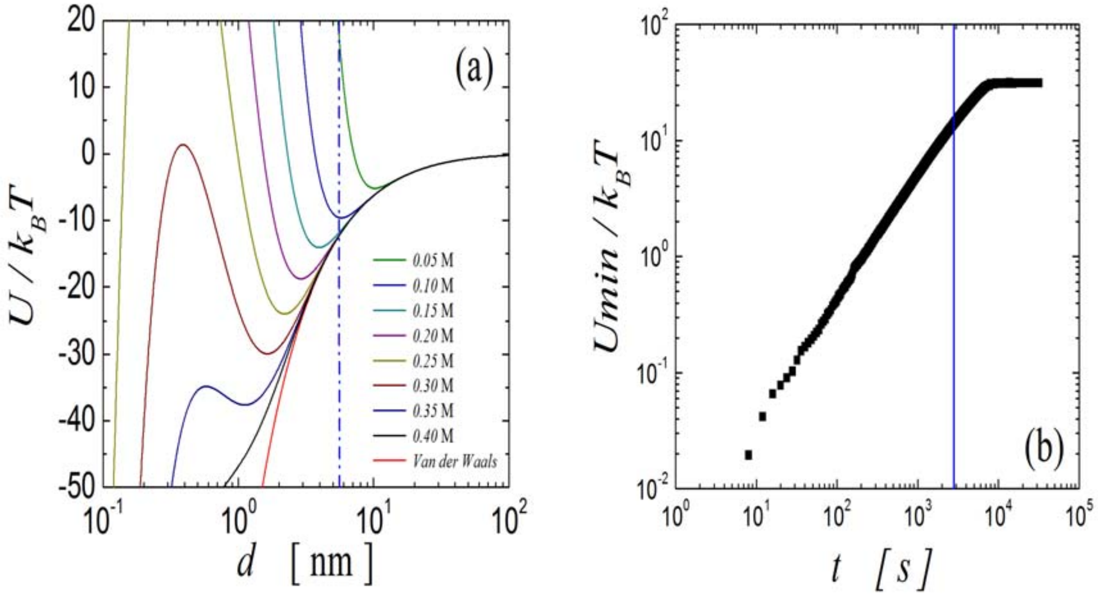

Figure III.4: (a) DLVO potential corresponding to the bare PS used in the Pluronic-coated PS-particle system, for an ionic strength of 0.05 molar (green line), 0.10 molar (blue line), 0.15 molar (cyan line), 0.20 molar (purple line), 0.25 molar (yellow line), 0.30 molar (brown line), 0.35 molar (dark blue line) and 0.40 molar (black line). The red line indicates the Van der Waals attraction and the blue dashed line the position of the steric brush. (b) Temporal evolution of the secondary DLVO minimum during the urea-urease reaction. The curve is obtained by relating the evolution of the ionic strength to its corresponding DLVO minimum. The blue line denotes the cut off to the DLVO attraction established by the steric brush of Pluronic f68.

DLVO particle interaction for a series of ionic strengths, showing the result in Figure III.4(a). By relating the DLVO potential to the temporal evolution of the ionic strength, we find the secondary DLVO minimum to evolve linearly in time, as shown in Figure III.4(b). At $t \geq 2850$s (ionic strength 0.133 molar) the steric repulsion becomes larger ranged than the DLVO attraction and although the DLVO minimum evolves further until all urea is hydrolyzed, this moment corresponds to the time at which the particle-particle interactions ceases to evolve. We define the start of our experiment at $t = 0$s as the moment at which the suspensions are mixed with the urea and urease solutions and study the system at $t = 10800$s in a volume fraction range of $\Phi = 0.03$ to $\Phi = 0.15$.

PolyN-isopropylacrylamide (PNiPAM) coated polystyrene particles.

We prepare PNiPAM coated polystyrene particles according to [10]. The emulsion polymerization is done using a 1-L flask equipped with a stirrer, a reflux condenser, and a thermometer. Sodium dodecyl sulfate (SDS, 0.097g) and N-isopropylacrylamide NiPAM (1.875g) are dissolved in pure water (262g). While stirring, this solution is degassed by repeated evacuation. After addition of styrene (71.271g), the mixture is heated to 80 °C under nitrogen atmosphere. The initiator potassium peroxodisulfate (KPS, 0.176g dissolved in 7.5ml water) is added while the mixture is stirred at 400 rpm. After 8 h the latex is cooled to room temperature and purified by extensive dialysis of the latex against $2.5 \cdot 10^{-3}$ molar sodium thiocyanate (NaSCN) solution.

The thus obtained particles have a radius of a = 181nm as determined by Dynamic and Static Light Scattering. We find that the measured static light scattering exhibits a deep minimum at $qa \sim 4.6$ and that the intensity autocorrelation functions are single exponentials, which indicate that our particles are reasonably monodisperse. We characterize their zeta-potential as a function of salt concentration at a temperature T = 20°C using sodium thiocyanate (NaSCN). We find the zeta-potential to significantly increase up to a NaSCN concentration of 0.15 molar to then remain approximately constant at ζ = -30mV in the concentration range of 0.15 to 0.3 molar, as shown in Figure III.5(a). Using our measured zeta-potential we calculate the DLVO potentials of our particles with the result shown in Figure III.5(b).

For our experiment we choose to set the ionic strength to a free volume concentration of 0.3 molar, which corresponds to a DLVO potential with no effective Coulomb repulsion (see Figure III.5(b)). Despite the high ionic strength our particle suspensions are stable provided that they are kept at low temperature. This is due to the PNiPAM layer on the particles that effectively sterically stabilizes the particles at low temperature. PNiPAM belongs to the class of water soluble polymers that exhibit a Lower Critical Solution Temperature (LCST); below the LCST PNIPAM is soluble, above the LCST it is not. This unusual temperature dependence is generally attributed to the formation of hydrogen bonds between the water and PNIPAM that breaks up as the temperature is increased. Indeed the semi-order of the water around the PNIPAM needed to solubilize PNIPAM made us choose NaSCN as screening agent, as this is a salting-in salt, which does not significantly alter any longer-range order in water. We take advantage of the PNiPAM LCST being 32°C [11] to start our experiments at 20°C, where the system is a stable suspension. Raising the temperature to 40°C leads to a collapse of the PNIPAM layer and consequently to aggregation of our particles. We find that this process is not completely reversible; decreasing the temperature again to 20°C does not lead to a fully dispersed state again. This indicates that the collapsed PNIPAM-layer is small enough to allow the Van der Waals interactions between the polystyrene cores to be effective. We define the start of our experiments at $t = 0$s as the moment we set the temperature to increase from 20°C to 40°C and investigate the aggregated states at $t = 8$h in a volume fraction range of $\Phi = 0.04$ to $\Phi = 0.30$.

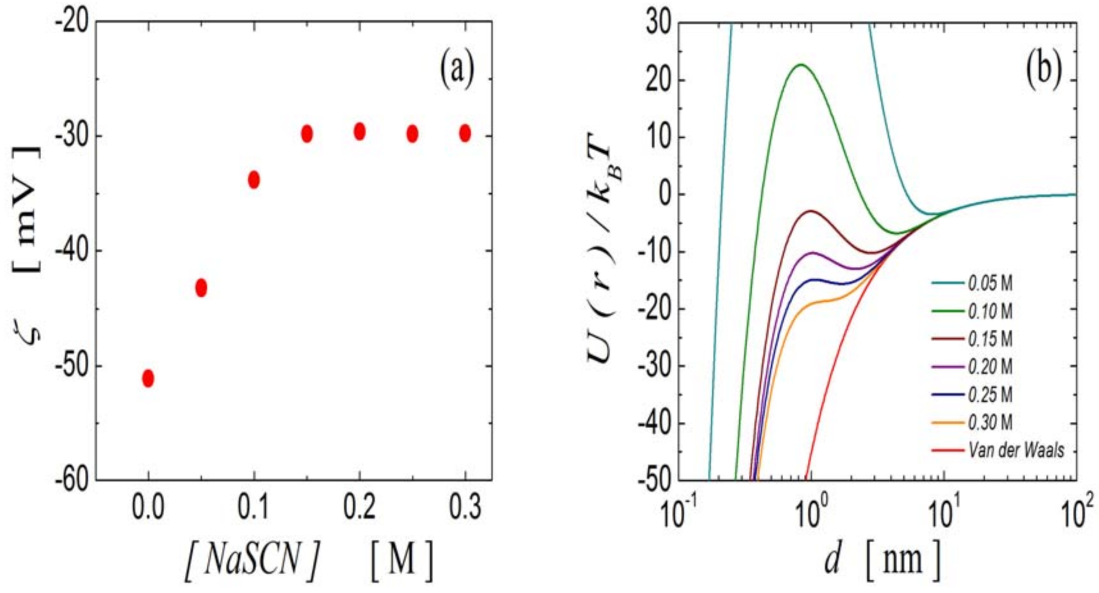

Figure III.5: (a) Zeta potential of PNiPAM coated PS-particles as a function of NaSCN concentrations. (b) DLVO potential for PNiPAM coated PS-particles calculated using the zeta potential and the corresponding ionic strength as inputs.

Results and Discussion.

Because of the high turbidity of all our systems we study the dynamics of their aggregated states by Diffusing Wave Spectroscopy. The experiments are performed in the transmission geometry using the set-up described in Chapter II. For the Pluronic-coated PS-particle and the PNiPAM-coated PS-particle systems we use scattering cells of thickness L = 1mm; for the Solsperse-coated ZnO-particle system we use scattering cells of thickness L = 2mm. In all cases $L/l^* > 10$, which ensures that the diffusion approximation for multiple scattered light applies [12].

In this chapter we describe the results obtained by using the point detector scheme described in Chapter II. The correlation functions obtained at different concentrations for the three systems investigated are shown in Figure III.6(a), (b) and (c), where we normalize the lag-time axis with $(L/l^*)^2$ to account for changes in the turbidity of our systems. We find that a full decay is only observed for the Solsperse-coated ZnO-particle system. The correlation functions of the Pluronic-coated PS-particle system and of the PNiPAM-coated PS-particle system exhibit a fast relaxation process followed by a plateau regime. The height of this plateau systematically increases with increasing particle volume fraction. We convert the correlation functions into their correspondent mean-square displacements (MSDs) with results shown in Figure III.6(a'), (b') and (c'). The time dependence of the MSDs exhibits features that are similar to the one found for strongly aggregated gels [13, 14]. At short lag times the MSDs exhibit an increase with time, which is common to all volume fractions. For lower Φ this increase extends to larger lag-times before converging to a constant value, δ^2, where δ^2 is a measure of the maximal excursion of the particles. For higher Φ the MSD converges to δ^2 at shorter lag times. Clearly, the time dependence of the MSD is determined by two characteristics, the cross-over time from the subdiffusive regime to the plateau regime, τ_c, and the plateau value δ^2. To obtain τ_c and δ^2 we use a scaling technique that consists of normalizing the time-axis with τ_c and the MSD-axis with δ^2, so that to obtain the best possible overlap of the data obtained at different Φ. The resulting master-curves obtained using this technique are shown in Figure III.7(a), (b) and (c). It is worth noticing that this scaling technique enables us to determine τ_c and δ^2 with a good relative accuracy; though the

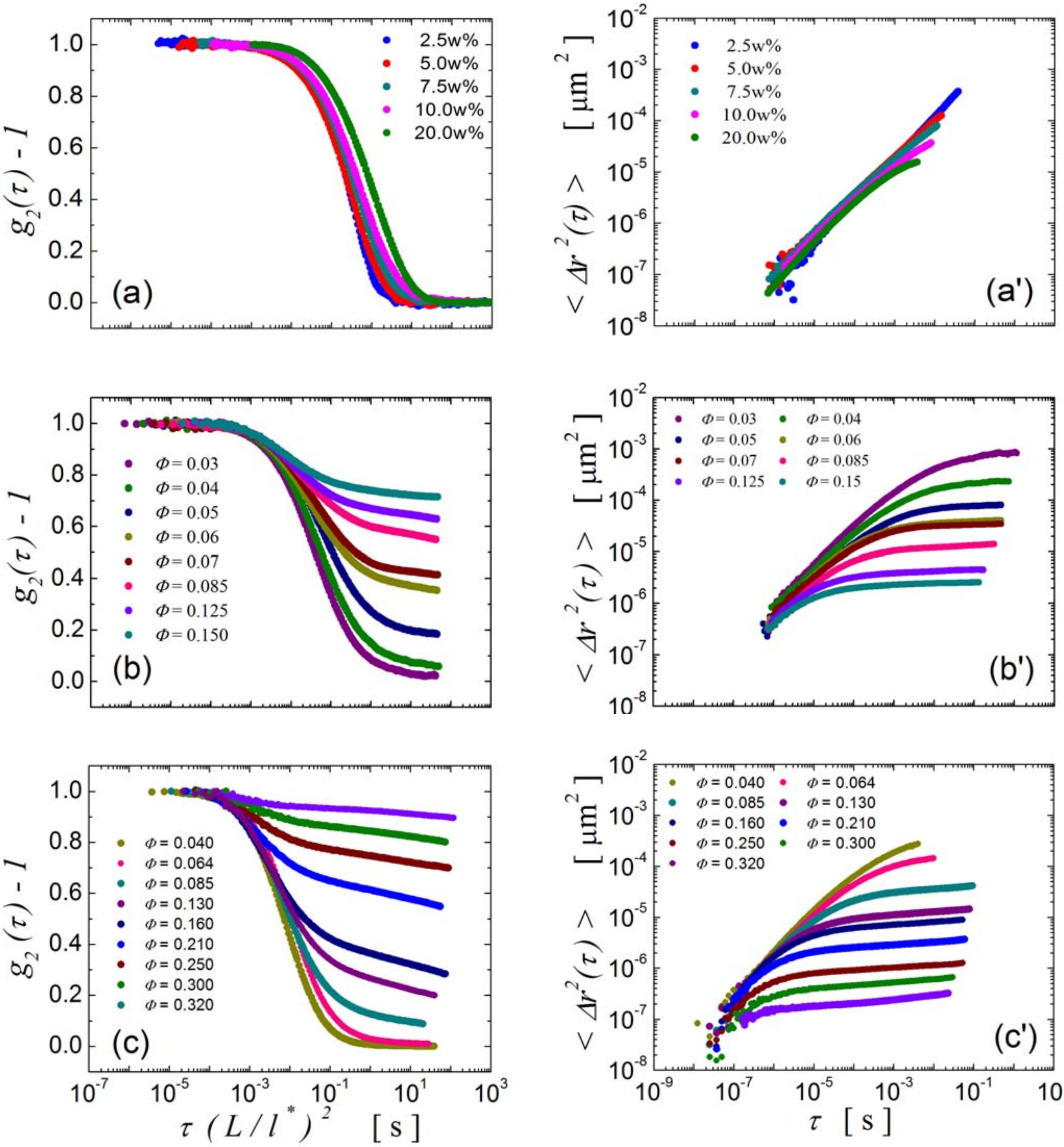

Figure III.6: Correlation functions obtained for (a) the Solsperse-coated ZnO-particle gels, (b) the Pluronic-coated PS-particle gels and (c) the PNiPAM-coated PS-particle gels. The corresponding time-dependencies of the MSD are shown in (a'), (b') and (c'). Indications of the volume fractions used are given in the figures.

absolute magnitude of both values might have a rather large error, the relative errors are small. For each system we find that τ_c and δ^2 are related by a power-law with an

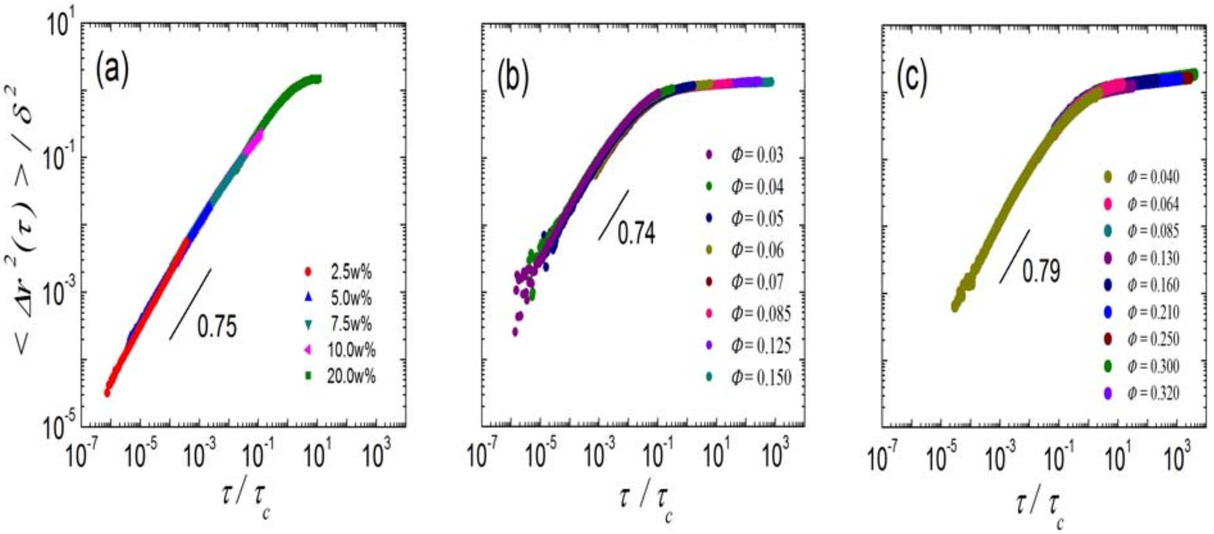

Figure III.7: MSDs scaled onto respective mastercurves for gels composed by (a) Solsperse-coated ZnO-particles, (b) Pluronic-coated PS-particles and (c) PNiPAM-coated PS-particles.

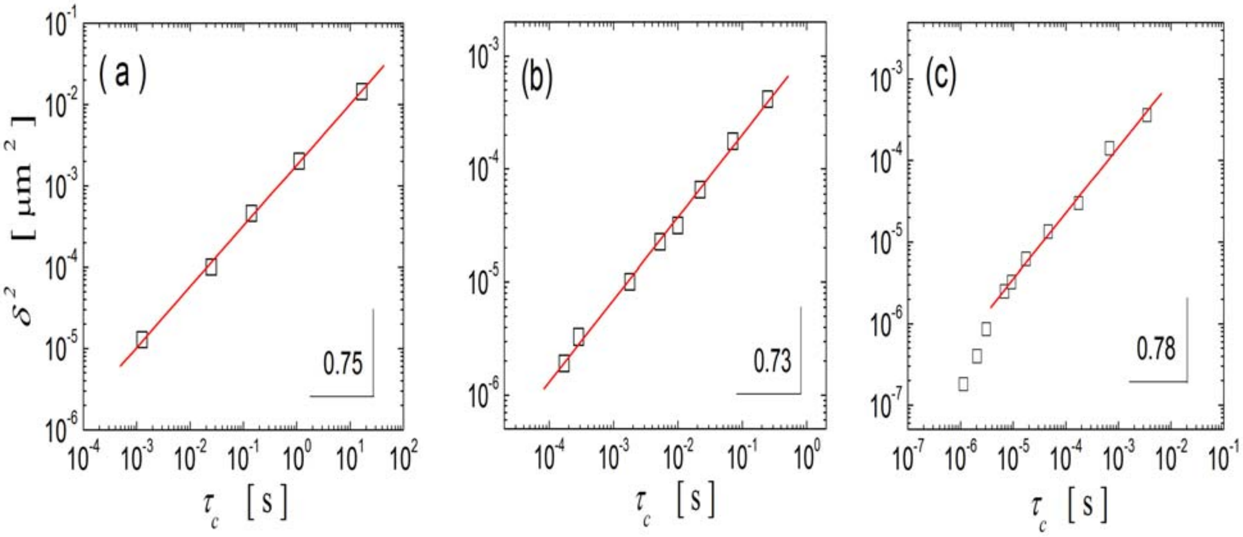

Figure III.8: Parametric plot of the scaling parameters used to scale the MSDs of (a) Solsperse-coated ZnO-particle gels, (b) Pluronic-coated PS-particle gels and (c) PNiPAM-coated PS-particle gels.

exponent of 0.75, 0.73 and 0.78 for respectively the Solsperse-coated ZnO-particle system, The Pluronic-coated PS-particle system and the PNiPAM-coated PS-particle system, as shown in Figure 8(a), (b) and (c). We note, however, that for the PNiPAM-coated PS-particle system the relation deviates for the lowest magnitudes of δ^2 and τ_c, which belong to volume fractions above 0.2.

In addition to the study on the dependence on volume fraction, we study the dynamics of our ZnO-particle system as a function of Solsperse concentration, which sets the particle-particle interaction within this system. We use a ZnO concentration of 10w%, and vary the Solsperse concentration in a range between 0.00w% and 0.50w%. For all Solsperse concentrations, we find the correlation functions to fully decay, the relaxation process becoming slower as the Solsperse-concentration increases (data not shown). For the maximum Solsperse concentration of 15w% the lag-time dependence of the MSD is linear, which is a typical characteristic of freely diffusing particles. With no dispersant the MSD exhibits the constraint subdiffusive behavior that is characteristic for the gel phase, as shown in Figure III.9(a). Indeed, these two samples respectively correspond to a fully dispersed phase and a fully aggregated phase, as denoted in the OM-micrographs in Figure III.1(b). In the intermediate range of dispersant concentrations we observe a

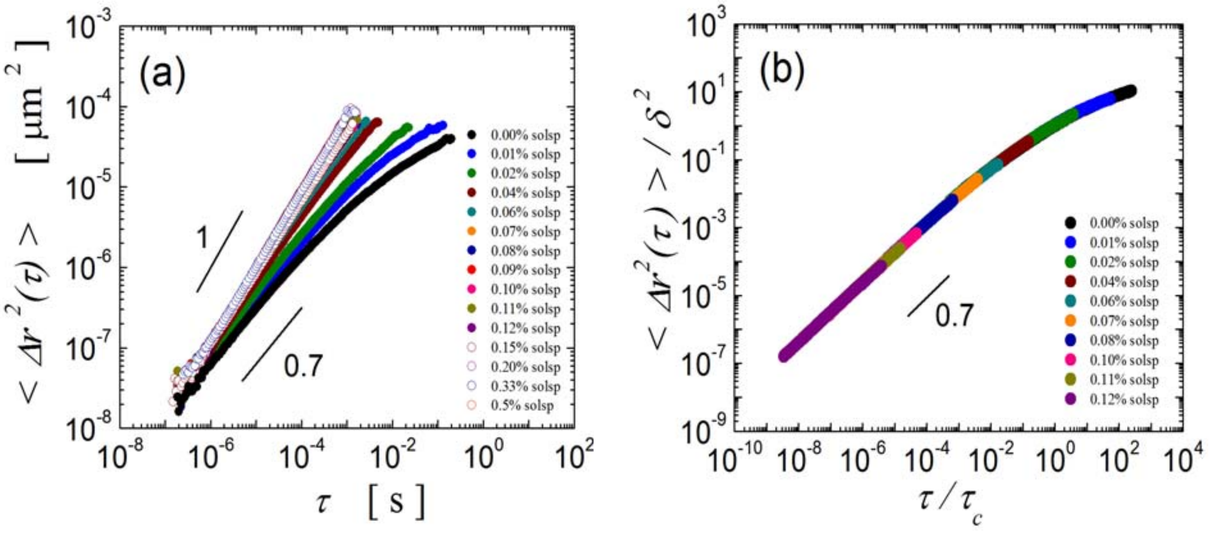

Figure III.9: (a) Dynamics of the Solsperse-coated ZnO-particle system at a ZnO concentration of 10w% and varying dispersant concentration. (b) Scaled master-curve of the MSDs corresponding to the solid phases. The different dispersant concentrations are indicated in the figure legends.

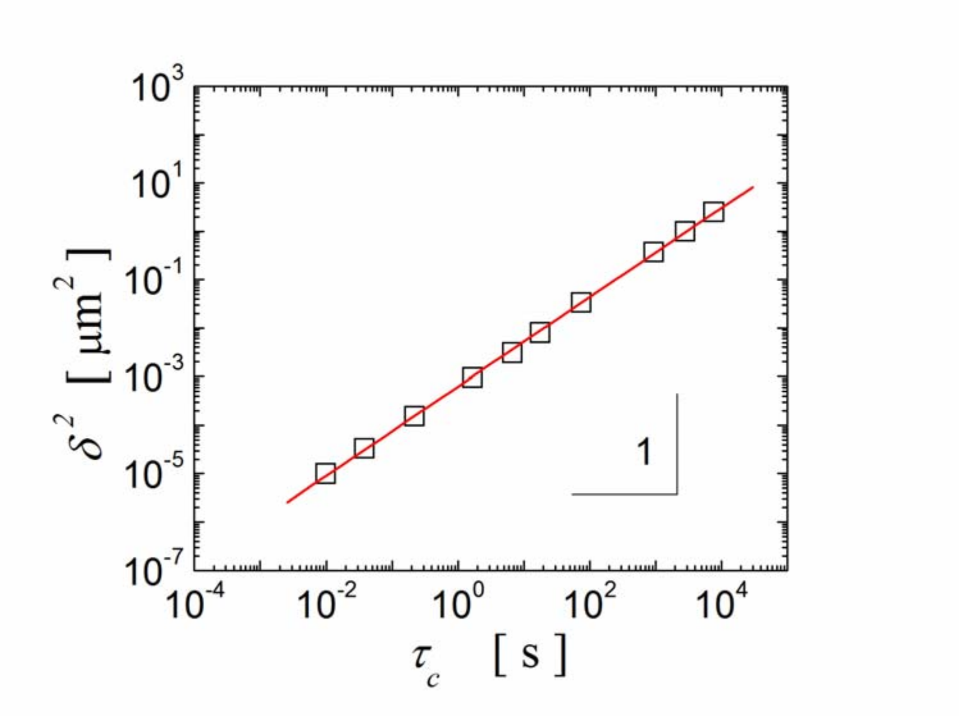

Figure III.10: Parametric plot of the scaling factors used for scaling the dynamics of Solsperse-coated ZnO-particle gels at a ZnO concentration of 10w% and varying surfactant concentration.

crossover from solid-like to fluid-like behavior. To determine the precise location of the boundary between fluid state and solid state, we take advantage of the scaling behavior that we have found to apply to the solid state. Thus, we define samples for which the time dependent MSDs can be scaled onto the one of the dispersant-free sample as solids; samples for which the time dependent MSDs can not be scaled onto the one of the dispersant-free sample as fluids. From our scaling procedure of the MSDs to a master curve (Figure III.9(b)) we again obtain δ^2 and τ_c with good relative accuracy. Both parameters relate linearly to each other, as shown in Figure III.10; this is in contrast to the relation found for the volume fraction variation at fixed particle-particle interaction, where $\delta^2 \sim \tau_c^{0.75}$.

To account for the observed dynamics we consider a model that has been introduced to describe the arrested dynamics of fractal gels with a characteristic length R_c; this length being defined as the limiting length above which the structure appears homogeneous, below which the structure is defined by its fractal character. This characteristic length is typically set by the particle volume fraction,

$$R_c / a \sim \phi^{1/(d_f - 3)} \tag{III.2}$$

where a is the size of the particle and d_f the fractal dimension [15]. For the description of the dynamics of such fractal gels Krall and Weitz [16] proposed to assume that the internal fluctuations within the fractal cluster of size R_c can be described as a superposition of modes each being assigned to a subcluster of size s. Each mode is treated as an independent, overdamped harmonic oscillator characterized by a spring constant κ_s and a relaxation time $\tau_s = 6\pi\eta\, s/\kappa_s$; the slowest and floppiest mode is the one corresponding to the cluster size ($s = R_c$) and sets the magnitude of the maximum mean squared displacement δ^2. In the limit of short times this model yields that $<\Delta^2 r(\tau)> \sim \tau^p$ with $p = (2 + d_b)/(3 + d_b)$ and d_b the backbone dimension, which typically varies between 1 and 1.5 depending on the aggregation mechanism [17, 18]. Thus, p varies between 0.75 and 0.78, which is in good agreement with our experimental results (see Figure III.7(a), (b) and (c)). Moreover, the relation between δ^2 and τ_c found for the variation in ϕ corresponds to $\delta^2 \sim \tau_c{}^p$, which is in perfect agreement with the model as well. Indeed, for a given particle-particle spring constant we expect the short time behavior of the MSDs to be identical at different volume fractions as long as we probe internal fluctuations below the cluster size. Varying the volume fraction leads to a variation of the characteristic cluster size, which sets the onset to the plateau regime in the time dependence of the MSDs, but does not lead to a change in the fluctuation spectrum at short time, as the subclusters and their corresponding modes are identical for fractals of different sizes. Thus, our scaling technique consists of shifting the time dependent MSDs along the short time spectrum; this spectrum being described by $<\Delta^2 r(\tau)> \sim \tau^p$ we therefore find that $\delta^2 \sim \tau_c{}^p$.

To account for the linear dependence between δ^2 and τ_c found for a variation in the particle-particle interactions at a given volume fractions we consider another result of the Krall-Weitz model, where it can be shown that $\tau_c \sim R_c/\kappa_c$ and $\delta^2 \sim 1/\kappa_c$ and thus $\tau_c \sim R_c\, \delta^2$. Our results obtained with the ZnO-Solsperse system therefore imply that the characteristic length of our system does not vary as the Solsperse concentration is varied, such that $\tau_c \sim \delta^2$. In turn this implies that the characteristic length of our gels is entirely set by the particle volume fraction.

That the Krall-Weitz model seemingly describes the dynamics of all our systems is surprising, as it is based on fractal arguments. Though we can conceive that the Pluronic- and PNiPAM-coated particle systems exhibit an aggregational behavior that resembles diffusion-limited aggregation, the ill-defined Solsperse-coated ZnO-system exhibits the exact same scaling behavior as the more model-type systems. More importantly, we designed all our systems, such that to be more weakly interacting than the systems that exhibit DLCA [15, 16, 19]. Thus, we would in principle expect that bonds that are formed between particles can also be broken, such that the gels could coarsen. Indeed, as seen in the optical micrographs displaying the structure of the ZnO-gels (see Figure III.1(b)) we find that this system is rather compact, better described by an assembly of flocs, rather than fractal clusters. However, we find that the basic features in the dynamics of this system can be described in the same terms as the one used for fractals. Thus, our findings indicate that the Krall-Weitz-model is more generally applicable than only to fractal gels, as long as the volume fraction is below 0.1.

In addition to the study of the dynamics, we explore the elastic properties of the Solsperse-coated ZnO-particle system. In Figure III.11(a) we show the frequencydependence of the storage $G'(\omega)$ and loss moduli $G''(\omega)$ obtained for the ZnO-concentration series for which the dispersant concentration is maintained fixed at a concentration of 0.02w%. At 10w% concentration of ZnO, the suspensions are clearly elastic; $G'(\omega)$ is nearly frequency independent and larger than $G''(\omega)$. As the ZnO concentration decreases, the magnitude of $G'(\omega)$ decreases and becomes increasingly dependent on frequency. For the lowest ZnO concentrations, a cross-over frequency, ω_c, can be identified, above which $G''(\omega)$ dominates over $G'(\omega)$. Maintaining the ZnO concentration at 10w%, a variation of the dispersant of the surfactant leads to a similar development of the rheological response function. At low dispersant concentrations the suspensions clearly exhibit elastic behavior, as shown in Figure III.11(b). When the dispersant concentration is increased, the magnitude of $G'(\omega)$ gradually decreases and a cross over frequency appears in the investigated range of frequencies.

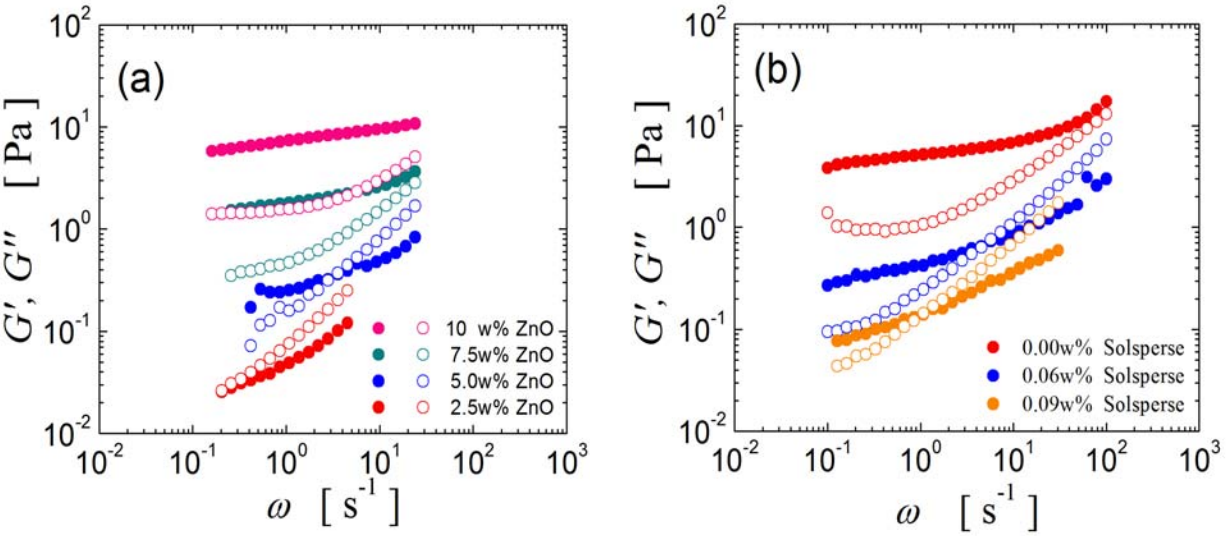

Figure III.11: Frequency dependence of the storage modulus G' (closed symbols) and loss modulus G'' (open symbols) obtained for the Solsperse-coated ZnO-particle gels at (a) varying ZnO concentration and at (b) varying surfactant concentration. The legends in the figures respectively indicate the different concentrations of ZnO and Solsperse.

The material response functions can be scaled onto a universal master curve by shifting the frequency and both moduli, as shown in Figure III.12(a) and Figure III.12(b). This scaling behavior has been previously observed for carbon black suspended in mineral oil [20], where similarly to the experiments presented here the particle and dispersant concentrations are varied in independent series. This scaling behavior can be rationalized considering a simple 2 component system [20]. At large enough particle concentrations and sufficient attraction between the particles, a network is formed; which can be considered as purely elastic, thus being characterized by a frequency independent plateau modulus, G'_p. The magnitude of G'_p increases as the particle concentration or the attraction between the particles increases. Interspersed throughout this elastic network is the suspending fluid, which has a purely viscous modulus, with $G''(\omega)$ increasing linearly with frequency. The magnitude of this contribution is independent of the particle concentration or the particle interaction. Thus at low frequencies $G'(\omega)$ dominates, while at high frequencies $G''(\omega)$ dominates. The cross-over occurs when the viscous and the elastic contributions are equal,

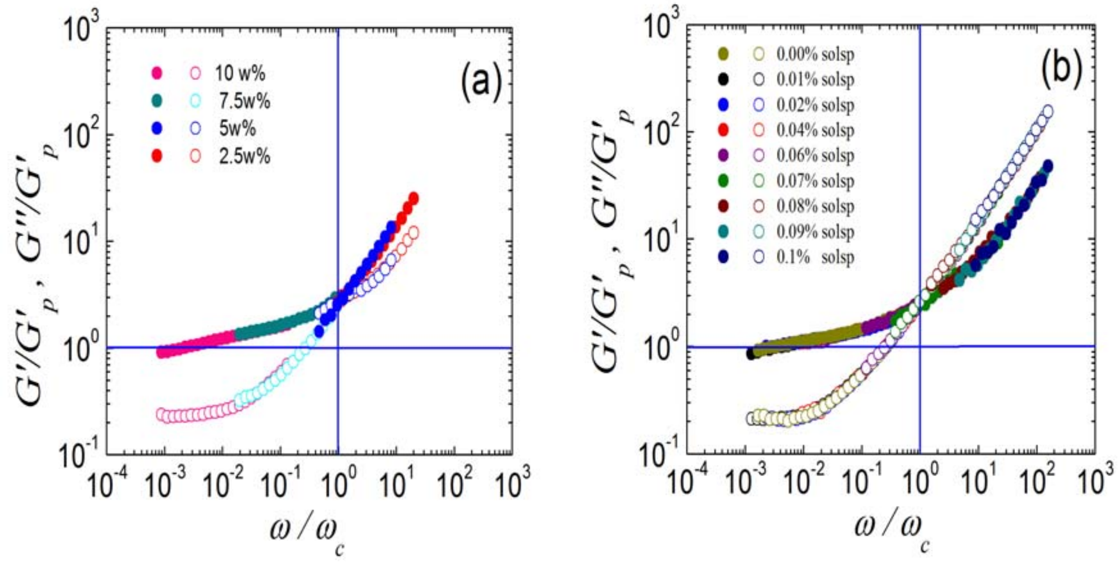

Figure III.12: Mechanical response function of ZnO gels scaled onto universal mastercurves for (a) different ZnO concentrations and (b) varying surfactant concentration. The storage modulus is denoted by closed symbols while the loss modulus is denoted by open symbols. The legend of respectively the volume fractions and solsperse concentrations used are given in the figure.

$$G'_p = G''(\omega_c) = \eta\omega_c \tag{III.3}$$

with η the viscosity of the medium. Within this picture the data of different systems will clearly exhibit scaling by a simple linear shift along the background viscosity. As shown in Figure III.13(a) and (b), this is indeed the case for the shift factors we used to scale all the data obtained for the various solid-like systems onto master-curves. Note, that the scaling technique used to obtain the master-curve in the mechanical response functions is strongly reminiscent of the one used to scale the MSDs. In both cases we use the characteristic cross-over time or respectively frequency to shift the *x*-axis; in both cases we use the plateau values (δ^2 and G'_p) found at long times or respectively small frequencies to shift the *y*-axis. Indeed, the physics determining the shift parameters of both master-curves is essentially the same. At short times the fluctuations of the network within the background fluid determines the spectrum, while at long times the constraints due to the solid nature of the network become determining. In particular Krall and Weitz

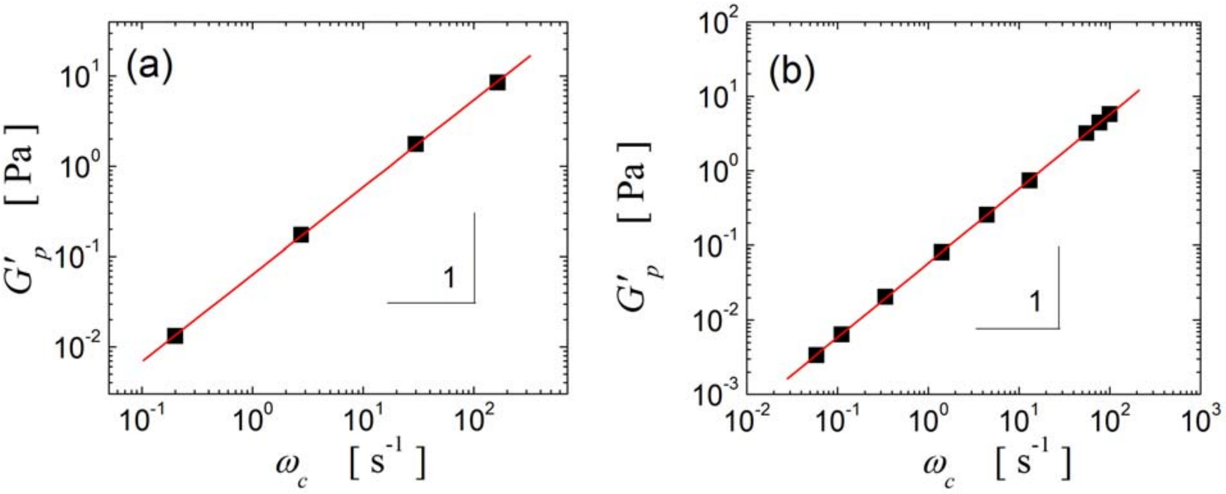

Figure III.13: Parametric plot of the scaling parameters used to scale the rheological response onto master-curves for the Solsperse-coated ZnO-particle gels at (a) different ZnO concentrations and (b) varying dispersant concentration.

[16] denoted that the elastic modulus can be directly determined from the characteristic time of the floppiest mode $\tau_c = 6\pi\eta\, R_c / \kappa_c$ as

$$G'_p = \kappa_c / R_c = 6\pi\eta / \tau_c \qquad \text{(III.4)}$$

We evaluate the validity of this relation using the data obtained for the Solsperse-coated ZnO-particle system, reporting G'_p and $6\pi\eta/\tau_c$ as a function of respectively the ZnO-concentration and the inverse of the Solsperse concentration in Figure III.14(a) and (b). The agreement between G'_p and $6\pi\eta/\tau_c$ is remarkably good, indicating that we can indeed evaluate the magnitude of the plateau modulus by using the time at the onset to constraint dynamics as an absolute measure for elasticity.

The dependence of the plateau modulus on dispersant concentration suggests a critical-like onset of solid-like behavior, which can be described by

$$G'_p = A\left(\frac{1}{[Disp.]} - \frac{1}{[Disp.]_c}\right)^{\alpha} \qquad \text{(III.5)}$$

with $A = 0.5$, $[Disp.]_c = 0.12\text{w\%}$ and $\alpha = 0.6$, as shown by the solid line in Figure III.14(b). This critical behavior is a hallmark of weakly interacting colloidal systems [21] and indicates that the elastic behaviour changes dramatically around the critical dispersant concentration, $[Disp.]_c$. For the dependence of the plateau modulus on particle

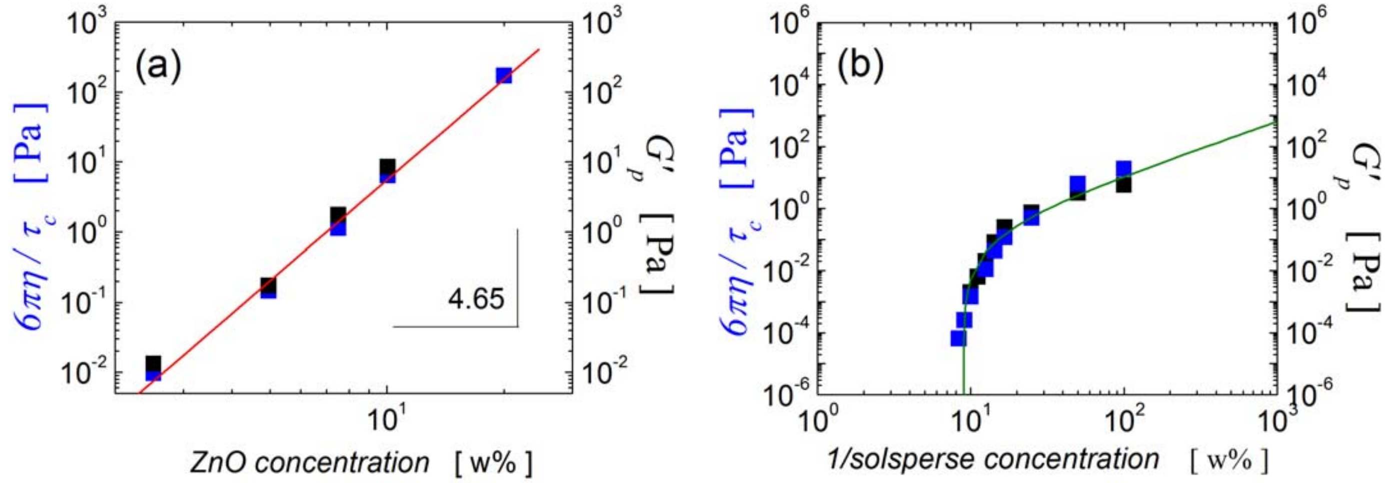

Figure III.14: Elastic modulus from rheology (black squares) and DWS using the Krall-Weitz model (blue squares) as a function of (a) varying ZnO concentration and of (b) varying dispersant concentration.

concentration shown in Figure III.14(a), we attribute not finding a critical onset of the solid-like behaviour for this data-set to the lack of data at lower concentrations rather than to the absence of such an onset. At any rate, it is apparent that the rheological behaviour of these suspensions can be tuned either by a variation of the particle concentration or by a change of the particle-particle interaction.

The fact that the dynamics at the very small length scale probed by DWS is reflecting the macroscopic properties of our systems implies that the origin of elasticity can be related to the microscopic particle-particle spring constant, κ_0, as this is the case for strongly aggregated systems. The elastic modulus of fractal networks is related to the volume fraction and the particle-particle spring constant as [22]:

$$G'_p = \frac{\kappa_0}{a}\Phi^{\nu} \qquad \text{(III.6)}$$

where $\nu=(3+d_b)/(3-d_f)$. Experiments on fractal gels composed of latex spheres yielded $\nu = 3.5 \pm 0.3$ [13, 14, 16, 19], which agrees with the theoretical prediction of ν =3.73 using d_f=1.9 and d_b=1.1 as expected for Diffusion Limited Cluster Aggregation (DLCA). By contrast, we find ν = 4.65 for the Solsperse-coated ZnO-particle system, which is within the range of that expected for elasticity percolation [23, 24]. Using the relation III.6 to determine the elastic modulus for the Pluronic- and PNiPAM-coated PS-particle

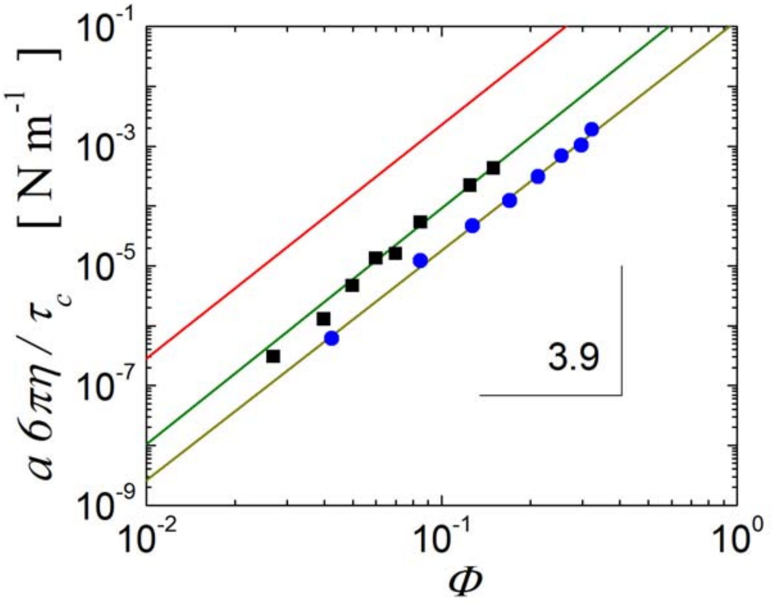

Figure III.15: Volume fraction dependence of the elastic modulus as calculated using the Krall-Weitz model. Black squares denote the data obtained for the Pluronic-coated PS-particle gels, blue circles denote the data obtained for the PNiPAM coated PS-particle gels and the red line denotes the behaviour of the bare PS-particle gels as reported in reference [16]. The green and yellow lines respectively correspond to power law fits to the data.

system, we find respectively $\nu = 3.97$ and $\nu = 3.90$, which is comparable to the power law found for strongly aggregated uncoated PS-particle systems. For the uncoated PS-particle system it could be shown that the effect of the particle size could be fully accounted for by multiplying G'_p with a [14, 19], which indicates that κ_0 is independent of the particle size. Thus, for comparison we report $a \cdot 6\pi\eta/\tau_c$ as a function of volume fraction in Figure III.15, where we show in addition to the data obtained for the Pluronic- and PNiPAM-coated systems the power law behaviour of the uncoated PS-system, that we obtained using the literature data [16]. For a given volume fraction we find that the magnitude of $a \cdot 6\pi\eta/\tau_c$ is decreasing in the order of uncoated PS > Pluronic-coated PS > PNiPAM-coated PS. We can quantify this decrease by determining κ_0 according to equation III.6. For the gels composed of uncoated PS-particles $\kappa_0 \sim 18.7$ Nm^{-1} [14, 19], for the gels composed of the Pluronic- and PNiPAM-coated PS-particles respectively $\kappa_0 \sim 1.0$ Nm^{-1} and $\kappa_0 \sim 0.1$ Nm^{-1}. Clearly, the coating weakens the particle spring constant, i.e. the attractive interactions between PS-particles. However, this weakening does not lead to a significant change in the volume fraction dependence of the dynamics and elasticity of the systems. In particular we find no indication that the elastic modulus exhibits a critical-like onset, as this was found for other weakly interacting systems [21, 25, 26]. However, we note that our investigations are restricted to fairly high volume fractions, such that we can not exclude the existence of a critical volume fraction at low Φ.

Summary.

We have developed and investigated three colloidal particle systems in which the particle interactions are partially controlled by steric stabilization; two of the systems are spherical colloidal model systems and one is an industrial product, with ill defined shape and high polydispersity. Despite these differences we find that the dynamics and rheology of gels formed by these particle-systems can be described by simple models [16, 20] that essentially assume a dominant contribution of the background viscosity at short times and a dominant contribution of the elasticity of the network at long times. This simple behavior allows us to scale all dynamical and rheological data of a given system onto master-curves, which allows us to determine characteristic parameters with a high relative accuracy. Analyzing the interrelation of these parameters, we find that the characteristic length of a given system is seemingly entirely set by the particle volume fraction and is not affected by the particle-particle interactions.

References.

1. W. B. Russel, W. R. Schowalter, and D.A. Saville, *Colloidal Dispersions*. 1989: Cambridge University Press.
2. T. Sato and R. Ruch, *Stabilization of Colloidal Dispersions by Polymer Adsroption*. 1980, New York: Marcel Dekker.

3. Donald H. Napper, *Polymeric Stabilization of Colloidal Dispersions*, ed. A. Press. 1983, London.
4. J.B. Kayes and D.A. Rawlins, *Adsorption Characteristics of Certain Polyoxyethylene-Polyoxypropylene Block co-Polymers on Polystyrene Latex.* Colloid Science, 1979. **257**: p. 622-629.
5. James A. Baker and J.C. Berg, *Investigation of the Adsorption Configuration of Poly(ethylene oxide) and Its Copolymers with Poly(propylene oxide) on Model Polystyrene Latex Dispersions.* Langmuir, 1988. **4**: p. 1055-1061.
6. S. Alexander, *Adsorption of Chain Molecules with a Polar Head. A Scaling Description.* Le Journal de Physique, 1977. **38**: p. 983-987.
7. H.M. Wyss, et al., *Diffusing-Wave Spectroscopy of concentrated Alumina Suspensions During Gelation.* Journal of Colloid and Interface Science, 2001. **241**: p. 89-97.
8. H.M. Wyss, et al., *Small Angle Static Light Scattering of Concentrated Silica Suspensions During in Situ Destabilization.* Journal of Colloid and Interface Science, 2004. **271**: p. 388-399.
9. H. M. Wyss, *Microsctructure and Mechanical Behavior of Concentrated Particle Gels*. 2003, Swiss Federal Institute of Technology Zurich.
10. N. Dingenouts, Ch. Norhausen, and M. Ballauff, *Observation of the Volume Transition in Thermosensitive Core-Shell latex Particles by Small-Angle X-ray Scattering.* Macromolecules, 1998. **31**: p. 8912-8917.
11. E. D. Daly and B R. Saunders, *A Study of the Effect of Electrolyte on the Swelling and Stability of Poly(N-isopropylacrylamide) Microgel dispersions.* Langmuir, 2000. **16**: p. 5546-5552.
12. D.A. Weitz and D. J. Pine, *Dynamic Light Scattering*, ed. C.P. Oxford. 1993.
13. S. Romer, *Aggregation and Gelation of Concentrated Colloidal Suspensions*. 2001, Swiss Federal Institute of Technology Zurich: Zurich.
14. H. Bissig, *Dynamics of Two Evolving Systems: Coarsering Foam and Attractive Colloidal Particles*. 2004, University of Fribourg: Fribourg.
15. M. Carpineti, et al., *Salt-induced Fast Aggregation of Polystyrene Latex.* Physical Review A, 1990. **42**(12): p. 7347-7354.

16. A.H. Krall and D.A. Weitz, *Internal Dynamics and Elasticity of Fractal Colloidal Gels.* Physical Review Letters, 1998. **80**(4): p. 778-781.

17. A. D. Dinsmore and D. A. Weitz, *Direct imaging of three-dimensional structure and topology of colloidal gels.* Journal of Physics: Condensed Matter, 2002. **14**: p. 7581-7597.

18. P. Meakin, et al., *Topological properties of diffusion limited aggregation and cluster-cluster aggregation.* Journal of Physics A, 1984. **17**: p. L975-L981.

19. T. Gisler, R.C. Ball, and D.A. Weitz, *Strain Hardering of Fractal Colloidal Gels.* Physical Review Letters, 1999. **82**(5): p. 1064-1067.

20. V. Trappe and D. Weitz, *Scaling of the Viscoelasticity of Weakly Attractive Particles.* Physical Review Letters, 2000: p. 449-452.

21. V. Prasad, et al., *Universal Features of the Fluid to Solid Transition for Attractive Colloidal Particles.* Faraday Discussions, 2003. **123**: p. 1-12.

22. Y. Kantor and I. Webman, *Elastic Properties of Random Percolating Systems.* Physical Review Letters, 1984. **52**(1891-1894).

23. Shechao Feng, et al., *Percolation on two-dimensional elastic networks with rotationally invariant bond-bending forces.* Physical Review B, 1984. **30**(9): p. 5386-5389.

24. T. A. Witten and L. M. Sander, *Diffusion-Limited Aggregation, a Kinetic Critical Phenomena.* Physical Review Letters, 1981. **47**(19): p. 1400-1403.

25. V. Trappe, et al., *Jamming Phase Diagram for Attractive Particles.* Nature, 2001. **411**: p. 772-775.

26. M. C. Grant and W. B. Russel, *Volume-Fraction Dependence of Elastic-Moduli and Transition-Temperatures for Colloidal Silica-Gels.* Physical Review E, 1993. **47**(4): p. 2606-2614.

Chapter IV.

Non-evolutionary Slow Dynamics in Weakly Aggregated Colloidal Particle Systems.

Introduction.

Colloidal gels are generally considered to belong to the class of non-equilibrium solids, which are characterized by mechanical stability and arrested dynamics. However, because of their non-equilibrium nature such solids are often found to exhibit some residual slow structural relaxation that evolves with the age of the sample. Indeed, previous studies on strongly aggregated particle gels revealed that gels can exhibit strong aging behavior [1-3], which has been attributed to quenched-in internal stresses that are gradually released by breaking bonds [4].

In this chapter we compare the aging behavior of a strongly aggregated system to the evolution of the long time dynamics of a more weakly aggregated system, namely we compare the behavior of an aggregated uncoated (bare) polystyrene system to the one of the PNiPAM coated polystyrene system described in Chapter III. The particle-particle spring constant of the PNiPAM-coated PS-system is with $\kappa_0 = 0.13 \mathrm{N \cdot m^{-1}}$ significantly smaller than the one of a uncoated PS-system where $\kappa_0 = 18.72\ \mathrm{N \cdot m^{-1}}$ [5]; this ensures that we indeed compare two systems that differ in their particle-particle interactions. In the previous chapter we show that this difference does not significantly change the dependence of the short time dynamics on the particle volume fraction and indicates that the structures formed by both systems are similar, which for a given volume fraction exhibit the same correlation length.

Experimental Systems and Methods.

To evaluate the differences in the evolutionary behavior of weakly and strongly aggregating system we perform time resolved experiments on both PNIPAM-coated polystyrene particles and standard charge stabilized polystyrene particles of similar size. For the comparative study we choose to perform our experiments at a particle volume fraction of $\Phi = 0.13$. Additionally we investigate the slow dynamics of the PNIPAM-coated polystyrene particles at different volume fractions ranging from Φ=0.04 to Φ= 0.3. The preparation, characteristics and destabilization procedures of the PNiPAM coated PS-particles (radius a = 181nm) are described in Chapter III. Our charge stabilized PS-particles are sulfated particles from IDC with a surface charge density of σ = $0.6 \cdot 10^{-2}$ C/m^2 and a radius of a = 150nm. We destabilize this particle system by using the *in situ* destabilization method described in the previous chapter. The start of the experiments at t = 0s is respectively defined as the moment when the temperature is set to increase from 20°C to 40°C in the case of PNiPAM coated PS-particle system and as the moment of mixing the urease solution into the suspension in the case of the bare PS-particle system. The temporal evolution of the temperature in the experiment with the PNIPAM-coated PS-particles is shown in Figure IV.1(a) and the temporal evolution of the ionic strength in the experiment with the bare PS-particles is shown in Figure IV.1(b). The total length of the experiments is 24h.

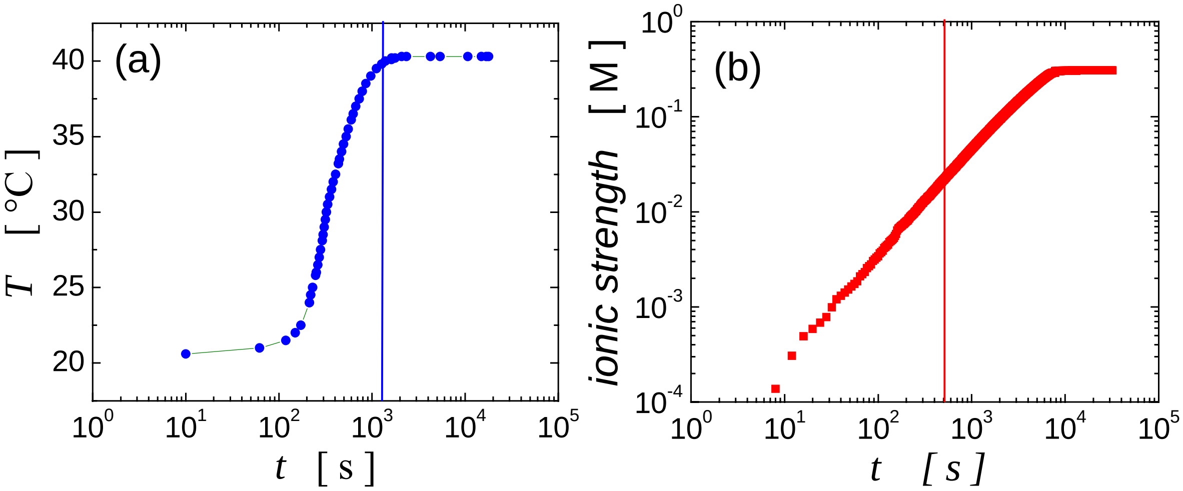

Figure IV.1: Temporal evolution of (a) the temperature in the experiment with the PNiPAM-coated PS-particles and (b) the ionic strength in the experiment with the bare PS-particles. The ionic strength is extracted from conductivity measurements as described in chapter III. The vertical lines corresponds to the moment, at which our systems start to exhibit constraint dynamics at intermediate lag-times.

We monitor the evolution of the fast and slow dynamics of our systems by performing DWS-experiments in the transmission geometry using both the single speckle and multi speckle detection schemes described in Chapter II. The fast dynamics is continuously recorded by acquiring correlation functions averaged for 180s in the beginning of the experiments, the averaging time being gradually increased up to 900s during the coarse of our experiment. For the PNiPAM coated PS-particle system, the slow dynamics is recorded in short TRC experiments of 250s, while we monitor the temporal evolution of the slow dynamics of the bare PS-particle system by recording the TRC-data continuously during the entire course of our experiment. The long time correlation functions at various ages of our samples are obtained by calculating the time average over the entire 250s experiments in the case of the PNiPAM-coated particle system; for the bare PS-particle system we choose to take time averages over 900s. For both systems we use scattering cells with an optical path length of $L = 1\text{mm}$, which ensures that for all systems $L/l^* > 10$, the transport mean free path being $l^* = 22\mu\text{m}$ for the bare PS-system at $\Phi = 0.13$, and $l^* = 53 - 16\mu\text{m}$ for the PNiPAM-coated PS-system in the investigated Φ-range of 0.04-0.3.

Results and Discussion.

Correlation functions obtained at different moments after initialization of the aggregation process are shown for the PNiPAM-coated PS-system in Figure IV.2(a) and for the bare PS-system in Figure IV.2(b). In both cases the volume fraction is $\Phi = 0.13$. The short time dynamics of both systems exhibits a similar development. The fast relaxation process becomes slower and the magnitude of the plateau noted at intermediate lag-times gradually increases in time. By contrast, we find distinct differences in the evolution of the long-time dynamics of the two systems investigated. The bare particle system exhibits a typical evolutionary behavior with a long-time relaxation process that becomes slower and slower with increasing age of the sample, while the coated particle system exhibits a nearly stationary long-time relaxation process. We quantify both processes the short-time and long-time process separately.

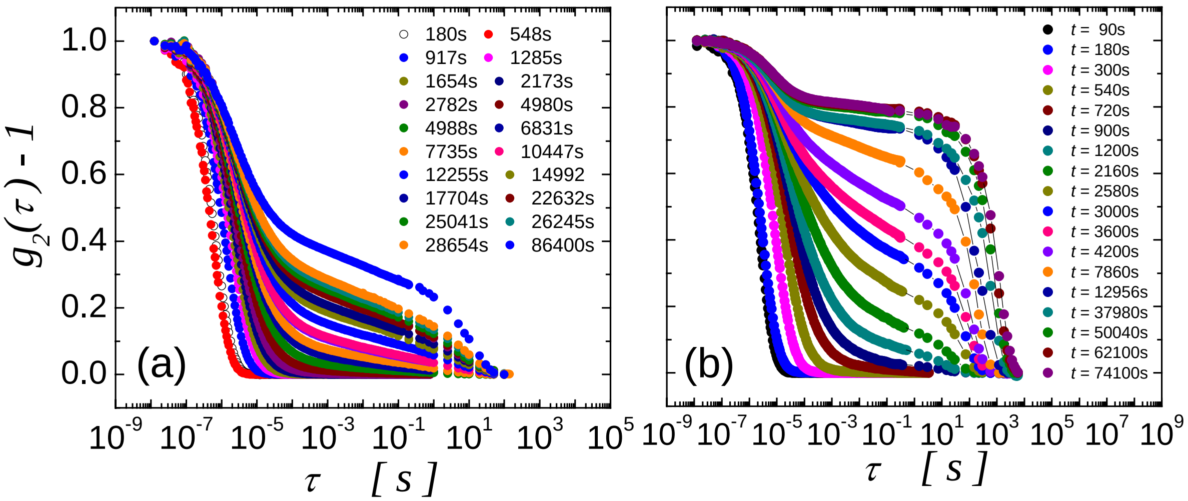

Figure IV.2: Correlation functions obtained at different moments after start of the experiment for (a) the PNiPAM coated PS-particle system and (b) the bare PS-particle system. The volume fraction is in both cases Φ=0.13.

For the short time process we convert the correlation function into mean squared displacement (MSD) and determine the crossover time, τ_c, and the characteristic mean squared displacement, δ^2, using the scaling procedure described in Chapter III. Both parameters reflect the elastic properties of our system, which emerge as the system undergoes a sol-gel transition. Thus, we define the gelation time t_0 as the time at which we detect for the first time a measurable τ_c and δ^2, which we indicate as vertical lines in Figure IV.1(a) and (b). In Figure IV.3(a) and (b) we report the evolution of τ_c and δ^2 as a function of the age of the gel given by t-t_0. Owing to the weaker particle-particle interactions between the PNiPAM-coated particles τ_c and δ^2 are systematically larger for this particle system than for the bare PS particle-system. For both systems we find that τ_c and δ^2 initially decrease in time at a similar rate, which indicates a gradual stiffening of the gels beyond the gel-point. At later stages this stiffening process appears to slow down for the bare particle system, while δ^2 and τ_c continuously decrease over the entire duration of the experiment in the case of the PNiPAM-coated particle-system.

For the long-time process we approximate the correlation function by a stretched exponential function, $g_2(\tau)-1 \sim exp(-(\tau/\tau_S)^p)$. To optimize our fit we use $\log[-\ln(g_2-1)]$

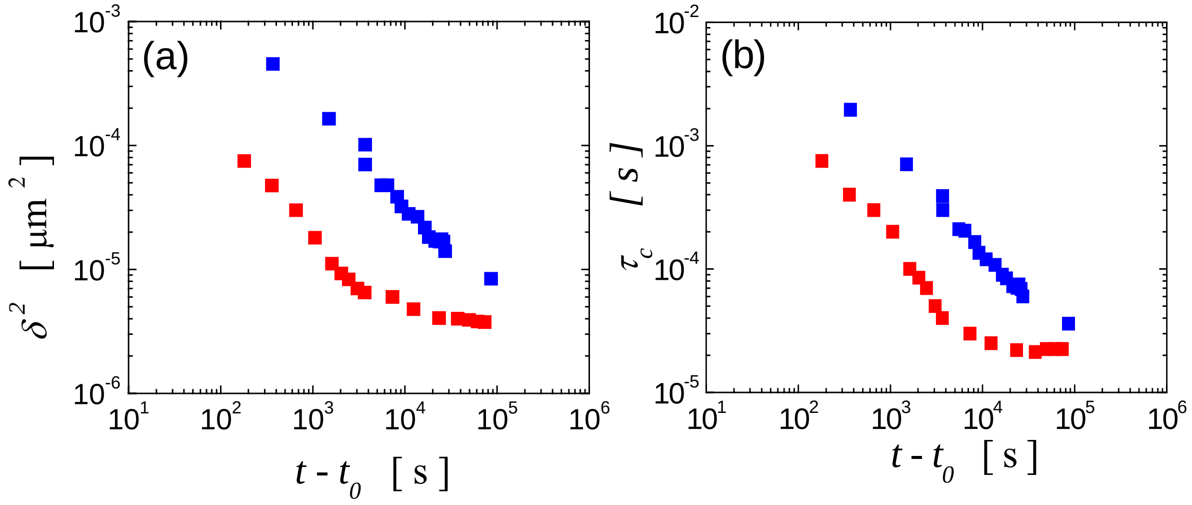

Figure IV.3: (a) Plateau mean squared displacement δ^2 and (b) characteristic cross-over time τ_c as a function of the age of the gel. The blue and red symbols correspond respectively to the data obtained for the PNiPAM coated PS-particle system and the bare PS-particle system.

and $\log[\tau]$ as y and x parameters respectively and apply a linear regression scheme to obtain p and τ_S. For the two systems at $\Phi = 0.13$ we find that p exhibits only little variation in time; however, the magnitude of p displays distinct differences between the two systems; while $p \sim 1$ for the bare particle system, $p \sim 0.5$ for the PNiPAM-coated particle system. This indicates that the structural relaxation spectrum of the PNiPAM-coated particle system is at this volume fraction significantly broader than the one of the bare particle system. More importantly our analysis confirms that the evolutionary behavior of the structural relaxation τ_S of the two systems exhibits marked differences. As observed previously for a similar system [2], we find in the case of the bare particle system that τ_S increases with the age of the gel following a power-law $\tau_s \sim (t - t_0)^{1.3}$, as shown in Figure IV.4. By contrast, τ_S remains nearly constant over the entire length of our experiment in the case of the PNiPAM coated particle system.

These remarkable differences in the temporal evolution of the structural relaxation process of the two systems investigated are somewhat difficult to understand. Considering the evolution of the fast dynamics we find essentially no differences in the aggregation kinetics of the two systems. Indeed, considering only the fast dynamics we would state that the two gels differ only in their particle-particle spring constant, but not

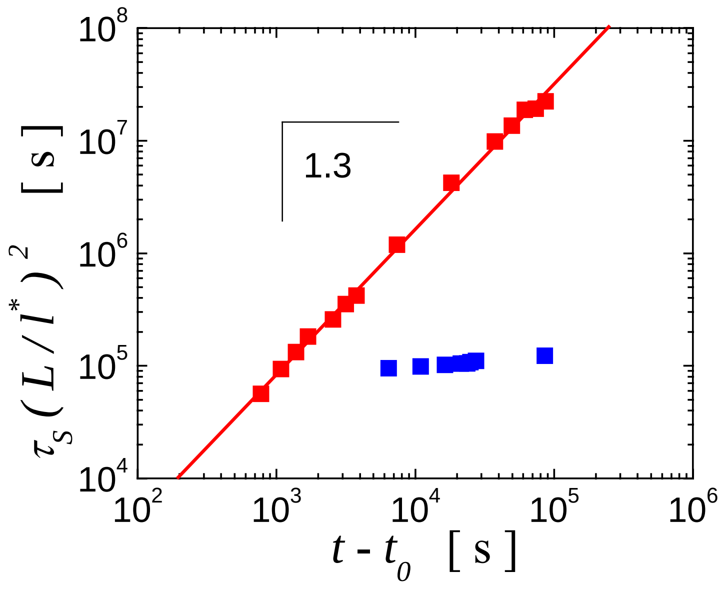

Figure IV.4: Characteristic structural relaxation time as a function of the age of the gel for the PNiPAM coated PS-particle system (blue symbols) and for the bare PS-particle system (red symbols). The bare PS-particle system exhibits a power law behavior with an exponent of 1.3. By contrast, the PNiPAM coated PS-particle system exhibits an almost stationary behavior.

in their gel-structure [see Chapter III]. Considering that the argument of quenched-in internal stresses drive the structural relaxation process applies, we would have hypothesize that the gel-structure sets the level of internal stresses and thus determines the structural relaxation process. Consequently, we would have expected that both systems exhibit a similar age dependence of their slow dynamics, which is evidently not the case.

To gain further insight in the structural relaxation process of our PNiPAM-coated PS-system, we explore its dependence on volume fraction. In Figure IV.5 we show the correlation functions obtained $t = 8$h for different volume fractions. As described in detail in the previous chapter increasing Φ leads to an increase in the intermediate plateau and consequently to a shift of the cross-over time τ_c to shorter lag times. For the slow relaxation process we find that an increase of Φ leads to a considerable increase of the structural relaxation time. As done for the analysis of the long time behavior of the samples at $\Phi = 0.13$ we fit the long-time behavior with a stretched exponential function

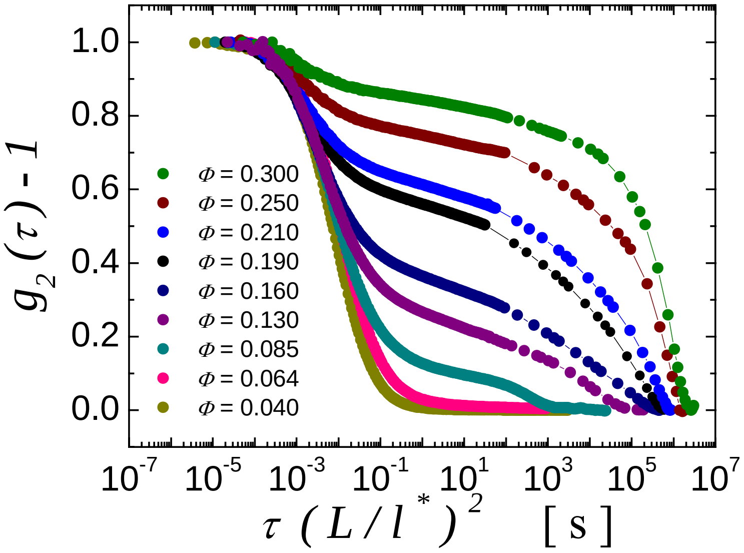

Figure IV.5: Correlation functions of PNiPAM coated PS-particle gels at t = 8h for Φ = 0.3 (green), Φ = 0.25 (brown), Φ = 0.21 (blue), Φ = 0.19 (black), Φ = 0.16 (dark blue), Φ = 0.13 (purple), Φ = 0.085 (cyan), Φ = 0.064 (pink) and Φ = 0.04 (yellow).

to determine τ_s and p. We find that the magnitude of τ_s dramatically increases in the volume range of Φ = 0.085-0.19 and then remains approximately constant between Φ = 0.19 and Φ = 0.30, as shown Figure IV.6(a). Interestingly, we find that the stretched exponent exhibits a dependence on Φ as well. As shown in Figure IV.6(b), p increases with Φ, the long-time relaxation exhibiting a nearly single exponential behavior at Φ =0.3 (p =0.94). Both parameters τ_s and p exhibit none or only little dependence on the age of the gel, as shown in Figure IV.7(a) and (b).

In summary, we find that the slow relaxation process of PNIPAM-coated PS-systems exhibits a stationary behavior, which is in strong contrast to the evolutionary slow dynamics found for bare PS-systems. In principle we could conceive that the interactions in our PNiPAM-coated system are weak enough to only allow for bonds with a finite life-time, which consequently would lead to a structural relaxation at a well defined rate. However, such process should in principle allow for considerable coarsening, which in turn should lead to a development of the fast dynamics in time that would be sensitively different to the one of the strongly aggregated PS-system, for which

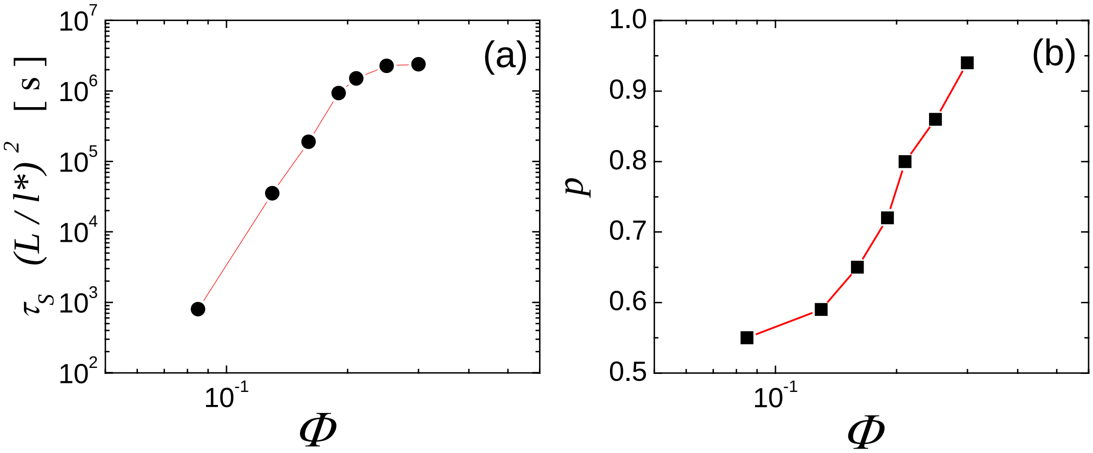

Figure IV.6: Volume fraction dependence of (a) the structural relaxation time and (b) stretched exponent of PNiPAM coated particle gels at t =8h.

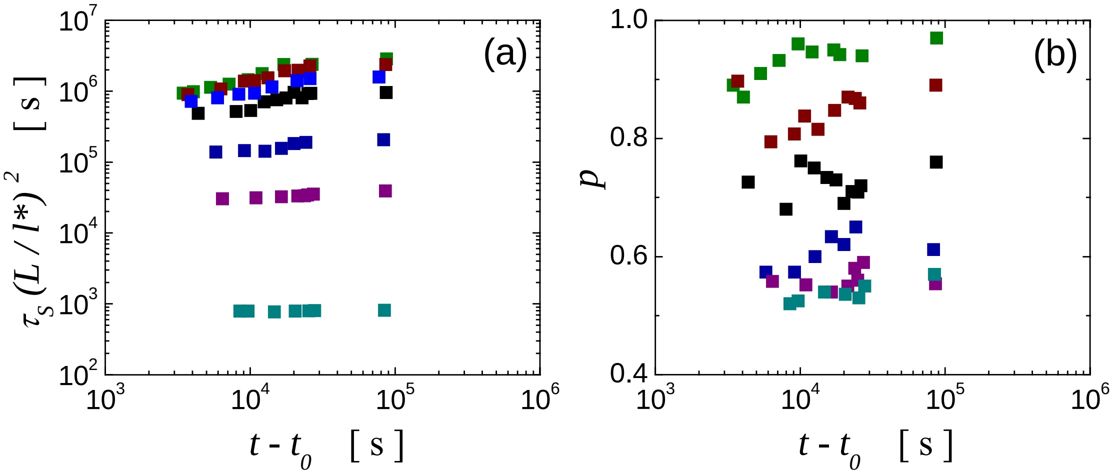

Figure IV.7: (a) Characteristic structural relaxation time and (b) stretched exponent as a function of the age of the PNiPAM coated PS-particle gels for $\Phi = 0.3$ (green), $\Phi = 0.25$ (brown), $\Phi = 0.21$ (blue), $\Phi = 0.19$ (black), $\Phi = 0.16$ (dark blue), $\Phi = 0.13$ (purple) and $\Phi = 0.085$ (cyan).

the long time dynamics is evolutionary. This, however, is not the case, at least not for $t\text{-}t_0 < 3000$s. Further investigations will be needed to fully elucidate the origin of the differences found in the development of the long-time process of the bare PS-system and the PNiPAM-coated systems. At the present state of research, we can only point out that marked changes in the volume fraction dependence of dynamic properties at volume fractions at about 10% have been repeatedly observed [1, 6]. For large enough particle-particle interactions this volume fraction appears to correspond to the limit between the low density gels that are typically fractal gels and the high density gels that fill space more homogeneously. This limit appears to also determine the change in the development of the long-time relaxation with volume fraction observed at $\Phi \sim 0.2$ and will need to be accounted for in any model describing the long-time dynamics of our PNiPAM-coated particle system. As a final remark, we point out that correlation functions measured in the multiple scattering limit are sensitive to the motion of single scatterers. This is because the photons effectively explore several scattering sites. Thus, for a full dephasing of the contribution of a given path it is sufficient that one of the scattering sites along that path moves by more than a wavelength. This is in strong contrast to single scattering experiments, in which each scattered photon corresponds to one scattering site, such that in average all particles have to move to lead to a full decorrelation. A full decay in the auto correlation function obtained by DWS could thus also be due to a population of mobile particles that effectively dephase all light paths even if another fraction of the particles is locally trapped in space. As it becomes increasingly recognized colloidal gelation can also occur by an arrested phase separation, where the particles become dynamically arrested within the denser phase [7, 8]. In such case we could conceive that the particles, which in the lower density phase are still free to diffuse around, will eventually lead to a full dephasing of the multiply scattered light. Whether this is the case for the PNiPAM-coated particle system is a matter of further investigations.

References.

1. H. Bissig, et al., *Intermittent Dynamics and hyper-aging in dense colloidal gels.* PhysChemComm, 2003. **6**(5): p. 21-23.

2. H. Bissig, *Dynamics of two evolving systems: coarsering foam and attractive colloidal particles*. 2004, University of Fribourg: Fribourg.

3. L. Cipeletti, et al., *Universal Aging Features in the Restructuring of Fractal Colloidal Gels.* Physical Review Letters, 2000. **84**(10): p. 2275-2278.

4. L. Cipeletti and L. Ramos, *Slow dynamics in glassy soft matter*. Journal of Physics: Condensed Matter, 2005. **17**: p. R253-R285.
5. T. Gisler, R.C. Ball, and D.A. Weitz, *Strain Hardering of Fractal Colloidal Gels.* Physical Review Letters, 1999. **82**(5): p. 1064-1067.
6. S. Romer, *Aggregation and Gelation of Concentrated Colloidal Suspensions*. 2001, Swiss Federal Institute of Technology Zurich: Zurich.
7. N. A. M. Verhaeg, et al., *Transient gelation by spinodal decomposition in colloid-polymer mixtures.* Physica A, 1997. **242**(1-2): p. 104-118.
8. S. Manley, et al., *Glasslike Arrest in Spinodal Decomposition as a Route to Colloidal Gelation.* Physical Review Letters, 2005. **95**: p. 238302-1 238302-4.

Chapter V.

Phase Behavior of Poly(N-isopropyl-acrylamide) Microgels.

Introduction.

In recent years, a new class of colloidal-type systems has been investigated where the volume fraction and the inter-particle interactions of a given solution can be tuned by temperature [1]; one of the most prominent example of this class of colloids being the poly-N-isopropylacrylamide (PNIPAM)-microgels. These microgels are cross-linked PNiPAM-particles that are soluble in water at temperatures below the lower critical solution temperature (LCST) of PNiPAM at ~ 33°C. In the fully swollen state at low temperatures their behavior varies from more polymer-like to more colloid-like behavior depending on the cross-linking density [2]. As the temperature increases the size of the PNiPAM-microgels decreases continuously up to the LCST; beyond the LCST the microgels collapse forming now more colloidal-type systems, which aggregate if not otherwise stabilized [3-5]. Thus, these systems allow for the study of both repulsive and attractive colloidal phases, the switch between the two being conveniently controlled by temperature [6].

In this study we explore both the behavior of the repulsive phases below the LCST and the one of the attractive phases above the LCST. For our investigations of the repulsive phases we use small angle neutron scattering and steady shear rheology, for the investigations of the attractive phases we use microscopy, static light scattering and diffusing-wave spectroscopy.

Experimental Systems: Synthesis and Characterization.

Materials.

N-isopropylacrylamide (NiPAM; Aldrich), *N*,*N'*-methylenbisacrylamide (BIS; Fluka) Sodium dodecylsulfate (SDS; Merck) and potassium peroxodisulfate (KPS; Merck) are used as received. Deionized water (Millipore) is used.

Emulsion polymerization.

The PNiPAM-microgels are prepared in an emulsion polymerization as described in [7]. We use a 2 L, three-necked flask equipped with a stirrer, a reflux condensor, and a gas inlet. NiPAM (7.87 g), the crosslinker BIS (0.15 g), and the stabilizer SDS (0.15 g) are dissolved in 450 ml pure water under stirring. The initiator KPS (0.3 g) is dissolved in 50 ml water. Both solutions are bubbled with nitrogen for 30 min. After heating the mixture to 70°C the initiator solution is added. After 6 h the dispersion is cooled to room temperature and subsequently purified by extensive dialysis against water. Finally, we freeze dry the solution to obtain the microgels in powder form.

Characterization.

We characterize the temperature dependent conformational properties of our microgels at a concentration of $4 \cdot 10^{-4}$g/ml in three different solvents, H_2O, D_2O and a 0.3 molar solution of NaSCN in D_2O, by using static and dynamic light scattering to determine respectively the radius of gyration, R_G, and the hydrodynamic radius, R_H, in a temperature range of 20-40ºC. For the three solvents we obtain qualitatively the same behavior, as shown in Figure V.1. Increasing the temperature leads to a gradual decrease of the particle size up to the lower critical solution temperature T_c, which we characterize by fitting the temperature dependence of R_H for $T < T_c$ to a critical-like function of form

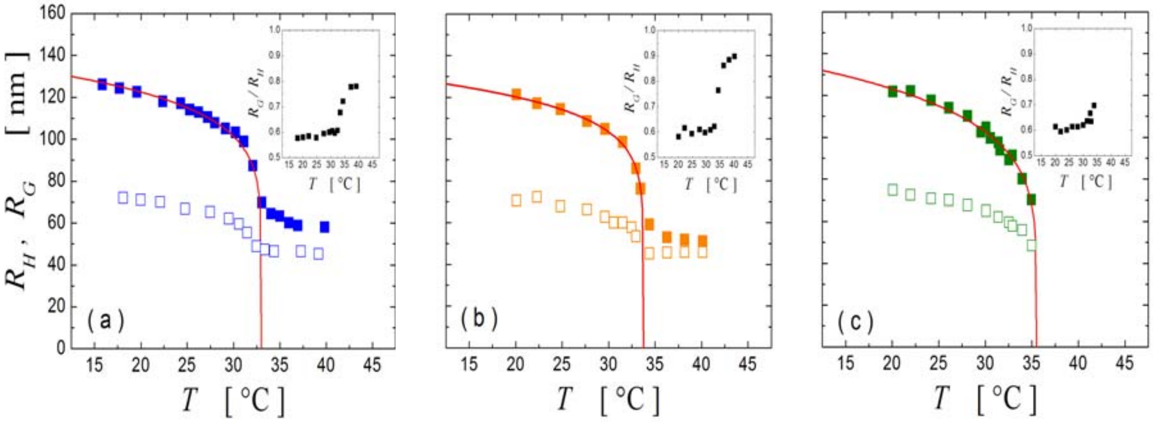

Figure V.1: Temperature dependence of microgel dimensions in (a) H_2O, (b) D_2O and (c) 0.3 molar solution of NaSCN in D_2O. Closed symbols denote hydrodynamic radii, R_H, and open symbols the radii of gyration, R_G. Red lines correspond to the fits of the data to $R_H=A(T_c-T)^{\alpha}$. Insets display the evolution of the ratio R_G/R_H with temparture.

$R_H = A\,(T_c - T)^{\alpha}$; the fits are shown as red lines in Figure V.1 and the resulting fit parameters are given in Table V.1. We find that T_c is somewhat sensitive to the solvent conditions used, where the most significant shift is observed for the 0.3 molar solution of NaSCN in D_2O. This finding is in agreement with previous studies investigating the effect of added electrolyte on the dimensions of PNiPAM microgels, where an increase in the particle size at ionic strength above 0.1M NaSCN was denoted [8]. This effect can be understood as being due to an improvement of the hydration of PNiPAM by the addition of thiocyonat (SCN^-). Indeed, thiocyonat belongs to the class of so-called 'structure making' ions that improves the hydration of uncharged water soluble polymers as classified in the Hofmeister series [9].

Solvent	T_c [ºC]	α	A [nm]
H_2O	33.0	0.129	88
D_2O	33.7	0.115	89
D_2O 0.3M NaSCN	35.5	0.176	76

Table V.1: Fit parameters obtained by fitting the temperature dependence of R_H to a critical-like function of form $R_H = A\,(T_c - T)^{\alpha}$.

Increasing the temperature beyond T_c leads to a complete collapse of the microgels and in the case of the 0.3 molar solution of NaSCN in D_2O to aggregation, which precludes the size determination of the microgels at these conditions. Indeed, T_c being the critical temperature beyond which PNiPAM preferentially interacts with itself, we would generally expect aggregation of the microgel particles for $T > T_c$. That this is not the case without addition of electrolyte is due to the fact that our microgels are charged because of the use of an ionic initiator; this charge when unscreened provides stability to the system at high temperature.

Interestingly, we find distinct differences in the temperature dependence of R_G and R_H, which becomes most evident by plotting the ratio R_G / R_H versus temperature, as shown in the inset of Figure V.1. For $T << T_c$ we find $R_G / R_H \sim 0.6$, which is unusually low as compared to values typically found for hard sphere colloids ($R_G / R_H \sim 0.8$) and for polymers in solution ($R_G / R_H \sim 1.5$) [7]. This relatively low value of R_G / R_H can be attributed to an uneven distribution of cross-linker, the cross-linking density being larger in the center of the particle than on the edges [7]. Because of the higher density of PNIPAM within the core, the core scatters significantly more than the low-density shell, such that we depict the radius of the cross-linked core in static light scattering, while we depict the hydrodynamically effective radius of the particle in dynamic light scattering. Note, that we would expect the effective size of the entire particle to be larger than R_H as the lower density edges will allow for some free drainage, as this is the case for polymers in solution. The non-proportional variation in R_G and R_H as the temperature increases can be attributed to a more significant shrinkage of the shell than of the core; alternatively it could be the result of the portion of the shell being near the high density core now becoming sufficiently dense to become part of the highly scattering core, such that the core appears to shrink less than the hydrodynamic relevant volume. Eventually the density of the overall particle seems to equilibrate at $T > T_c$, as we recover $R_G / R_H \sim 0.8$ which is the value expected for hard spheres.

In the following we restrict our studies on the phase behavior of PNiPAM microgels dissolved in 0.3 molar solutions of NaSCN in D_2O; this enables us to span a broad range of interaction potentials and allows for investigations by neutron scattering. We study both the repulsive behavior of these systems at $T < T_c$ and the attractive behavior at $T > T_c$ as a function of volume fraction and temperature. For $T < T_c$ we use the sizes determined at the given condition and shown in Figure V.1(c), for $T > T_c$ we infer the sizes obtained in D_20 and shown Figure V.1(b) as we could not determine the sizes in 0.3 molar solutions of NaSCN in D_2O because of aggregation.

Results and Discussion.

Properties of PNiPAM microgels below the LCST.

We study the structural and dynamical properties of PNiPAM-microgel solutions below the LCST by means of small angle neutron scattering (SANS) and rheology exploring a wide range of concentration. The SANS-experiments are performed at the Paul Scherrer Institute in collaboration with Dr. Joachim Kohlbrecher. The samples investigated are listed in Table V.2 and the experiments are performed at $T = 20.8$°C and

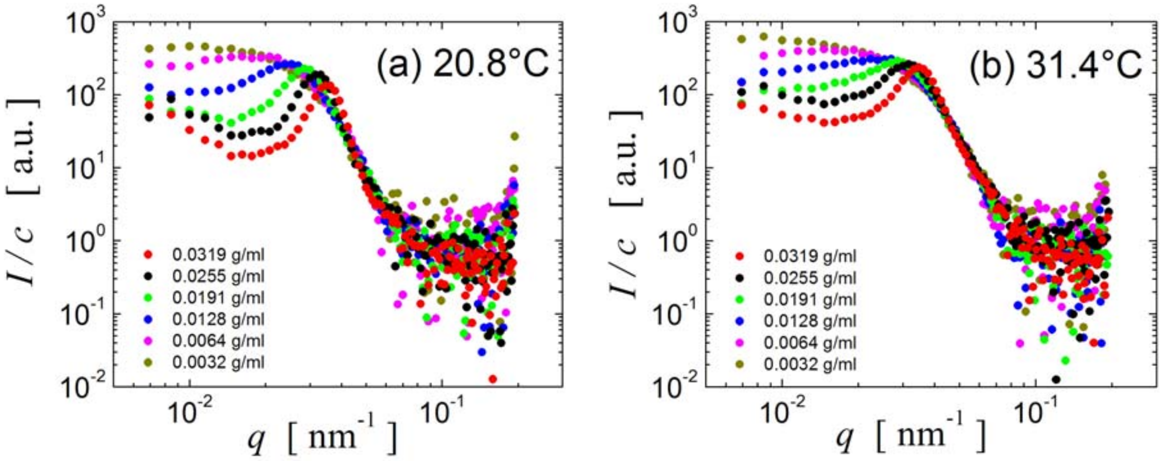

Figure V.2: Neutron scattering intensities as a function of q for sample A (red), B (black), C (green), D (blue), E (pink) and F (yellow). All intensities are normalized by the concentration of the sample.

$T = 31.4$°C. The q-dependence of the scattered intensity exhibits a pronounced dependence on concentration at both temperatures, as shown in Figure V.2, where we show the q-dependence of the scattered intensity normalized over the concentration in arbitrary units. For the lowest concentration (sample F) we recover a scattering profile reminiscent of the hard sphere form factor, the approximations yielding hard sphere radii of $R_s = 82$nm and $R_s = 72$nm at $T = 20.8$°C and $T = 31.4$°C respectively. These numbers agree reasonably well with the one obtained in static light scattering, where we would expect $R_G / R_S = 0.8$ for hard spheres; a comparison of the different sizes obtained is shown in Table V.3.

Sample	***c* [g/ml]**
A	0.0319
B	0.0255
C	0.0191
D	0.0128
E	0.0064
F	0.0032

Table V.2: Samples investigated by small angle neutron scattering. The concentrations indicated in g/ml refer to the one set at 20°C

T [ºC]	R_S [nm]	R_G [nm]	R_H [nm]	R_G / R_S	R_G / R_H	R_S / R_H
20.8	82	72	120	0.88	0.60	0.68
31.4	72	62	98	0.86	0.63	0.73

Table V.3: Comparison of the sizes obtained by using the Guinier approximation to fit the SLS data (R_G), the hard sphere form factor to approximate the SANS data (R_S) and by assuming Stokes-Einstein to determine the hydrodynamic radius (R_H) from the diffusion coefficient determined from the auto correlation function obtained in DLS.

For the samples at higher concentrations, sample A, B, C, D and E, the scattering profiles exhibit features that reflect the influence of a structure factor, $S(q)$. In particular, we observe the appearance of a peak, which becomes more pronounced and systematically shifts to larger q as the concentration increases. To properly determine the position of the peak reflecting the mean particle distance we need to extract $S(q)$ from the scattering intensity $I(q)$, which requires the knowledge of the form factor $F(q)$, as $I(q) = S(q) \cdot F(q)$. Previous SANS experiments on similar microgels revealed that the size of microgels somewhat depend on concentration, as the open structure of the microgels allows for compression [10]. This size change leading to a variation in the q-dependence of the form factor thus needs to be accounted for, when determining $S(q)$. Typically a radius change of ~20% is observed for a concentration range spanning from $\phi_{eff} = 0$ to $\phi_{eff} = 1$, where ϕ_{eff} is obtained by mapping the viscosity obtained at low concentrations to the one expected for hard spheres [10]. Tests on the effect of a decrease in size of 20% on $S(q)$ reveal that the absolute values of $S(q)$ are significantly lowered, but that the position of the peak, q_{peak}, varies only by 4%. Thus, we simplify our analysis assuming for a given temperature a constant size R_S to calculate $S(q)$ for all concentrations investigated, which we use to determine q_{peak} only. Nonetheless, we note that for the largest effective concentrations q_{peak} might be slightly smaller than indicated.

Interestingly, we find that q_{peak} does not vary much with temperature in the high concentration range and this despite the fact that the overall dimension of the microgel vary by 14-24 % as the temperature is varied from $T = 20.8$ºC to $T = 31.4$ºC. This indicates that the center to center distance between the particles is determined by the number concentration, which is usually the case for strongly repulsive systems that configure such that to achieve a maximal distance between the particles. In the case of PNiPAM microgels we can argue that the dependence on number concentration indicates that the microgels are closed packed at both temperatures, adopting a maximal distance of their center by either adjusting their size or adjusting the maximal penetration depth of their lower density shell; a schematic drawing of these 2 possibilities is shown in Figure V.3. The deviation of the linear dependence observed for $T = 31.4$ºC at $c \leq 0.019$ g/ml (sample C and D) and for $T = 20.8$ºC at $c = 0.0064$ g/ml (sample E), as shown in Figure V.4(a), indicates that the spheres in this sample are not closed packed anymore such that the peak position reflects a distance between particles that now mainly interact by excluded volume. To better evaluate our findings we estimate the effective center to center distances between the particles as $d = 2\pi / q_{peak}$, which we report as $d/2 = \pi / q_{peak}$ in Figure V.4(b) comparing them to R_S and R_H. Strikingly, we find the onset to the deviation from the linear dependence of $d/2$ observed for $T = 31.4$ºC at

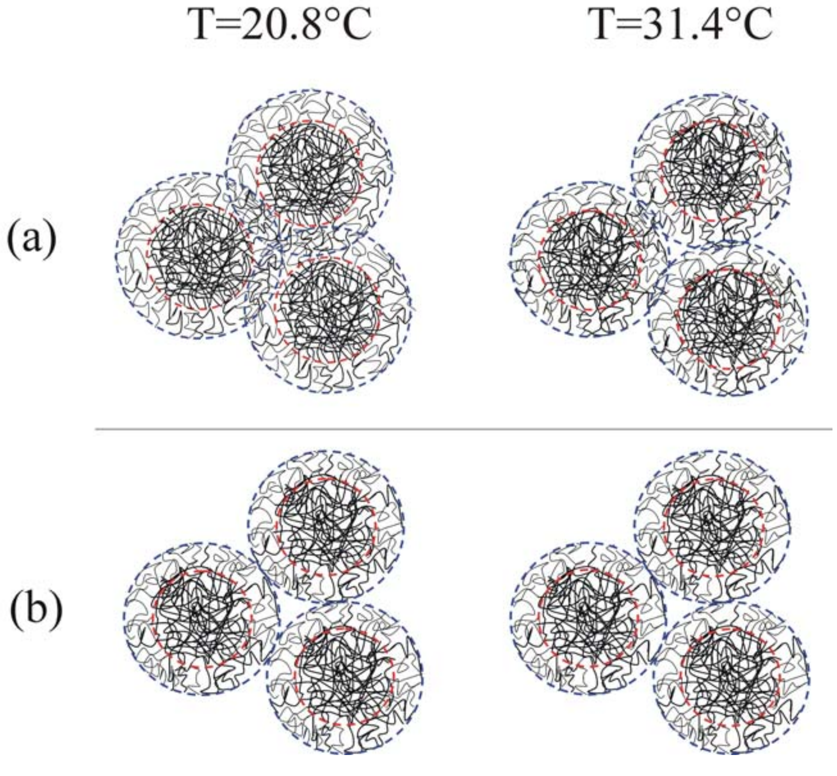

Figure V.3: Possible temperature dependent configurations of the microgels above close packing. (a) Interpenetration of the low density shells; (b) shrinkage of the overall dimensions of the particles. The number concentration establishes the center to center distance in both cases.

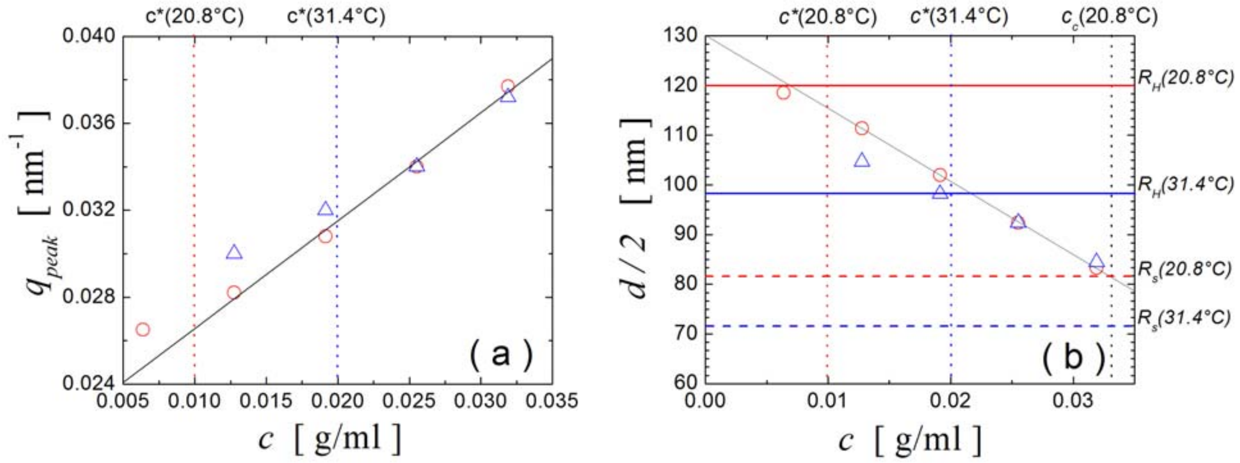

Figure V.4: (a) Position of particle-particle peak, q_{peak}, as a function of concentration for T=20.8°C (red circles) and T = 31.4°C (blue triangles). Vertical dotted lines indicate the concentrations $c*$ at which the data starts to deviate from the linear dependence. (b) Concentration dependence of the half center to center distance between particles as determined from q_{peak}. The horizontal solid lines indicate R_H and the dotted horizontal lines indicate R_s. The vertical dotted red and blue lines respectively indicate $c*$ at 20.8°C and 31.4°C. The vertical dotted black line indicates c_c at 20.8°C

$c* \sim 0.02$ g/ml and for $T = 20.8$ºC at $c* \sim 0.01$ g/ml to approximately coincide with R_H. This corroborate our assumption that the spheres are above the maximal packing condition at concentrations larger $c*$, adjusting for any increase of concentration above $c*$ by either shrinkage or interpenetration or a combination of both. To explore the consequences of this behavior on the mechanical properties of our systems we perform steady shear experiments using a commercial rheometer (Paar Physica MCR300) equipped with double gap and cone and plate geometries, respectively for experiments at low and high concentrations. We determine the low shear viscosity $\eta(c)$ for samples with concentrations ranging from $c = 5\cdot 10^{-4}$ g/ml to $c = 0.0295$ g/ml at temperatures ranging from $T = 20$ºC to $T = 31$ºC. Note that the indication of the concentration in g/ml again refers to the one used in our sample preparation at 20ºC; typically, we find less than 0.5% variation in the total volume of our sample for the temperature range investigated, leading to an error of less than 0.02% in the indication of the concentration in g/ml.

Within the concentration range investigated we find that $\eta(c)$ varies by a factor of ~400 at 20ºC, while varying only by a factor of ~4 at 31ºC, as shown in Figure V.5(a), where we display the concentration dependence of the low shear viscosity normalized by the viscosity of the background fluid η_0. We can entirely account for the systematic variation in the concentration dependence of $\eta(c)$ with temperature by considering the change in the particle volume. Indeed, the simple normalization of the concentration by the ratio $(R_H(T)/R_H(20ºC))^3$ collapses the data onto a master curve, as shown in Figure V.5(b) where we use $R_H(20ºC)$ as a reference radius, such that the concentration axis refers to the one obtained at 20ºC. This almost perfect collapse of the data obtained in the range of $T = 20ºC - 31ºC$ by simply accounting for the temperature dependent dimensions of the microgel indicates that the particle-particle interactions remain unchanged within this temperature range and at first sight would also imply that the particles interact purely by excluded volume. Indeed, we find the viscosity to diverge at

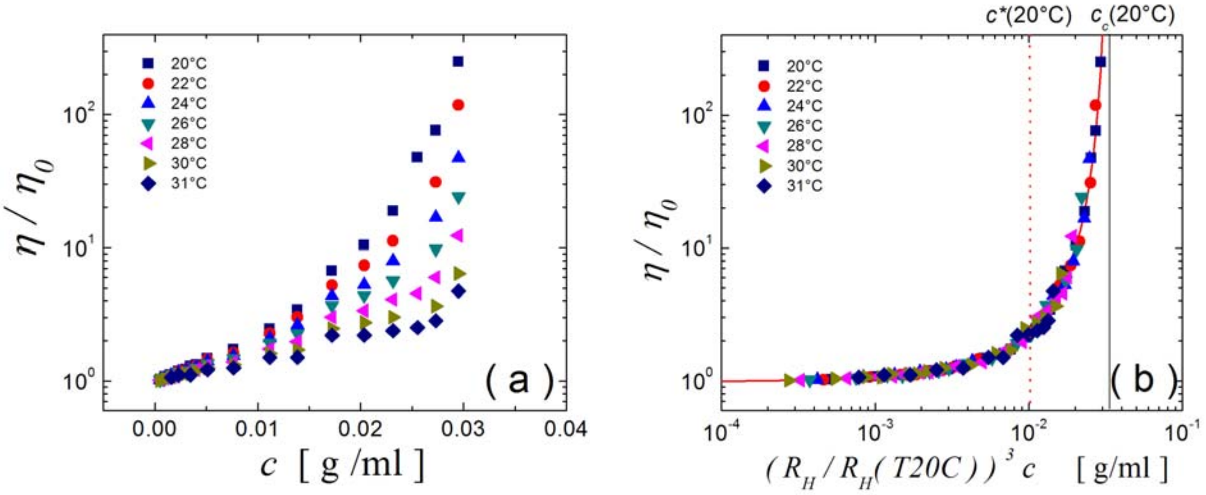

Figure V.5: (a) Relative low shear viscosity versus concentration for 20°C (blue squares), 22°C (red diamonds), 24°C (blue triangles), 26°C (green triangles), 28°C (pink triangles), 30°C (yellow triangles) and 31°C (blue diamonds). (b) Relative low shear viscosity versus rescaled concentration yielding a master curve. The red line corresponds to a fit of the data to a critical-like function $\eta(c)/\eta_0 = (1 - c / c_c)^{\beta}$. The dotted red line indicates c^* at 20.8°C and the continuous black line indicates c_c at 20.8°C as well.

some critical concentration, which is strongly reminiscent of the behavior expected for hard sphere colloids. The typical critical-like function known to describe hard sphere behavior, $\eta(c)/\eta_0 = (1 - c \;/\; c_c)^{\beta}$, describes our data well, as shown by the continuous line in Figure V.5(b). This finding is somewhat surprising when considered within the context of the neutron scattering results that indicate that the microgel spheres are able to adapt beyond the closed packing condition of their unperturbed dimension c^*, which we indicate as dotted line in Figure V.5(b). Both proposed scenarios, interpenetration and shrinkage, should in principle lead to a power-law increase of the viscosity beyond c^*, but would somewhat preclude the critical-like divergence that is observed. An important indication leading to a better understanding of the observed behavior is obtained by considering the results of the critical like fit, where we find $\beta = 2.5$ and $c_c = 0.033$ g/ml for $T = 20$ºC. This critical concentration, c_c, corresponds approximately to the one where we would expect $d/2$ to correspond to R_S, as indicated in Figure V.4(b). This implies that the divergence of the viscosity occurs when the higher density cores become closed packed, which agrees somewhat better with the scenario of an interpenetration of the low density shell than with the scenario of the shrinking dimensions, as there is no obvious reason to assume that the maximal shrinkage would be reached at R_S. Indeed, considering the dimensions obtained at $T = 40$ºC we would expect that the maximal shrinkage would be reached at about $0.6{\cdot}R_s$. The critical exponent, β, being larger than the one typically expected for hard spheres ($\beta = 2$) [11] indicates that the critical-like increase is further ranged in the microgel systems than in hard sphere systems; this reflects the intermediate nature of our microgels that exhibit a behavior intermediate between polymer-like and hard-sphere-like behavior between $c^* \sim 1/R_H^3$ and $c_c \sim 1/R_S^3$. To gain some intuition about the correspondence between the concentrations given in mass per volume (c) and the effective volume fractions (Φ_{eff}) we fit our viscosity data in the low concentration range to the Batchelor equation for hard sphere suspensions, $\eta/\eta_0 = 1 + 2.5\,\Phi_{eff} + 5.9\,\Phi_{eff}^2$, adapting Φ_{eff} to νc. We find for our PNiPAM-microgel solutions at 20°C that $\nu \sim 26$ ml/g, which leads to a correspondence of c^* to $\Phi^*_{eff} \sim 0.26$ and c_c to $\Phi_{eff\,c} \sim 0.86$. Assuming that the typical random close packing conditions are about $\Phi_{rcp} \sim 0.6$ we find that $\Phi^*_{\ddot{e}ff}$ is significantly lower than Φ_{rcp}, which is somewhat inconsistent with proposed scenario of c^* corresponding to the random closed packing condition of the unperturbed spheres. We note, however, that our determination of $\Phi_{\ddot{e}ff}$ is based on the hydrodynamically effective volume of the spheres; as mentioned above the real dimensions of the sphere are likely to be larger than R_H as the low density outer edge of the spheres would allow for free drainage. Indeed, considering the real radius to be a factor of 1.3 larger than R_H would lead to $\Phi^* = \Phi_{rcp}$. The fact that $\Phi_{eff\ c} > \Phi_{rcp}$ is expected, as we inferred that the critical volume fraction at which the viscosity eventually diverges correspond to the random close packing of the core; the core volume fraction being much smaller than $\Phi_{\ddot{e}ff}$ we find $\Phi_{eff\ c} > \Phi_{rcp}$.

In conclusion we find that within the temperature range of $T = 20$ºC-31ºC the behavior of our microgels is exclusively determined by their core-shell nature, exhibiting no evidence of a variation in their particle interaction potential. The temperature dependent behavior at all concentrations can simply be accounted for by considering the change in dimension observed in the dilute limit. In the high concentration range we find that the center to center distance is determined by the number concentration, disclosing the interpenetrable nature of our microgel system. The limit of interpenetration is set by the high density core, which eventually leads to a divergence of the viscosity as the concentration becomes high enough, so that the cores become random closed packed.

For the temperature range of $T = 33$ºC-35ºC we find some evidence that the particle-particle interactions becomes slightly attractive. For the temperature range above the LCST we find that our systems gel, as discussed in the next section.

Properties of PNiPAM microgels above the LCST.

As the temperature is increased above the LCST we find that the optical properties of our samples dramatically change, as shown in Figure V.6. Below the LCST the sample is clear; by contrast, above the LCST the sample is completely turbid. The reason for this switch from transparent to turbid is twofold: a) the optical contrast between particle and solvent considerably increases as the particle becomes insoluble at high temperatures [8]; b) the particles become sticky at high temperatures, which leads to the formation of larger aggregates that exhibit enhanced forward scattering. Note, that our microgels only aggregate, when the residual charges are sufficiently screened. Increasing the temperature of a PNiPAM microgel sample without added electrolyte results in an increased turbidity because of the increase of the optical contrast between particle and solvent only, which is far less pronounced than the effect observed for the aggregating system. Indeed, the highly multiple scattering properties of our screened systems at temperatures above the LCST preclude any characterization of these systems by means of light or neutron scattering unless the samples are considerably diluted. Thus, to gain structural information of the aggregates formed at larger concentrations we use transmission light microscopy using thin samples to avoid extended multiple scattering effects. Additionally, we characterize the aggregates formed in the highly dilute limit using static light scattering. To gain insight in the dynamics of our systems we use diffusing wave spectroscopy. The list of the samples used in these studies is given in Table V.4, where we also indicate the effective volume fraction at 31.4 C and 40 C. We indicate Φ_{eff} for 31.4 C as we use this temperature to equilibrate our sample in the repulsive limit prior to any temperature quench above the LCST. This protocol ensures that the microgels are well dispersed before the quench. We indicate Φ_{eff} for 40 C only, as

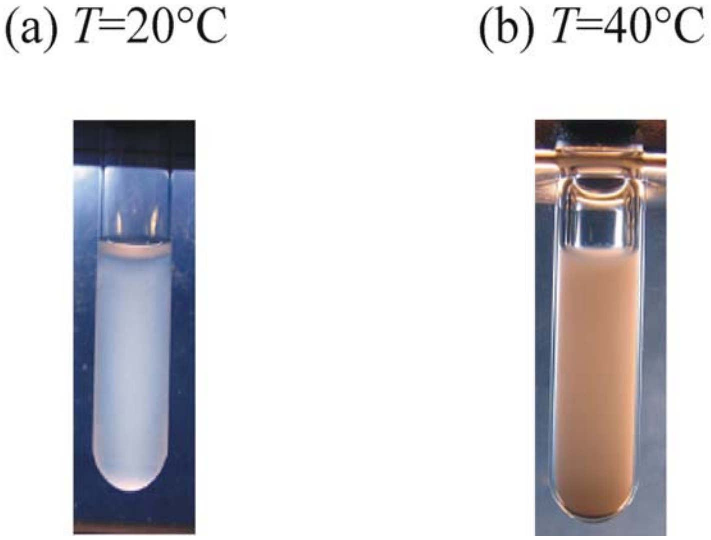

Figure V.6: Microgel suspension (c = 0.006 g/ml) at (a) T = 20°C and at (b) T = 40°C.

we estimate that Φ_{eff} of a given sample does not vary by more than 2% in the temperature range of T = 36-40ºC, which is the temperature range investigated.

	c [g ml^{-1}]	Φ_{eff} (31.4°C)	Φ_{eff} (40°C)
SLS	0.0004	0.0053	0.0007
microscopy	0.0022	0.0295	0.0040
	0.0200	0.2679	0.0367
	0.0295	0.3951	0.0541
DWS	0.0138	0.1848	0.0253
	0.0255	0.3416	0.0468
	0.0295	0.3951	0.0541

Table V.4: List of samples investigated in the high temperature range, where the PNiPAM-particles become attractive.

For our microscopy experiments we use a light microscope from Leica with a 10x objective, which is equipped with a commercial shear cell from Linkam scientific instruments that allows for a precise setting of both the thickness of the sample and the temperature. We set the thickness of the sample to be 100 μm. For the acquisition of images we use a complementary metal-oxide-semiconductor (CMOS) camera from IDT (X-stream Vision Monochrom Digital Camera) using an integration time of 15ms; our image size is 768x528 pixels with a pixel size of $\rho = 1.202 \cdot 10^{-3}$ mm/pixel. We equilibrate our sample below the LCST at 31.4°C. At this temperature our microgel suspensions are stable, exhibiting a characteristic size of R_S = 72 nm. This size being far below the resolution of light, our microscope images appear homogeneous, as shown in Figure V.7(a). Upon increase of the temperature above the LCST we observe the formation of large scale structures that appear to have a well defined characteristic length, as shown for 40°C in Figure V.7(b). Decreasing the temperature again to 31.4°C these structures melt and the suspension reverts back to a fully dispersed state, which is again evidenced by the homogeneous appearance of our sample in microscopy, as shown Figure V.7(c). We take advantage of this remarkable reversibility to realize several configurations of the structures formed at different temperatures, ramping consequently

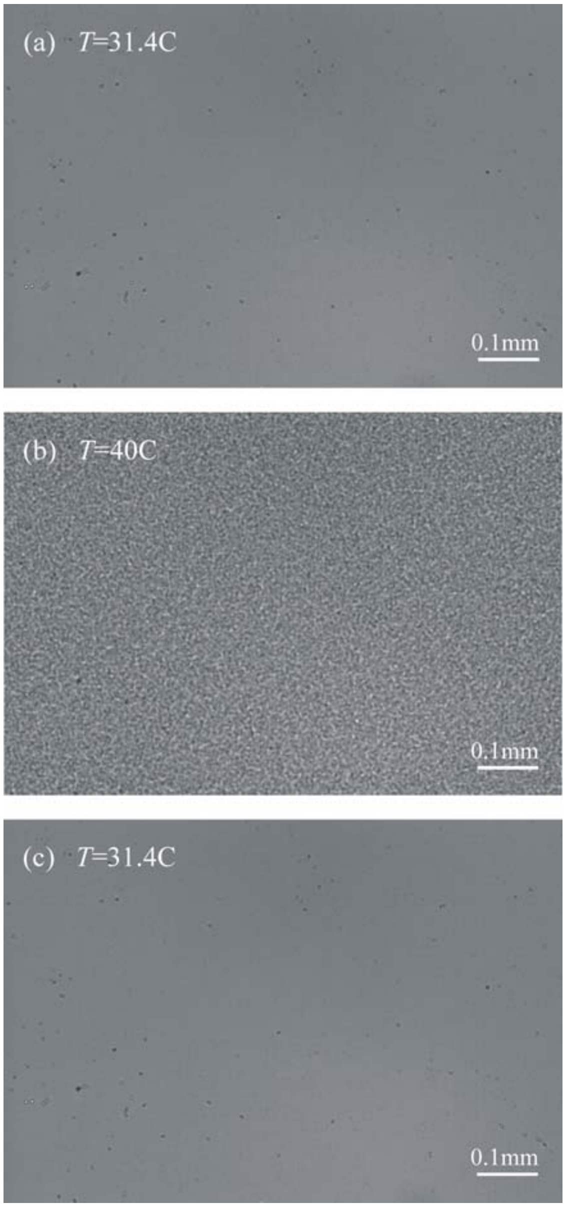

Figure V.7: Normalized images of a microgel suspension at a concentration of $c = 0.0295$g/ml.

(a) Equilibration before temperature jump at 31.4°C
(b) 2 Min. after temp jump to 40°C
(c) 6 Min. after decreasing the temperature again to 31.4°C

from 31.4°C to the desired temperature and back again. For each temperature we perform this experiment 10 times taking an image 2 minutes after the structures are formed. This relatively short equilibration time appears justified as several time resolved experiments revealed that these structures do not significantly evolve in time.

To more quantitatively determine the structural hallmarks of our systems we transform our images from real space to Fourier space using a Fast Fourier Transform (FFT) routine. As an example we show the micrographs and the corresponding FFT of the structures formed at $T = 40^{\circ}\mathrm{C}$ for $c = 0.0200$ g/ml and $c = 0.0295$ g/ml in Figure V.8. The FFTs exhibit a ring that reflects the characteristic length of our systems. To quantify this feature we perform azimuthal averages over equally spaced rings and report the averaged intensity as a function of the magnitude of the wave-vector q in Figure V.9, where we define q as $q = \dfrac{2\pi}{\rho}\dfrac{n}{L}$ with L the size of the image and n the radius of the ring in units of pixels. Prior to the FFT transform, all images are normalized by the average

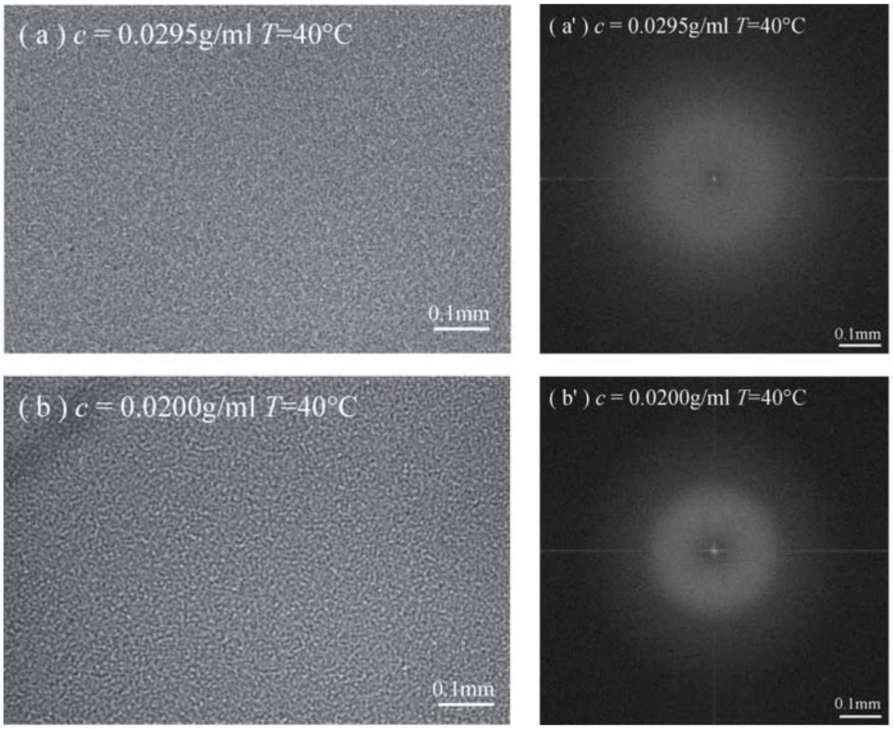
(a) c = 0.0295g/ml T=40°C
0.1mm
(a') c = 0.0295g/ml T=40°C
0.1mm
(b) c = 0.0200g/ml T=40°C
0.1mm
(b') c = 0.0200g/ml T=40°C
0.1mm

Figure V.8: (a) and (b) are normalized images of the gel phase at $c = 0.0295$ g/ml and $c = 0.0200$ g/ml, respectively. (a') and (b') are the corresponding FFT transforms exhibiting a ring revealing the presence of a characteristic size.

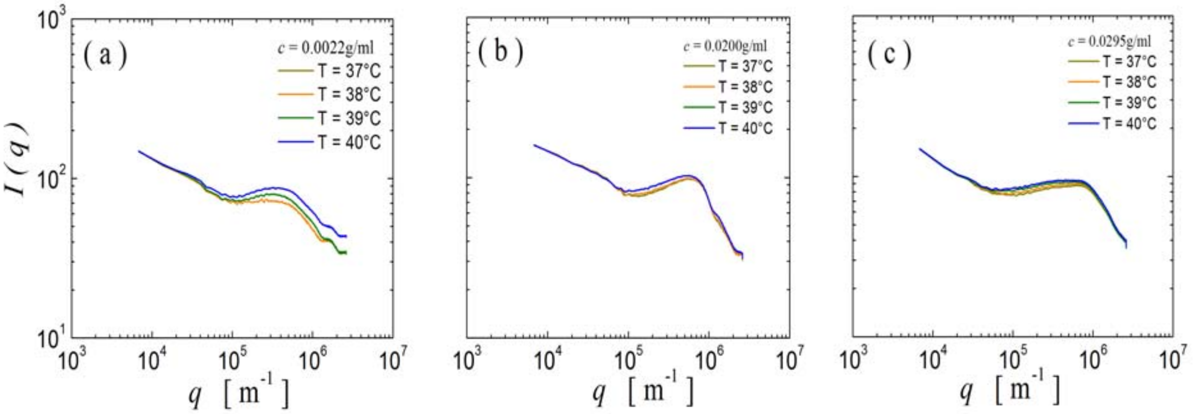

Figure V.9: Static structure factors obtained from microscopy. The intensities are normalized with the average intensity at T = 31.4°C. The microgel concentrations are at (a) c = 0.0022g/ml, (b) c = 0.0200g/ml and (c) c = 0.0295g/ml. The different experiments are at T = 40°C (orange), T = 39°C (blue), T = 38°C (yellow), T = 37°C (dark blue) and T = 36°C (green).

intensity of images taken just before the temperature jump at $T = 31.4$ °C; this procedure should account for variation in the intensity of our light source and make our experiments comparable. Each intensity curve is an average taken over the 10 individual temperature jumps performed for each temperature.

For the three concentrations investigated, $c = 0.0022$ g/ml, $c = 0.0200$ g/ml and $c = 0.0295$ g/ml, the intensity profile is characterized by a peak that is indicative for the structural length of our systems. Note that the apparent intensity increase observed at low q is due to the finite size of our image and is of no physical meaning. Surprisingly the peak position shows nearly no dependence on temperature and only little dependence on volume fraction, evolving from $q_{peak,aggreg.} = 374\,\mathrm{mm}^{-1}$ at $c = 0.0022$ g/ml to $q_{peak,aggreg.} = 724\,\mathrm{mm}^{-1}$ at $c = 0.0295$ g/ml. From the peak position, $q_{peak,aggreg.}$, we can infer a characteristic length $\xi = \pi / q_{peak,aggreg.} = 8.4$, 5.5 and 4.3µm for $c = 0.0022$ g/ml, $c = 0.0200$ g/ml and $c = 0.0295$ g/ml respectively, which corresponds approximately to 200-100 particle radii.

To gain further insight in the aggregation behavior of our systems we investigate the effect of a quench from 31.4ºC to $T = 36$ºC and $T = 40$ºC by static light scattering using a dilute sample ($c = 4\cdot10^{-4}$ g/ml). To cover a wide range of q we perform the experiments using the small- and wide-angle setups described in Chapter II and follow the evolution of the light scattered by our sample in time. We find that the scattering profile in the q-range accessible in our wide-angle experiments ($q = 4\cdot10^{6}$-$3\cdot10^{7}$ m^{-1}) does not change significantly after a 15 min equilibration period at a given temperature $T > T_c$, while the scattering profile in the q-range accessible in our small-angle experiments ($q = 1.4\cdot10^{5}$-$1.7\cdot10^{6}$ m^{-1}) changes continuously over the entire duration of our experiments of ~1.5 h. At even longer waiting times (~4h) we observe the formation of large macroscopic flocks, which precludes further investigations by light scattering. In Figure V.10 we show the q-dependence of scattered intensity after an equilibration time at respectively $T = 36$ºC and $T = 40$ºC of $t = 3400$ s. Remarkably, we find for both temperatures that the scattered intensity exhibits a very strong dependence on q in the high q-range best described by $I(q) \sim q^{-4}$. Such q^{-4}-dependence indicates the formation of compact objects with sharp interfaces, which is unusual for an aggregating system, where we generally expect fractal-type structures to build up. Indeed, the q-dependence of $I(q)$ in the low q-range corresponds to the one typically expected in fractal aggregation; the

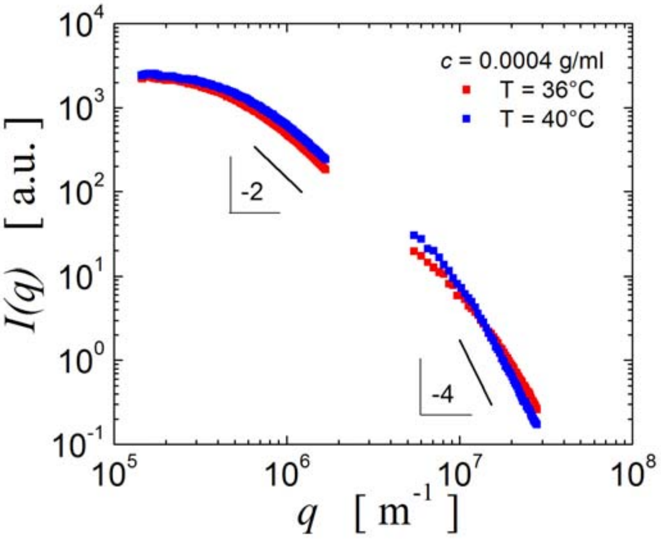

Figure V.10: Static form factors of aggregated microgel particles at a concentration of $c = 0.0004$ g/ml at $T = 36$°C (red squares) and $T = 40$°C (blue squares).

scattered intensity exhibits a characteristic crossover from a q^0-dependence at very low q to an approximately q^{-2}-dependence at larger q that is characteristic for fractal clusters. Our findings are consistent with the initial formation of compact objects that subsequently aggregate to form fractal-type clusters, which eventually become large enough to be visible by eye. From the position of the cross-over from a q^{-2}- to a q^{-4}-dependence we estimate the diameter of the compact object to be ~800-900 nm, which corresponds to 8-9 particle diameters. From the position of the cross-over from a q^0- to a q^{-2}-dependence we estimate the cluster-radius to be ~ 6 μm, which is very similar to the characteristic length obtained in our high concentration gels. Note, however, that the cluster size continues to increase after $t = 3400$s, which is the equilibration time used for our experiment.

Nonetheless, the formation of compact objects suggests that the aggregation of our PNiPAM-systems initially proceeds by a liquid-liquid phase separation that becomes arrested as the local density reaches the critical conditions for dynamic arrest [12]. While this leads to the formation of individual, probably spherical, objects at low concentration, which develop by a nucleation and growth mechanism, it is conceivable that the liquid-liquid phase separation proceeds via spinodal decomposition at larger concentrations, which leads to the formation of a network structure with a characteristic size, as the one denoted in our microscopy experiments. Alternatively, our high concentration gels might as well form via a nucleation growth process, the concentration of the formed droplets now being sufficiently high to lead to the formation of a stress-bearing network via aggregation.

To gain insight in the dynamical properties of our gels we use Diffusing Wave Spectroscopy [13]. We restrict our study to the gels formed at $c = 0.0138$, 0.0255 and 0.0295 g/ml, for which the turbidity is large enough to ensure the strong multiple scattering properties required for DWS. For these volume fractions the transport mean free path l^* exhibits only little dependence on both, concentration and temperature. As shown in Figure V.11, l^* varies between 240 μm and 340 μm. For all our DWS experiments we use a square cell with a path-length of $L = 2$ mm, corresponding to $L / l^* = 7 \pm 1$, which is still within the limit of the condition required for DWS [14]. To access both the short and long time dynamics, we measure the intensity fluctuations of

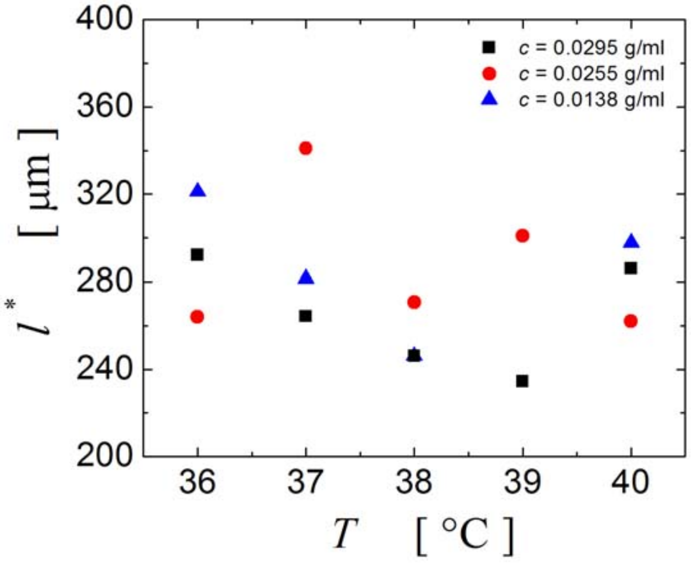

Figure V.11: Temperature dependence of the transport mean free path, *l**, at concentrations of c = 0.0295g/ml (black squares), c = 0.0255g/ml (red circles) and c = 0.0138g/ml (blue triangles).

the light scattered by our sample using simultaneously a photo-multiplier and a CCD-camera, both being implemented in our DWS-set-up as described in Chapter II. The signal of the photo-multiplier is processed in real time using a commercial hardware-correlator that give access to the time averaged degree of correlation $g_2(\tau)$ over a lag-time window of $\tau = 10^{-8}\text{-}5\cdot10^{1}$s. By contrast the CCD-images are recorded at a rate 3.33 Hz using an exposure time of 0.2ms and processed subsequently following the procedure of the recently introduced TRC-method [15] that gives access to the instantaneous degree of correlation $c_I(t_w,\tau)$ over a lag-time window of 0.3 s to several thousand seconds. As done in the structural investigations with microscopy and static light scattering we equilibrate our system at a temperature $T = 31.4$°C prior to any experiment. The suspension is then transferred to the DWS-set up, whose bath is set at a temperature above the LCST. We define this moment at which the sample is set to its final temperature as $t = 0$ s. The initially transparent suspension becomes turbid within 1 minute. To ensure that the detectors are not destroyed by directly transmitted light, we start the acquisition with the photo-multiplier at $t = 2$ minutes and the acquisition with the CCD at $t = 3$ minutes. We find that the short time dynamics of our systems evolves to its final profile in less then 5 minutes, while the long time dynamics evolves over the entire course of the experiment, which typically lasts 24 hours.

In contrast to the structural hallmarks of our systems that exhibit only little dependence on concentration and temperature, we find that the short time dynamics strongly depends on both. For the three concentrations investigated and $T \geq 36°C$ we find that the intensity correlation function is characterized by a first decay followed by a plateau, which is indicative of constraint thermal fluctuations. Both the first decay and the height of the plateau systematically increase as the temperature and volume fraction increases, as shown in Figure V.12. To better account for the dynamics observed we calculate the time dependent mean squared displacements (MSD) from our correlation functions, reporting the results in Figure V.13 and Figure V.14, where we organize the data in sets displaying the effect of temperature at a given concentration (Figure V.13) and the effect of concentration at a given temperature (Figure V.14). To account for the temperature-dependent changes in the background viscosity we normalize our time axis by the ratio of the solvent viscosity at 20°C and the one at the temperature investigated, $\eta_0(20°C)/\ \eta_0(T)$. Surprisingly, we find no common time-dependence of the MSD at very short times and this neither in the variation in concentration nor in the variation of the

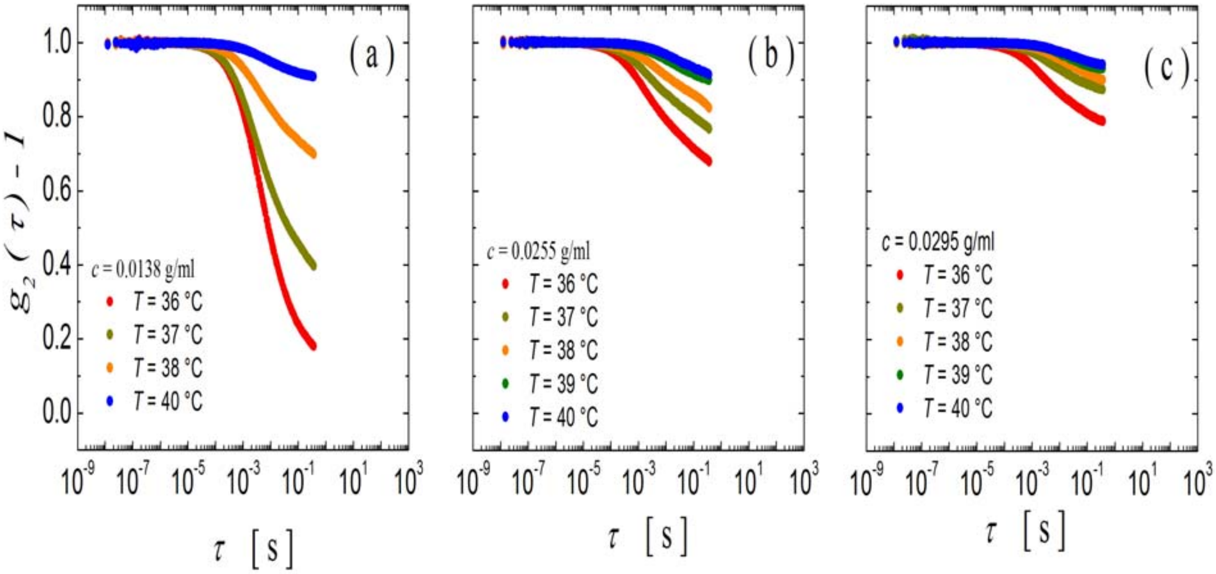

Figure V.12: DWS Correlation functions obtained for microgel suspensions at concentrations of (a) $c = 0.0138$g/ml, (b) $c = 0.0255$g/ml and (c) $c = 0.0295$g/ml.

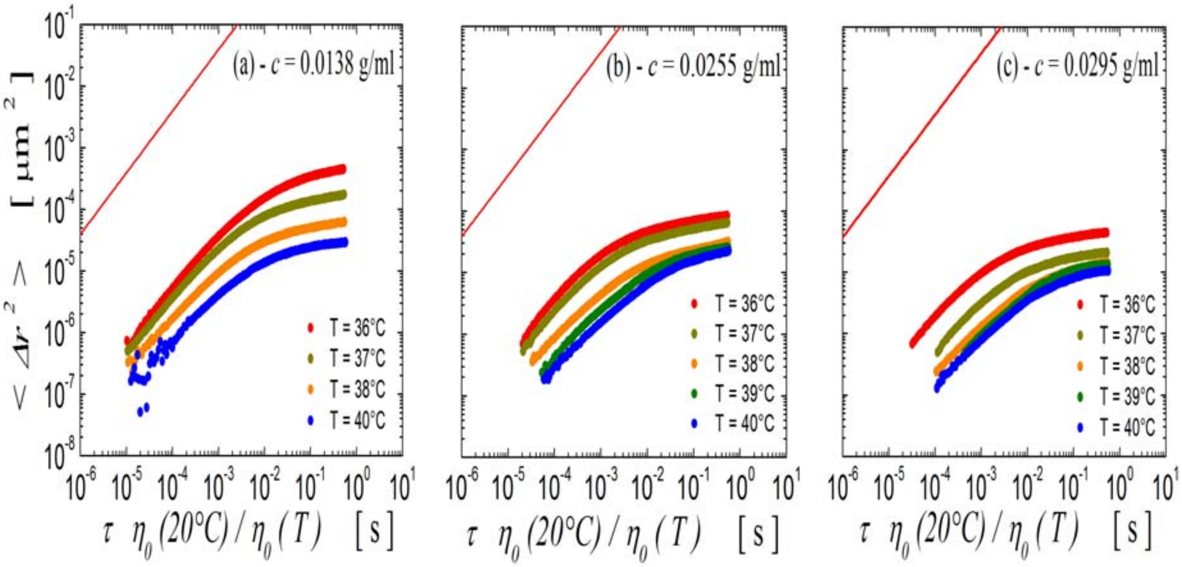

Figure V.13: Short time dynamics of microgel networks at fixed concentration and varying temperature. The concentrations are c = 0.0138 g/ml (a), c = 0.0255 g/ml (b) and c = 0.0295 g/ml (c). The temperatures are T = 40°C (blue), T = 39°C (green), T = 38°C (orange), T = 37°C (yellow) and T = 36°C (red). The solid lines correspond to the behaviour expected for free diffusion of individual particles.

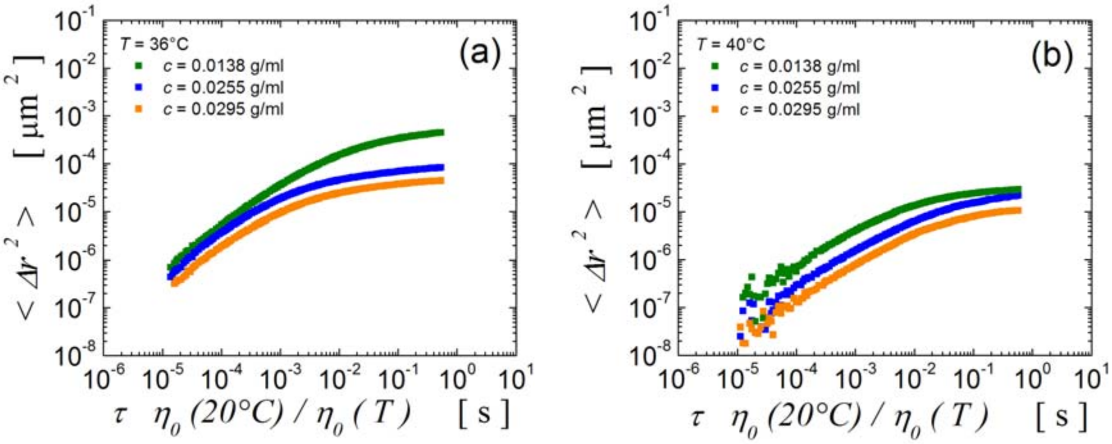

Figure V.14: MSDs of aggregated microgel particles at (a) T = 36°C and (b) T = 40°C. In each set of data the concentrations are c = 0.0138 g/ml (green), c = 0.0255 g/ml (blue) and c = 0.0295 g/ml (orange).

temperature. This is in stark contrast to the behavior found for the colloidal gels discussed in Chapter III, where we found that a set of samples with varying Φ and fixed interaction potential exhibits a common short-time spectrum; this short-time spectrum being near to the one expected for freely diffusing particles. To gain some intuition about the observed short-time dynamics we additionally indicate the behavior expected for free diffusion in Figure V.13, where the free diffusion is calculated using the Beenaker-Mazur equation [16] to account for the changes in the effective volume fractions, Φ_{eff} (*40°C*). Clearly, the short time dynamics of our samples differ significantly from the one expected for the free diffusion of the individual particles. To quantify this behavior we fit the correlation functions to a stretched exponential function, $\sqrt{g_2 - 1} = \exp\left\{-\left[\tau / \tau_o (l^* / L)^2\right]^p\right\}$, and report the ratio of τ_0 / τ_{DIFF} in Figure V.15(a), where τ_{DIFF} corresponds to the characteristic time expected for the free diffusion of individual particles. For all concentrations and temperatures investigated we find τ_0 / τ_{DIFF} to be larger than 1000, increasing by a factor of ~100 as the temperature is increased from $T = 36$°C to $T = 40$°C. The extremely large values of τ_0 / τ_{DIFF} seemingly indicate that the thermally induced motion in our gels involves the motion of regions that are much larger than any of the characteristic structural lengths that we detect in microscopy or static light scattering. Within this region the dynamics is essentially frozen, such that this region represents the dynamically relevant base unit of our system.

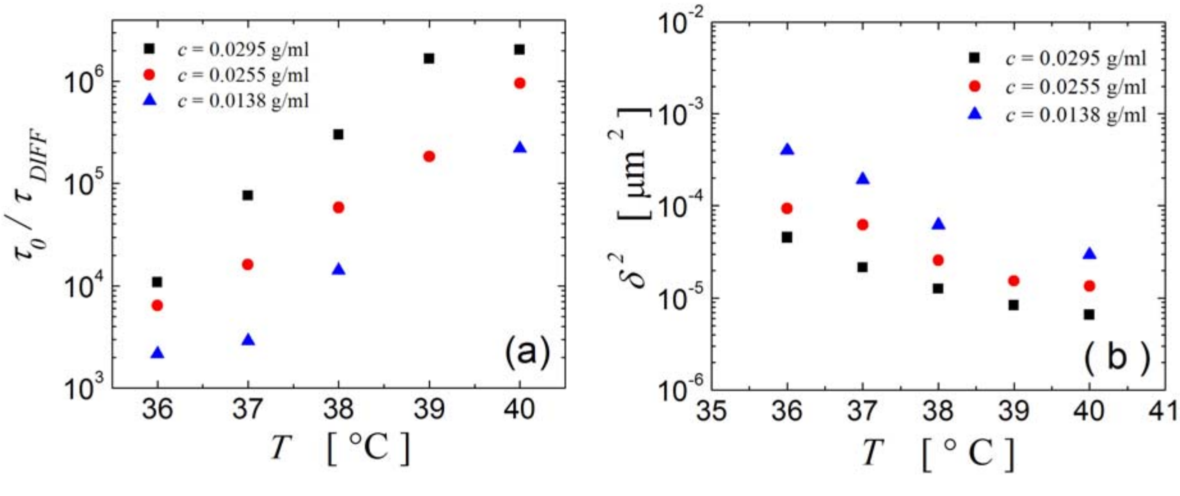

Figure V.15: (a) Temperature dependence of the short time relaxation time normalized by the one expected for the free diffusion of individual particles. (b) Temperature dependence of the MSDs plateau values. The microgel concentrations are c = 0.0295 g/ml (black squares), c =0.0255 g/ml (red circles) and c = 0.0138 g/ml (blue triangles).

The strong variation of τ_0 / τ_{DIFF} with temperature seemingly indicates that this unit becomes significantly larger as the temperature is increased. Note, that we can not simply attribute the slowing down of the short-time dynamics as being due to an increase in particle-particle spring constant, as this should lead to a decrease of the cross-over time τ_c characterizing the transition from the sub-diffusive regime to the plateau regime [see Chapter III]. We, however, find this cross-over time to increase with temperature. That our gels nonetheless become more rigid as the temperature increases can be inferred from the fact that the maximum mean squared displacement δ^2 systematically decreases with temperature, as shown in Figure V.15(b). Though a consistent model describing the entire spectrum of the short–time dynamics is still missing, we believe this spectrum to be determined by both, a temperature dependent size of the dynamically relevant base unit and a temperature dependent spring constant; both the size of the base unit and the spring constant increases with temperature.

As mentioned above we find that the short-time dynamics of our gels ceases to evolve shortly after the temperature jump from 31.4°C to $T > T_c$. By contrast, our gels exhibit a slow structural relaxation process that evolves over the entire duration of our experiments of ~24h. Intriguingly, we find two types of evolutionary processes. For deep quenches to high temperatures and/or large concentrations the slow relaxation initially slows down to then speed up again, exhibiting at longer times a continuous slowing down, as seen in the TRC-traces for the gel formed at $c = 0.0255$ g/ml and $T = 40$°C in Figure V.16(a). Indeed, an increase of the instantaneous degree of correlation $c_I(t,\tau)$ at different lag-times τ corresponds to a decrease of the decay rate of the momentary correlation function. Accordingly a decrease of the $c_I(t,\tau)$ at different τ corresponds to an increase of the decay rate of the momentary correlation function; the momentary correlation being simply read as a vertical cut (t = constant) through the TRC-traces calculated for various lag-times. In contrast to the deep quenches, the TRC-traces exhibit a continuous increase in time for shallower quenches to not too high temperatures and/or concentrations, as shown for the gel formed at $c = 0.0255$ g/ml and $T = 38$°C in Figure V.16(b). We want to emphasize, that the two examples shown, $c = 0.0255$ g/ml at respectively $T = 40$°C and $T = 38$°C, are representative for deep and shallow quenches, the transition between the two being shifted to lower temperatures at higher

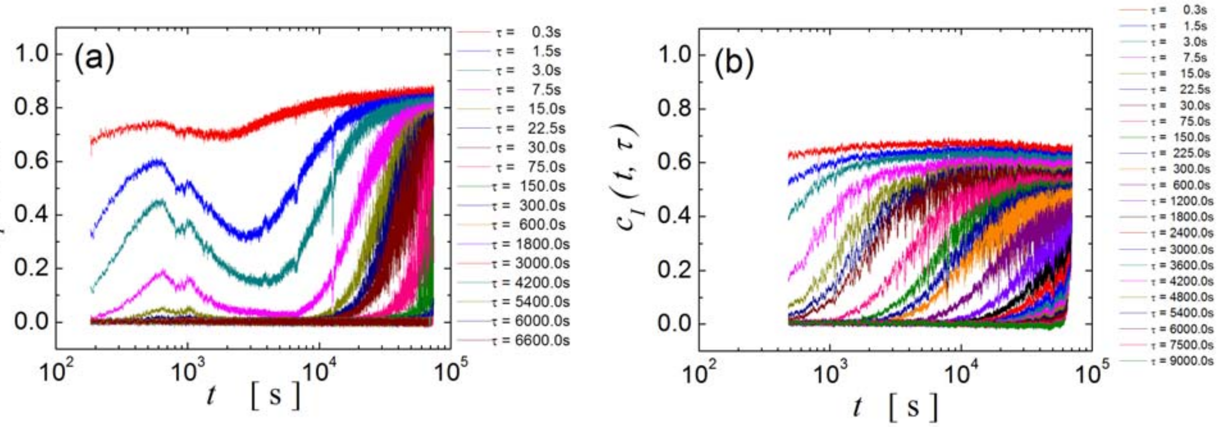

Figure V.16: Time evolution of the instantaneous degree of correlation after a temperature jump to (a) T = 40°C and (b) T = 38°C. In both graphs the concentration is c = 0.0255 g/ml. The different lag times are indicated next to the graphs.

concentrations. We tentatively interpret these intriguing changes in the evolution of the structural relaxation as being due to increased imbalances in the quenched-in internal stresses as the quench depth becomes larger; this imbalances leading to an intermediate faster restructuring rate, till the initially quenched stresses are released, the following evolution being then due to the bond-forming and bond-breaking mechanism that has been inferred to account for the aging behavior of other colloidal gels [17]. Moreover, we note that our TRC-traces are characterized by strong fluctuations, which indicate that our structural relaxation process is determined by high temporal heterogeneities. At some moments in time $c_I(t, \tau)$ drops significantly below the mean, which indicate that the dynamics becomes sporadically faster. We attribute this increase in the dynamics to an intermittent restructuring process involving larger portions of our samples. Indeed, extended visual observations of lower concentration gels reveal that our gels formed by PNiPAM-microgels have a tendency to shrink. We could conceive that at larger concentration this shrinking process leads to micro-collapses, where small portion of the gel detaches from the surrounding network forming a more compact object that then reattaches at another location.

Our understanding of the gels formed by PNiPAM-microgels is certainly far from complete. Further investigations are needed to critically evaluate the role of phase separation in the gel formation, the origin of the slowing down of the thermally induced fluctuations, as well as the role of shrinkage determining the structural relaxation. Nonetheless, our study presents to our knowledge the first attempt to systematically investigate the structure and dynamics of this type of gels.

Summary.

We investigated the temperature dependent behavior of PNiPAM-microgel systems as a function of concentration. Below the lower critical solution temperature we find that the temperature dependence of mechanical properties of our microgel systems is essentially determined by the temperature dependence of the microgel-dimensions. However, the characterization of microgel solutions at low concentrations, as well as measurements of the static structure factor of microgel solutions at high concentrations reveals that our microgels are best described as core-shell particles. At high concentrations the shell appears to be fully interpenetrable seemingly allowing for a maximum packing of the microgels up to a concentration at which the core volume fraction reaches the random close packing condition; this concentration corresponding to the one at which we observe the divergence of the viscosity. Above the lower critical temperature our microgel systems becomes attractive and form at large enough concentrations stress bearing gels. Our data indicate that aggregation at least initially proceeds via a liquid-liquid phase separation, which leads to the formation of larger objects with sharp interfaces. Whether the gelation at larger concentrations occurs via spinodal decomposition or an initial formation of compact droplets that subsequently aggregate remains an open question. Somewhat surprisingly we find that the dynamics of our gels is strongly determined by temperature, while we find no evidence for considerable structural differences. Thus, while it appears that temperature only determines the intra-molecular interactions within the microgel particles at temperatures below the LCST, it strongly determines the inter-molecular interactions between the microgel particles at temperatures above the LCST.

References.

1. R. B. Saunders and B. Vincent, *Microgel particles as model colloids: theory, properties and applications.* Advances in Colloid and Interface Science, 1999. **80**(1): p. 1-25.
2. H. Senff and W. Richtering, *Influence of Cross-Link Density on Rheological Properties of Temperature-Sensitive Microgel Suspensions.* Colloid and Polymer Science, 2000. **278**(9): p. 830-840.
3. A. F. Routh and B. Vincent, *Salt-Induced Homoaggregation of Poly(N-isopropylacrylamide) Microgels.* Langmuir, 2002. **18**(14): p. 5366-5369.
4. A. Fernandez-Nieves, et al., *Reversible Aggregation of Soft Particles.* Langmuir, 2001. **17**(6): p. 1841-1846.
5. A. Fernandez-Nieves, et al., *Structure Formation from Mesoscopic Soft Particles.* Physical Review E, 2001. **64**(5): p. 051603-1 051603-1.
6. J. Wu, B. Zhou, and H. Zhibing, *Phase Behavior of Thermally Responsive Microgel Colloids.* Physical Review Letters, 2003. **90**(4): p. 048304-1 048304-4.
7. H. Senff and W. Richtering, *Temperature sensitive microgel suspensions: Colloidal phase behavior and rheology of soft spheres.* Journal of Chemical Physics, 1999. **111**(4): p. 1705-1711.
8. E. Daly and B. R. Saunders, *A Study of the Effect of Electrolyte on the Swelling and Stability of Poly(N-isopropylacrylamide) Microgel Dispersions.* Langmuir, 2000. **16**(13): p. 5546-5552.
9. F. Hofmeister, Arch. Exp. Path. Pharmakol., 1888. **24**: p. 247.
10. Markus Stieger, et al., *Are Thermoresponsive Microgels Model Systems for Concentrated Colloidal suspensions? A Rheology and Small-Angle Neutron Scattering Study.* Langmuir, 2004. **20**: p. 7283-7292.
11. W.B. Russel, D.A.Saville, and W.R. Schowalter, *Colloidal dispersions*. 1989: Cambridge University Press.
12. S. Manley, et al., *Glasslike Arrest in Spinodal Decomposition as a Route to Colloidal Gelation.* Physical Review Letters, 2005. **95**: p. 238302.
13. D. A. Weitz and D. J. Pine, *Dynamic Light Scattering*, in *Dynamic Light Scattering*, W. Brown, Editor. 1993, Clarendon Press: Oxford.

14. P. D. Kaplan, et al., *Geometric Constraints for the Design of Diffusing-wave Spectroscopy Experiments.* Applied Optics, 1993. **32**(21): p. 3828-3836.

15. L. Cipelletti, et al., *Time-resolved Correlation: a new tool for studying temporally heterogeneous dynamics.* Journal of Physics: Condensed Matter, 2003. **15**(1): p. S257-S262.

16. C. W. J. Beenakker and P. Mazur, *Diffusion of Spheres in a Concentrated Suspension II.* Physica A, 1984. **126A**(3): p. 349-370.

17. L. Cipeletti, et al., *Universal Aging Features in the Restructuring of Fractal Colloidal Gels.* Physical Review Letters, 2000. **84**(10): p. 2275-2278.

Acknowledgments.

I would like to acknowledge Dr. Veronique Trappe for introducing me into the field of colloidal physics and supervising my work in Fribourg with particular enthusiasm, priceless knowledge and patience.

I am grateful to Prof. Dr. Peter Schurtenberger who has given me the opportunity to work in his laboratory at the University of Fribourg.

I thank Prof. Dr. Eckhard Bartsch and Prof. Dr. Peter Schurtenberger for agreeing to be co-examiners, and Prof. Dr. Jean-Claude Dousse for being chairman at my PhD defense.

Many thanks to all current and former members of the Soft Condensed Matter Group for inestimable advises, discussions, support and friendship inside and outside the laboratory.

I thank my wife Elena for her patience and support throughout all the period of time that this work took. I also would like to acknowledge my family in Girona and my family in law in Sofia for their constant support.

Curriculum Vitae.

Joaquim Clara Rahola

Date and place of birth:	3rd August 1976, Girona.
Nationality:	Spanish
Contact:	+41 - (0)764188490 (Switzerland) +34 – 972214069 (Spain) joaquim.clara@gmail.com
University degree:	Licenciatura en Física (Spanish M.Sc. in Physics) University of Barcelona, Catalunya, Spain February 2002.

PROFESSIONAL EXPERIENCE.

15th July 2002 – March 2007

PhD Thesis in the Soft Condensed Matter Group of Prof. Dr. Peter Schurtenberger, University of Fribourg, Switzerland. Advisor: Dr. Veronique Trappe. PhD title: "Elasticity and Dynamics of Weakly Aggregated Colloidal Systems".

01/09/2001- 14/07/2002

Research fellow at the University of Barcelona, Physics Faculty, Applied Physics and Optics Department, Prof. Dr. Enric Bertran's FEMAN group. Light Scattering detection and characterization of nanostructured dust growth in Ar-SiH$_4$ low-pressure plasma discharges.

01/02/2001-30/08/2001

Six months stay at the Bulgarian Academy of Sciences, Sofia, Institute of Solid State Physics G. Nadjakov, Prof. Dr. Dimo I. Uzunov Cooperative Phenomena Laboratory. Theoretical studies on Superconductor Phase Transitions in Type I superconductors and on the effect of magnetic fluctuations in the order of the transition for quasi-2D, 3D and intermediate geometries.

01/06/2000-31/09/2000

Stay at the University of Orleans, France, GREMI laboratories, focused on plasma characterization, diagnosis and light scattering detection of nanosized particles. Scientific advisor: Dr. Elhadi Boufendi.

TEACHING ACTIVITIES.

2002-2006.

“Diplome Assistant” at the University of Fribourg, Switzerland. Exercise sessions of: Modern Physics (2004-2006), Atomic Physics (2004-2006), Condensed Matter Physics (2003) and Assistant to experimental student sessions in Thermodynamics (winter semester 2002).

05/2002 – 07/02.

University of Barcelona, Applied Physics and Optics Department, coaching to trainees and incoming Socrates-Erasmus students.

1997 – 2000.

First year university subjects, several private schools, Barcelona. Taught subjects were: Electromagnetism, Mathematics, Informatics, Biophysics, Thermodynamics and General Physics.

PUBLICATIONS.

Non-evolutionary slow dynamics in weakly aggregated particles. J. Clara-Rahola and V. Trappe, under preparation.

Elasticity of particle gels formed by PNiPAM microgels. J. Clara-Rahola and V. Trappe, under preparation.

Particle - Particle Interaction of Block Copolymer Steric Stabilized Spherical Colloids. J. C. Rahola, unpublished.

First Order Phase Transitions Induced by Magnetic Fluctuations and Dimensional Crossover in Type I Superconductor Films. J. C. Rahola Phys. Stud. Vol 5 N° ¾, 2001, 304-309.

Dusty particle detection and plasma characterization in Ar-SiH4 discharges. J.C. Rahola, University of Barcelona, internal report.

CONFERENCES.

− 18-24/09/2005. Participation at the "*19th Conference of the European Colloid and Interface Science*". Geilo, Norway.

− 05-12/06/2004. "*7th European Summer School on Scattering Methods Applied to Soft Condensed Matter*". Bombannes, France. Oral presentation, title: "Scaling in the dynamics of weakly aggregated colloids ", (Bitter Lemon award).

− 16-19/07/2003. "*European Student Colloid Meeting*". University of Bristol, UK. Oral presentation, title: "Scaling of the Elasticity and Dynamics of Weakly Aggregating Colloids".

− 10-13/04/2002. Seminar at the Technical University of Eindhoven, Holland. Title: "Dusty Particle Detection in rf Ar-SiH_4 Plasmas by Laser Light Scattering".

− 01-15/08/2001. "*2nd International Pamporovo Workshop: Quantum Phase and Phase Transitions*". Pamporovo, Bulgaria. Oral presentation, title: "Induced First Order Phase Transitions in Type I superconductors".

INFORMATICS.

Soft Condensed Matter Group, Linux server administrator, University of Fribourg, 2002-2005.

User knowledge of Fortran, Turbo Pascal, Turbo C, C++, Visual Basic, Visual C and Java.

Unix University of Barcelona extension courses: Basic Administration and Advanced Administration.

User knowledge of Origin, Sigma Plot, Mathcad, Mathematica, Windows, Office and Latex2e.

OTHER.

Academic years 1999/2001: University of Barcelona - Llicenciatura en Administració i Direcció d'Empreses (A.D.E. – Degree in Business Managment and Administration). In parallel to the studies in Physics, first two years of the degree completed.